

3-29-2016

# Optimization and Characterization of Integrated Microfluidic Surface Acoustic Wave Sensors and Transducers

Tao Wang

Follow this and additional works at: <http://scholarcommons.usf.edu/etd>

 Part of the [Mechanical Engineering Commons](#)

## Scholar Commons Citation

Wang, Tao, "Optimization and Characterization of Integrated Microfluidic Surface Acoustic Wave Sensors and Transducers" (2016).  
*Graduate Theses and Dissertations*.  
<http://scholarcommons.usf.edu/etd/6153>

This Dissertation is brought to you for free and open access by the Graduate School at Scholar Commons. It has been accepted for inclusion in Graduate Theses and Dissertations by an authorized administrator of Scholar Commons. For more information, please contact [scholarcommons@usf.edu](mailto:scholarcommons@usf.edu).

Optimization and Characterization of Integrated Microfluidic Surface Acoustic Wave  
Sensors and Transducers

by

Tao Wang

A dissertation submitted in partial fulfillment  
of the requirements for the degree of  
Doctor of Philosophy  
Department of Mechanical Engineering  
College of Engineering  
University of South Florida

Major Professor: Rasim Guldiken, Ph.D.  
Nathan Crane, Ph.D.  
Nathan Gallant, Ph.D.  
Garrett Matthews, Ph.D.  
Jing Wang, Ph.D.

Date of Approval:  
March 15, 2016

Keywords: SH-SAWs, SAWs, Pumping, Biosensor, Cancer Detection

Copyright © 2016, Tao Wang

## **DEDICATION**

To my family.

## ACKNOWLEDGEMENT

I would like to acknowledge all the people that have helped me during my Ph.D. studies.

First and foremost, I would like to express my deepest gratitude towards my supervisor, Dr. Rasim Guldiken, for guiding me through the years of study and research. The dissertation would have been impossible without the help of Dr. Guldiken, who has played a key role in stimulating my interests and helping me improve my theoretical skills. Thank you for all the valuable opportunities that you have given me. Your excellent guidance and trust motivated me through all the stages of my Ph.D. study. Dr. Guldiken has made my research experience truly enjoyable.

Secondly, I am greatly indebted to Dr. Nathan Crane, Dr. Nathan Gallant, Dr. Garrett Matthews and Dr. Jing Wang for serving as my committee members. Thanks for all your support. Your motivation inspires me to further study in this interesting and challenging topic. The invaluable advices and generous guidance that you have given me help me successfully move my dissertation forward. Without your help, I certainly cannot be here right now.

I should give my hearty gratitude to all the other faculty members of the Department of Mechanical Engineering. I cannot forget during the study of my M.S. degree and Ph.D. degree, your considerations and patient instructions cultivate my initiative and creativity. Moreover, I would like to give my deep gratitude to Dr. Subhra Mohapatra and Dr. Shyam Mohapatra from the Department of Molecular Medicine. I have been inspired because of your sharp and dynamic mind.

At the same time, I would like to thank all my lab mates: Myeong Chan Jo, Onursal Onen, Emre Tufekcioglu, Scott Padilla, Joel Cooper, Greeshma Manohar and Senmiao Hu for your friendship and helpful advices. I learnt a lot from you. The pleasant discussions we had were a great source of inspiration. Many thanks to Rajesh Ramakrishnan Nair, Ryan Green and Mark Howell from the Department of Molecular Medicine for their countless ideas and medical experimental skills. Your generous assistance made the experiments more precise and reliable.

Besides, I would like to extend my heartfelt appreciation to my friends with whom I had many meaningful communications and shared many precious moments: Qi Ni, Jose M Carballo, Ruiz Yaricet, Judith Chiang, Eric Tridas, Yaozhu Huang, Qi Yan, Henry Wang, Jason Wu, Ryan, Chaoyan Wang, Abhishek Dey, and Ivan Rivera. You put considerable time and effort into helping me with my study. I benefited a lot from your suggestions. Thank you for your invaluable advice and kindness.

Last but not least, I am very grateful for my beloved parents, Chengwei Wang and Chunfang Chen. I really admire your hard-working spirit. It makes me realize the importance of persistence. Thank you for contributing a lot to my study. Your constant support and love warm me and keep me moving on. I would specially like to thank my wife, Yiwen Tang, for your love, your whole-hearted support and for always being there for me. I had so many memorable days with you during these years. Your unconditional trust and support gives me faith to overcome challenges and makes me a better person.

## TABLE OF CONTENTS

LIST OF TABLES .....	iii
LIST OF FIGURES .....	iv
ABSTRACT .....	ix
CHAPTER 1. INTRODUCTION .....	1
1.1. Motivation .....	3
1.2. Dissertation Organization .....	4
CHAPTER 2. SURFACE ACOUSTIC WAVES .....	6
2.1. Piezoelectricity .....	8
2.2. Stress and Strain in a Nonpiezoelectric Elastic Solid .....	10
2.3. Stress and Strain in a Piezoelectric Elastic Solid .....	11
CHAPTER 3. FINITE ELEMENT MODELING AND DEVICE DESIGN .....	13
3.1. Theoretical Background .....	13
3.2. Interdigital Surface Acoustic Wave Transducer Design with 2D Simulations .....	14
3.2.1. Eigenfrequency Analysis .....	15
3.2.2. Parameter Analysis .....	15
3.2.3. Effect of Substrate and Finger Design .....	16
3.3. Interdigital Surface Acoustic Wave Transducer Design with 3D Simulations .....	18
3.3.1. Effect of Substrate and Finger Thickness Ratio .....	19
3.3.2. Effect of Guide Layers in 3D Cells .....	31
3.3.3. Frequency Sweep Analysis in 3D Model .....	32
CHAPTER 4. SURFACE ACOUSTIC WAVE BASED MICROFLUIDIC PUMP .....	34
4.1. Note to Reader .....	34
4.2. Introduction .....	34
4.3. Device Operation, Simulation and Design .....	35
4.4. Transducer Fabrication and Microchannel Integration .....	40
4.5. Experimental Setup .....	43
4.6. Results and Discussion .....	45
4.7. Conclusions .....	52
CHAPTER 5. LIQUID PROPERTY SENSING WITH A SURFACE ACOUSTIC WAVE BASED SENSOR .....	53
5.1. Introduction .....	53

5.2. Working Principle .....	54
5.3. Device Design and Fabrication .....	55
5.4. Experimental Setup .....	59
5.5. Results and Discussion .....	61
5.5.1. Experiment for Flow Rate Measurement .....	61
5.5.2. Finite Element Simulations .....	62
5.5.3. SH-SAW Measurements of Liquid Mechanical Properties .....	65
5.6. Conclusions .....	69
<b>CHAPTER 6. CELL QUANTIFICATION WITH A SURFACE ACOUSTIC WAVE</b>	
<b>MICROFLUIDIC SENSOR .....</b>	<b>70</b>
6.1. Note to Reader .....	70
6.2. Introduction .....	70
6.3. Working Principle .....	72
6.4. Design and Fabrication of Bio-Sensor .....	73
6.4.1. Device Design .....	73
6.4.2. Device Fabrication .....	75
6.5. Experimental Setup .....	77
6.5.1. Experimental Protocol for SAW Measurement .....	77
6.5.2. Experimental Protocol for Measuring Cell Viability .....	77
6.5.3. Experimental Protocol for Measuring Cell Proliferation .....	78
6.5.4. Experimental Protocol for Culturing 3D Tumoroids .....	78
6.6. Results and Discussion .....	78
6.6.1. Cell Viability and Cell Proliferation Is Not Affected after SAW	
Measurements .....	78
6.6.2. Frequency Shift Increases with Increasing Cell Concentration and	
Sensitivity Is Further Aided by the Use of ZnO .....	80
6.6.3. SAW Measurements of Cell Density Match Simulation Results .....	81
6.6.4. SAW Measurements Aid in Monitoring Growth of A549 3D Spheroid	
Cultures .....	83
6.7. Conclusions .....	84
<b>CHAPTER 7. CONCLUSIONS AND FUTURE WORK .....</b>	<b>86</b>
7.1. Summary and Contributions .....	86
7.2. Future Work .....	88
<b>REFERENCES .....</b>	<b>89</b>
<b>APPENDICES .....</b>	<b>99</b>
Appendix A. Copyright Clearance (Chapter 4) .....	100
Appendix B. Copyright Clearance (Chapter 6) .....	101

## LIST OF TABLES

Table 4.1. Device parameters used for the design and fabrication of the IDT transducers .....	40
Table 5.1. Parameter of delay line and resonator design .....	56
Table 5.2. Density and viscosity of the different weight concentrations of glycerol .....	65
Table 6.1. Device parameters used for the simulation and fabrication of the IDT transducers .....	74



## LIST OF FIGURES

Figure 2.1. Rayleigh surface acoustic wave on a lithium niobate surface .....	7
Figure 2.2. Shear horizontal surface acoustic wave on a lithium niobate surface .....	7
Figure 2.3. Schematic of piezoelectric effect.....	8
Figure 3.1. (a) 2D cell model design of the interdigital transducer in COMSOL; (b) interdigital transducer design parameters employed in this dissertation .....	14
Figure 3.2. Effect of substrate thickness on the center frequency of IDTs on 128 °YX cut lithium niobate substrate in 2D simulation model .....	17
Figure 3.3. Effect of finger thickness on the center frequency of IDTs on 128 °YX cut lithium niobate substrate in 2D simulation model .....	17
Figure 3.4. Effect of metallization ratio on the center frequency of IDTs on 128 °YX cut lithium niobate substrate in 2D simulation model .....	18
Figure 3.5. 3D cell model design of the interdigital transducer in COMSOL.....	19
Figure 3.6. Effect of finger thickness on the center frequency of IDTs on 128 °YX cut lithium niobate substrate .....	20
Figure 3.7. Effect of finger thickness on the center frequency of IDTs on 36 °YX cut lithium tantalate substrate .....	20
Figure 3.8. Effect of finger thickness on the center frequency of IDTs on ST-cut quartz substrate .....	21
Figure 3.9. Effect of substrate thickness ratio on the center frequency of IDTs on different substrates .....	21
Figure 3.10. Effect of metallization ratio on the center frequency of IDTs on 128 °YX cut lithium niobate substrate .....	22
Figure 3.11. Effect of metallization ratio on the center frequency of IDTs on 36 °YX cut lithium tantalate substrate .....	24

Figure 3.12. Effect of metallization ratio on the center frequency of IDTs on ST-cut quartz substrate .....	24
Figure 3.13. Effect of finger thickness on the center maximum displacement of IDTs on 128 °YX cut lithium niobate substrate .....	25
Figure 3.14. Effect of finger thickness on the center maximum displacement of IDTs on 36 °YX cut lithium tantalate substrate .....	26
Figure 3.15. Effect of finger thickness on the center maximum displacement of IDTs on ST-cut quartz substrate .....	26
Figure 3.16. Effect of substrate thickness on the center maximum displacement of IDTs on 128 °YX cut lithium niobate substrate .....	27
Figure 3.17. Effect of substrate thickness on the center maximum displacement of IDTs on 36 °YX cut lithium tantalate substrate .....	28
Figure 3.18. Effect of substrate thickness on the center maximum displacement of IDTs on ST-cut quartz substrate .....	28
Figure 3.19. Effect of metallization ratio on the center maximum displacement of IDTs on 128 °YX cut lithium niobate substrate .....	29
Figure 3.20. Effect of metallization ratio on the center maximum displacement of IDTs on 36 °YX cut lithium tantalate substrate .....	30
Figure 3.21. Effect of metallization ratio on the center maximum displacement of IDTs on ST-cut quartz substrate .....	30
Figure 3.22. Effect of different guide layer thicknesses on the center frequency of IDTs on 36 °YX cut lithium tantalate substrate.....	31
Figure 3.23. Effect of different guide layer thicknesses on the center frequency of IDTs on ST-cut quartz substrate.....	32
Figure 3.24. Realistic model to simulate the responses of receiver IDTs.....	33
Figure 3.25. Frequency spectrum simulation results of 128 °YX cut lithium niobate substrate by using frequency sweep analysis methods .....	33
Figure 4.1. Conceptual view of the liquid pumping and manipulation induced by surface acoustic waves .....	37

Figure 4.2. (a) SAW transducer geometry employed in the simulations; (b) profile of the IDT fingers formed by 100 nm chromium deposited on a 500 $\mu\text{m}$ 127.8° lithium niobate substrate .....	38
Figure 4.3. (a) Simulated operation frequency as a function of IDT finger height and material selection; (b) simulated operation frequency as a function of substrate thickness .....	39
Figure 4.4. Fabrication process flow for SAW transducers, PDMS molding, Cytop layer spinning and bonding .....	41
Figure 4.5. (a) Aligned IDTs and microchannel on the substrate; (b) close-up of the microchannel design investigated in this study; (c) details of the chrome IDTs .....	42
Figure 4.6. Experimental setup: An external pump was connected to the channel inlet to pump the liquid into the channel.....	43
Figure 4.7. (A) Receding contact angle of the drop on the PDMS surface without Cytop layer; (B) advancing contact angle of the drop on the PDMS surface without Cytop layer; (C) receding contact angle of the drop on the PDMS surface with Cytop layer; (D) advancing contact angle of the drop on the PDMS surface with Cytop layer; (E) static contact angle of the drop on the lithium niobate substrate surface without Cytop layer; (F) static contact angle of the drop on the substrate with Cytop layer .....	45
Figure 4.8. An illustration of different volumes of liquid pumping in the channel with sealed inlet and open outlet.....	46
Figure 4.9. The pumping experiment in the 250 $\mu\text{m}$ channel without Cytop over 75 seconds.....	47
Figure 4.10. Experimental pumping velocity as a function of applied input power with two different liquid volumes (0.22 $\mu\text{l}$ and 0.11 $\mu\text{l}$ ) in a 500 $\mu\text{m}$ microchannel with the Cytop layer coating in the design.....	48
Figure 4.11. Experimental pumping velocity as a function of applied input power in a 500 $\mu\text{m}$ microchannel with/without the Cytop layer in the design for two different liquid volumes: 0.22 $\mu\text{l}$ (Figure 4.11a) and 0.11 $\mu\text{l}$ (Figure 4.11b) .....	50
Figure 4.12. Experimental pumping velocity as a function of applied input power in a 250 $\mu\text{m}$ microchannel with/without the Cytop layer in the design for two different liquid volumes: 0.11 $\mu\text{l}$ (Figure 4.12a) and 0.054 $\mu\text{l}$ (Figure 4.12b) .....	51
Figure 5.1. Delay line and two-port resonator design with channel alignment mark.....	55

Figure 5.2. Frequency spectrum for resonator design and delay line design by network analyzer .....	57
Figure 5.3. Aligned resonator and microchannel on the substrate.....	58
Figure 5.4. Conceptual view of the oscillatory circuit system for liquid properties detection .....	59
Figure 5.5. Long-term experiment to test stability .....	60
Figure 5.6. Results of calculation of the flow rate from the equation compared to the experimental results .....	62
Figure 5.7. 3D-cell simulation of resonance frequency .....	63
Figure 5.8. 3D simulation of insertion loss effected by the mechanical properties of the different weight concentrations of glycerol .....	64
Figure 5.9. Relative frequency shift of different concentration of glycerol .....	66
Figure 5.10. Different weight concentrations of glycerol with relation to multiplication of density and viscosity .....	67
Figure 5.11. Simulation results of designed resonator's response on different weight concentrations of glycerol.....	67
Figure 5.12. Relative frequency response to different weight concentrations of particles (8 $\mu\text{m}$ in diameter and 1.09 $\text{g}/\text{cm}^3$ in density).....	68
Figure 6.1. A 3D COMSOL model and simulation results based on the 36 °Y-cut LiTaO <sub>3</sub> : (A) 3D cell model geometry with mesh; (B) resonance frequency of the IDTs with a 200 nm thick ZnO layer; and (C) resonance frequency of the IDTs with 12.5 K cells media on the 200 nm thick ZnO layer surface.....	73
Figure 6.2. (A) Conceptual view of the oscillatory circuit system. ....	76
Figure 6.3. Cell viability following SAW measurement .....	79
Figure 6.4. Cell proliferation following SAW measurement.....	80
Figure 6.5. Relative frequency shift response to the different cell concentrations.....	81
Figure 6.6. SAWs experiment data matches the tendency of the simulation results on the ZnO coated sensor.....	83

Figure 6.7. (A) Representative image of A549 cells growing in 3D tumoroid structures on the 3P scaffold using NucBlue nuclear stain on day 8 of culture .....84

## ABSTRACT

Surface acoustic waves (SAWs) have a large number of applications and the majority of them are in the sensor and actuator fields targeted to satisfy market needs. Recently, researchers have focused on optimizing and improving device functions, sensitivity, power consumption, etc. However, SAW actuators and sensors still cannot replace their conventional counterparts in some mechanical and biomedical areas, such as actuators for liquid pumping under microfluidic channels and sensors for real-time cell culture monitoring. The two objectives of this dissertation are to explore the potential of piezoelectric materials and surface acoustic waves for research on actuators and sensors in the mechanical pump and biosensor areas.

Manipulation of liquids in microfluidic channels is important for many mechanical, chemical and biomedical applications. In this dissertation, we first introduced a novel integrated surface acoustic wave based pump for liquid delivery and precise manipulation within a microchannel. The device employed a hydrophobic surface coating (Cytop) in the device design to decrease the friction force and increase the bonding. Contrary to previous surface acoustic wave based pumps which were mostly based on the filling and sucking process, we demonstrated long distance media delivery (up to 8mm) and a high pumping velocity, which increased the device's application space and mass production potential. Additionally, the device design didn't need precise layers of water and glass between substrate and channel, which simplified the design significantly. In this study, we conducted extensive parametric studies to quantify the effects of the liquid volume pumped, microchannel size, and input applied power as well as the existence of

hydrophobic surface coating on the pumping velocity and pump performance. Our results indicated that the pumping velocity for a constant liquid volume with the same applied input power could be increased by over 130% (2.31 mm/min vs 0.99 mm/min) by employing a hydrophobic surface coating (Cytop) in a thinner microchannel (250  $\mu\text{m}$  vs 500  $\mu\text{m}$ ) design. This device could be used in circulation, dosing, metering and drug delivery applications which necessitated small-scale precise liquid control and delivery.

This dissertation also introduced a novel SAW-based sensor designed and employed for detecting changes in cell concentration. Before conducting cell concentration experiments, preliminary experiments were conducted on weight concentration differentiation of microfluidic particles based on a polydimethylsiloxane (PDMS) channel and surface acoustic wave resonator design. The results confirmed that our device exerted an ultra-stable status to detect liquid properties by monitoring continuous fluids. An improved design was carried out by depositing a 200 nm ZnO layer on top of the lithium tantalate substrate surface increased the sensitivity and enabled cell concentration detection in a microfluidic system.

Comprehensive studies on cell viability were carried out to investigate the effect of shear horizontal (SH) SAWs on both a cancerous (A549 lung adenocarcinoma) and a non-cancerous (RAW264.7 macrophage) cell line. Two pairs of resonators consisting of interdigital transducers (IDTs) and reflecting fingers were used to quantify mass loading by the cells in suspension media as well as within a 3-dimensional cell culture model. In order to predict the characteristics and optimize the design of the SH-SAW biosensor, a 3D COMSOL model was built to simulate the mass loading response of the cell suspensions. These results were compared to experimental data generated by pipetting cell concentrations of 3.125K, 6.25K, 12.5K, 25K and 50K cells per 100  $\mu\text{L}$  into the PDMS well and measuring to obtain the relative frequency shift from the two oscillatory

circuit systems (one of which functioned as a control). Frequency shift measurements were also collected from A549 cells cultured on a 3D nanofiber scaffold produced by electrospinning to evaluate the device's ability to detect changes in cell density as the cells proliferated in culture over the course of eight days. The device's ability to detect changes in cell density over time in a 3D model along with its biocompatibility reveal great potential for this device to be incorporated into 3D in vitro cancer research applications.



## CHAPTER 1. INTRODUCTION

After a thorough mathematical discussion on the propagation of surface acoustic waves (SAWs) at the free isotropic elastic solid surface, first reported by Lord Rayleigh<sup>1</sup>, a variety of applications have utilized the mechanical theory of surface acoustic waves. Named by their discoverer, surface waves have a longitudinal and vertical shear component that can couple with media in contact with the substrate surface. This coupling strongly affects the amplitude and velocity of the wave, allowing SAW sensors to directly sense dielectric and mechanical properties<sup>2,3</sup>. This type of wave is commonly used in devices in the electronic circuit industry. SAW devices fabricated with piezoelectric materials can transduce electric energy to mechanical energy. Many SAW devices have been developed based on the properties of SAW energy transfer, such as mixing, separation, pumping and detecting devices. Mixing, separation and pumping devices are based on energy transduction from electric energy to the body force on liquid or particles. The SAW sensor is based on the application of energy loss and phase velocity change fundamentals of piezoelectric materials used to design interdigital transducers (IDTs) for converting acoustic waves to electrical signals and vice versa. These devices are fabricated by the MEMS (microelectromechanical systems) fabrication process, as well as the process used in microfabrication of integrated circuits.

The advantages offered by SAW devices include their smaller size, integration capability with accompanying electronics, biocompatibility, low power consumption and non-contact with the sample media. Recently, SAW devices designed as actuators and sensors have been integrated

with microfluidic systems to provide significant advantages<sup>4-6</sup>, such as sealed environments for bio-samples and sub-microliter volume consumption. In the actuator field, the majority of research has focused on high-efficiency devices for mixing<sup>7,8</sup>, separation<sup>9,10</sup> and drug delivery<sup>11,12</sup> purposes. However, pumps are another key component in microfluidic systems that can be integrated into many devices to accomplish an important task. It is commonly known by practitioners of the art that, friction forces dominate pumping forces in the micro-scale range of the microchannel, which makes liquid appear more viscous than it is<sup>13</sup>. A mechanical pump in the sub-micrometer range increases the manufacturing cost to an unreasonable price. As compared to alternatives, liquid manipulation and pumping with SAW is a non-contact technique capable of precise and highly repeatable flow manipulation.

In the sensor field, SAW application has been broadly exerted and experimented as physical sensors<sup>14</sup>, biology sensors<sup>15,16</sup> and chemical sensors<sup>17,18</sup>. Biosensors are widely used in cancer detection<sup>15,16</sup> and bio-agent detection<sup>19,20</sup>. Chemical sensors<sup>21,22</sup> can be found in reaction, evaporation and chemical complex areas. SAWs in biosensors and chemical sensors are mostly based on the devices with guided layers in the design, which is deposited or spin coated on the surface of the device. These sensors can absorb or react to the targeted bio-sample or chemical vapors. The mass loading of the chemical and bio-sample establish an equilibrium of the mechanical and dielectric properties between adsorption and desorption, which changes the area/mass density, viscoelastic and permittivity properties of the guide film<sup>23-25</sup>. The mechanical and dielectric property of guide layer changes will result in wave transmission energy loss, which changes the propagation velocity and phase of the acoustic wave. As a result, the resonant frequency of the SAW sensor shifts to lower frequencies. Since the acoustic wave responds to a

change of mechanical and dielectric properties on the path that the wave travels, the guide layer has a key role in determining many chemical and biological applications' sensitivity and stability.

The majority of liquid sensors use grating or films instead of microfluidic channel placed on the sensing area<sup>26,27</sup>. Without an integrated fluidic system, the liquid being tested comes into direct contact with open atmosphere. Therefore, an integrated microfluidics system is introduced to SAW based sensor to monitor the properties of the media in real time with advantages of low liquid sample consumption, fast analysis, and protection of the media<sup>24,28</sup>. The second objective of this dissertation is focused on the liquid sensor based on a two-port resonator design integrated into a microfluidic system. Then based on the advantages of two-port resonators and microfluidic systems, a guide layer SH-SAW sensor was designed and optimized by the commercially available finite element modeling software, COMSOL, to simulate the properties of the liquid and mass loading of the cells.

## **1.1. Motivation**

Recently, a variety of SAW sensors and transducers have been demonstrated accomplishing many critical tasks for various applications. Demand for microfluidic actuators and microfluidic biosensors continues to rise each year. Currently, most biosensors focus on antibody detection, sample quantification and disease diagnostics. However the majority of these devices require long operation time and analysis. Additionally, the requirements of real time monitoring of live cell viability in a culture environment are as important as obtaining the physical parameters and identifying/detecting the biomarker.

In 2014 the global biosensors market peaked at \$12.96 billion (USD) with a projected growth rate of 9.7% per year during 2015 to 2020<sup>29</sup>. However SAW biosensor still need to overcome many technical challenges such as stability, sensitivity, reliability, cost and portability

over competing sensor technologies. This dissertation intends to address some of the shortcomings of the current state of the art and introduces a novel SAW micropump and a biosensor.

## **1.2. Dissertation Organization**

This dissertation is organized as follows.

Chapter 2 presents a historical overview of piezoelectric crystal material. A mathematical development on the piezoelectric phenomena is discussed in detail. Both the stress and strain relationship in piezoelectric materials is demonstrated in this chapter.

Chapter 3 provides the finite element modeling employed in the design of SAW. We demonstrated how various design parameters does affect the phase velocity and sensitivity of the SAWs devices.

Chapter 4 presents a novel SAW actuator for pumping purpose. Details of design, fabrication, optimizations and experimental results are provided in this chapter. A Cytop layer is introduced to as a way to reduce the adhesive force of PDMS and bonding channel and substrate are presented in this chapter.

Chapter 5 provides optimizations of SAW devices by introducing resonator design on a SH-SAW sensor. The resonator design was fabricated to detect the flow rate, flow viscosity and concentration of particles inside the microfluidic channel. Three-dimensional modeling on prediction of the flow viscosity is also presented in this chapter.

In Chapter 6, a study is carried out on a resonator design SH-SAW sensor for real time monitoring of non-cancerous and cancerous cell lines. COMSOL modeling was demonstrated to predict the frequency shift caused by different cell mass loadings (3.125K, 6.25K 12.5K, 25K and 50K). Different number of A549 cells cultured on a 3-D nanofiber scaffold were detected by the

device. A study on cell viability revealed the effect of shear horizontal surface acoustic waves on A549 and RAW 264.7 cell lines.

Chapter 7 summarizes the work of this dissertation and provides methods and suggestions on how to develop and improve future SAW actuators and sensors design in the future.

## CHAPTER 2. SURFACE ACOUSTIC WAVES

This chapter introduces the theoretical and mathematical background for piezoelectric materials and surface acoustic wave applications. It will give a thorough demonstration of the elementary stress-strain tensor relations.

In a piezoelectric substrate, two major waves will be generated: either surface acoustic waves or bulk acoustic waves propagating through the interior of the substrate. Surface acoustic waves are energy-concentrated waves located on the free surface of a piezoelectric material. In this dissertation, the generation of acoustic waves is achieved by application of a voltage signal to a metal film interdigital transducer (IDT) patterned on the surface of a piezoelectric substrate. Several types of SAWs are generated by different materials, cut types and boundary conditions<sup>30</sup>. The two types of SAWs discussed in this dissertation are Rayleigh waves and shear horizontal waves, which are the most common types of SAWs.

The Rayleigh wave propagating at the surface of a semi-infinite isotropic medium is actually a two-dimensional wave with a combination of longitudinal and transverse waves in the piezoelectric substrate. Figure 2.1 shows Rayleigh waves simulated by commercially available COMSOL 4.4 Multiphysics software (COMSOL, Inc., Palo Alto, CA). The particles of the substrate travel in an elliptical motion in a plane normal to the substrate surface and parallel to the propagation direction. The body force and acoustic force as a result of the Rayleigh waves allows to manipulation of liquid as well as the particles inside the liquid. Rayleigh surface waves are more widely used for mixing, separating and pumping devices with microfluidic system.

Shear horizontal (SH) waves usually have particle displacement only normal to the direction of the wave propagation at the surface, as shown in Figure 2.2. They have low radiation loss in liquid as compared to Rayleigh waves, which makes SH-SAWs the most frequently used SAW type for biosensors. Less wave attenuation and damping by liquid loading are also reasons for SH-SAW use as a liquid loaded application. For Rayleigh waves, large radiation losses will travel into the liquid on the surface of the substrate, which also generate longitudinal waves inside the liquid.

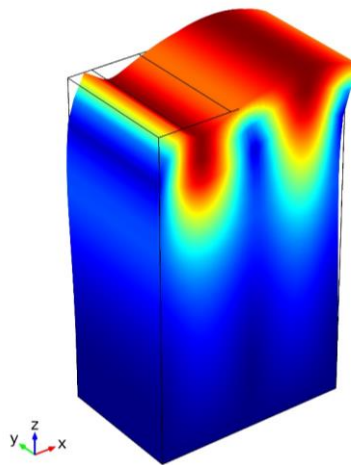


**Figure 2.1.** Rayleigh surface acoustic wave on a lithium niobate surface

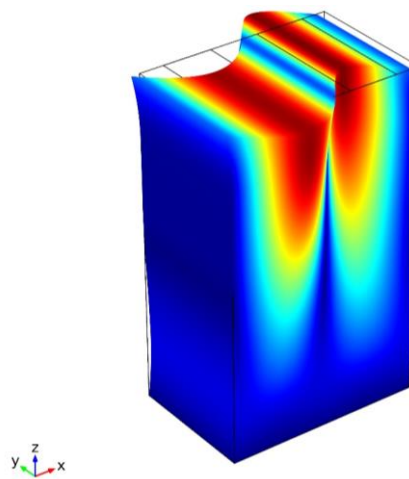


**Figure 2.2.** Shear horizontal surface acoustic wave on a lithium niobate surface

The other SAWs most frequently used in acoustic sensor system are Love waves, which are generated by the SH-SAW substrate deposited by a thin layer of material with low acoustic wave velocity. The added layer acts as a waveguide and keeps most of the wave's energy localized to the surface. The most popular waveguides on piezoelectric materials are SiO<sub>2</sub>, ZnO, TiO<sub>2</sub> and PMMA<sup>31</sup>. Different guide layers with varying acoustic wave velocities and dielectric properties do impact the sensitivity and stability of the sensor system.

### 2.1. Piezoelectricity

Brothers Pierre and Jacques Curie first demonstrated the novel phenomenon of some crystal surfaces having positive and negative charges when the crystal was poled in different directions<sup>32,33</sup>. In 1880 they published their experiment studies, which consisted of a conclusive measurement of surface charges appearing on specially prepared crystals (tourmaline, quartz, topaz, cane sugar, Rochelle salt, etc.) that were subjected to mechanical stress<sup>34</sup>. After Hankel proposed the name of this phenomenon (the piezoelectric effect)<sup>35</sup>, more and more researchers explored piezoelectric materials.

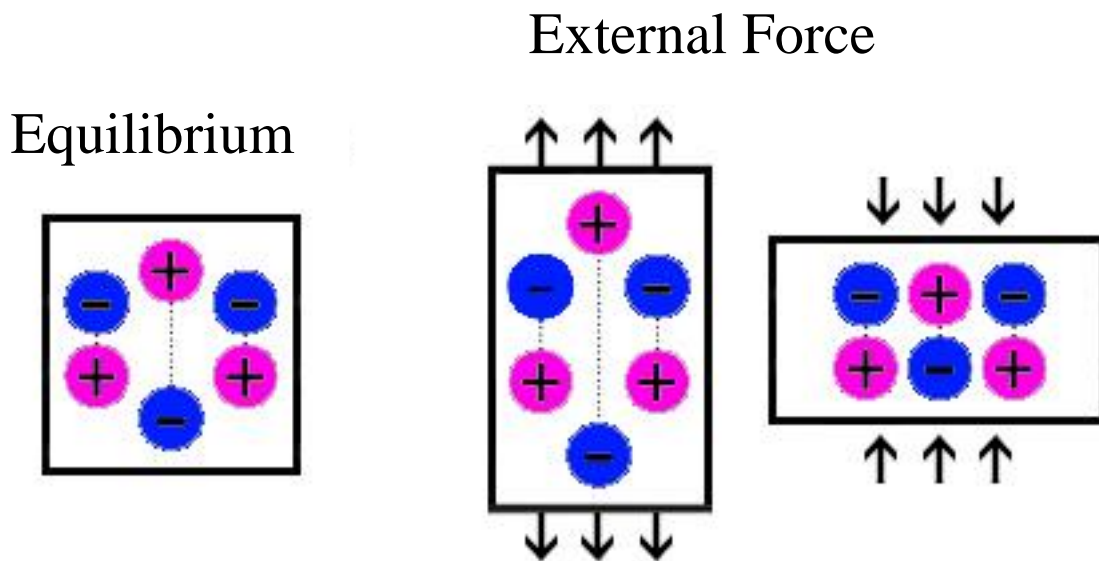


**Figure 2.3.** Schematic of piezoelectric effect



When no external stress appears on the surface of piezoelectric material, negative charges and positive charges are reciprocally canceled in the 3D structure of the piezoelectric material as a result of negative and positive molecules colliding. As illustrated in Figure 2.3, when pressure is exerted on the surface of the piezoelectric material, the internal structure deforms, which causes separation of the positive and negative centers of the molecules. Hence, the material is polarized and generates an electric field on the surface. The piezo material simply transforms a mechanical signal to an electric field.

After SAW properties were first discovered by Lord Rayleigh, the first SAW devices were investigated, opening the door for an explosion in the development of SAW devices<sup>36</sup>. These devices consist of many pairs of electrode fingers deposited on the surface of a piezoelectric material by plasma-enhanced chemical vapor deposition (PECVD) or by sputtering. When external stress is exerted on the surface of the material, the charge density of the molecule generate the electric field and results in a flow of free charges in the electric circuit that connects with the two metal plates. The flow of the free charge switches the direction depending on the pressure signal. When the applied pressure is removed, the flow caused by the polarization vanishes and charges return to the initial condition. When the current flow is connected to radio frequency (RF) or network analysis, an electrical signal can be detected.

The experiments performed by the Curie brothers demonstrated that the surface density of the generated charge was proportional to the pressure exerted. This relationship can be formulated in a simple way as follows.

$$P = dT \quad \text{Equation 2.1}$$

where  $P$  is the piezoelectric polarization vector, the magnitude of which is equal to the linked

charge surface density by piezoelectric effect at the surface,  $d$  is the piezoelectric strain coefficient and  $T$  is the stress to which the piezoelectric material is subjected.

The first step to understand the surface acoustic waves starts with the fact that propagation of an SAW consists of two displacement components, one being parallel to the SAW propagation direction, and the second being normal to the SAW propagation direction. These two wave motions are 90 °out of phase with one another in the time domain. Rayleigh waves travel in the direction of wave propagation and shear horizontal waves are the wave with displacement normal to the surface. The amplitude of these displacement components become negligible for penetration depths greater than a few acoustic wavelengths into the body of the piezoelectric solid<sup>37</sup>.

## 2.2. Stress and Strain in a Nonpiezoelectric Elastic Solid

The relationship between the mechanical stress  $T$  and strain  $S$  of nonpiezoelectric elastic solid can be related proportionally by Hooke's Law. For simple compressional stress and strain along the same axis, this can be written as

$$\{T\} = \{c\}:\{S\} \quad \text{Equation 2.2}$$

where  $\{c\}$  is the Young's modulus (N/m<sup>2</sup>), also known as elastic stiffness coefficient. Expanding tensor Equation 2.2 for value of  $T_{xx}$  along the x axis can be written as<sup>38</sup>

$$T_{xx} = c_{ij} + S_{ij}, i, j = x, y, z \quad \text{Equation 2.3}$$

and then expanding in 3-dimension gives<sup>38</sup>

$$\begin{aligned} T_{xx} = & c_{xxx}S_{xx} + c_{xxxy}S_{xy} + c_{xxxz}S_{xz} + c_{xxyx}S_{yy} + c_{xxyz}S_{yz} \\ & + c_{xxzx}S_{zx} + c_{xxzy}S_{zy} + c_{xxzz}S_{zz} \end{aligned} \quad \text{Equation 2.4}$$

In Equation 2.4,  $T$  and  $S$  are second rank tensors indicated by two suffixes, but  $c$  is indicated with four suffixes. After the reduction, using a matrix equation,  $[c]$  becomes a 6×6 matrix:

$$[T] = [c][S] \quad \text{Equation 2.5}$$

### 2.3. Stress and Strain in a Piezoelectric Elastic Solid

The stress-strain relationship deduced in Equation 2.5 is only applicable to nonpiezoelectric materials. Mechanical stress-strain does not change when an electrical field was applied on these type solids. Considering the piezoelectric effects, the electrical relationships should be taken into consideration. When a voltage is applied, the electric field  $E$  causes a change of piezoelectric materials' molecular charge distributions which result in an accumulation of surface charge. The surface charge of density  $D$  (C/m<sup>2</sup>) can be obtained by<sup>39</sup>

$$D = [e][S] + [\varepsilon] \quad \text{Equation 2.6}$$

where  $[e]$  represents the piezoelectric constant matrix,  $E$  is the applied electric field,  $[\varepsilon]$  is the dielectric permittivity and  $[S]$  is the strain matrix. In piezoelectric materials the mechanical stress relationships can be expanded to<sup>37</sup>

$$[T] = [c][S] - [e^t] \quad \text{Equation 2.7}$$

The  $[e^t]$  matrix is the transpose matrix of piezoelectric constant matrix and  $[e^t]$  is a 3 ×6 matrix. Three essential SAW parameters of a piezoelectric material, the phase velocity, the attenuation and electromechanical coupling coefficient are determined for surface waves propagation on the free substrate. Electromechanical coupling coefficient ( $K^2$ ) is a measure of the conversion efficiency for a piezoelectric material in converting an electric signal into mechanical energy<sup>40,41</sup>. It may be shown that the electromechanical coupling coefficient  $K^2$  can be defined in terms of the piezoelectric coefficient, elastic constant and dielectric permittivity as<sup>39</sup>

$$K^2 = \frac{e^2}{c\varepsilon} \quad \text{Equation 2.8}$$

The electromechanical coupling coefficient  $K^2$  may also be obtained experimentally as follows<sup>39</sup>

$$K^2 = -\frac{2\Delta v}{v} \quad \text{Equation 2.9}$$

which can define the magnitude of the SAW velocity change  $\Delta v$  in terms of unperturbed SAW velocity, piezoelectric coefficient, elastic constant and dielectric permittivity as<sup>39</sup>

$$\Delta v = -\frac{ve^2}{2c\epsilon} \quad \text{Equation 2.10}$$

After considerable manipulation, the final version of the equation will be obtained as<sup>42</sup>

$$\frac{\Delta v}{v} = \frac{1}{v} \left[ \frac{\partial v}{\partial m} \Delta m + \frac{\partial v}{\partial c} \Delta c + \frac{\partial v}{\partial T} \Delta T + \frac{\partial v}{\partial \sigma} \Delta \sigma + \frac{\partial v}{\partial p} \Delta p \dots \right] \quad \text{Equation 2.11}$$

In Chapters 5 and 6, Equation 2.11 will be employed for detection based on the shear horizontal sensor.

## CHAPTER 3. FINITE ELEMENT MODELING AND DEVICE DESIGN

### 3.1. Theoretical Background

The first finite element method (FEM) analysis of surface acoustic wave devices was implemented by Endoh<sup>43</sup>. The initial SAW modeling with COMSOL Multiphysics was demonstrated by Nemade et al. (2006)<sup>44</sup>. In this dissertation we modeled SAW devices on 128° YX cut lithium niobate substrate, 36° YX cut lithium tantalite substrate and ST-Quartz by employing commercially available software COMSOL using finite element analysis (FEA). Even though the method employed cannot provide information on filter input-output impedance levels, circuit factor loading, harmonic operation, wave interference and diffraction, it can still provide excellent preliminary design information on the response of a SAW sensor<sup>45</sup>. The frequency analysis of a SAW device is illustrated with the periodic boundary conditions in 2D and 3D cell model simulations. A fundamental simulation was conducted on the effects of parameters such as finger width, finger thickness, and substrate thickness on the phase velocity and frequency response in 2D and 3D models. After this step, we used eigenfrequency, frequency sweep and parametric sweep analysis to simulate different thicknesses of ZnO/TiO<sub>2</sub>/SiO<sub>2</sub> layer on lithium tantalate, lithium niobate and quartz devices. Frequency response on different cell concentrations was also simulated in a 3D model. Fluids with particles of different concentrations and viscosities resulting in frequency shifts in SAW devices were also investigated in COMSOL simulations. FEM methods can easily predict the experiment results and optimize the design in an affordable way.

### 3.2. Interdigital Surface Acoustic Wave Transducer Design with 2D Simulations

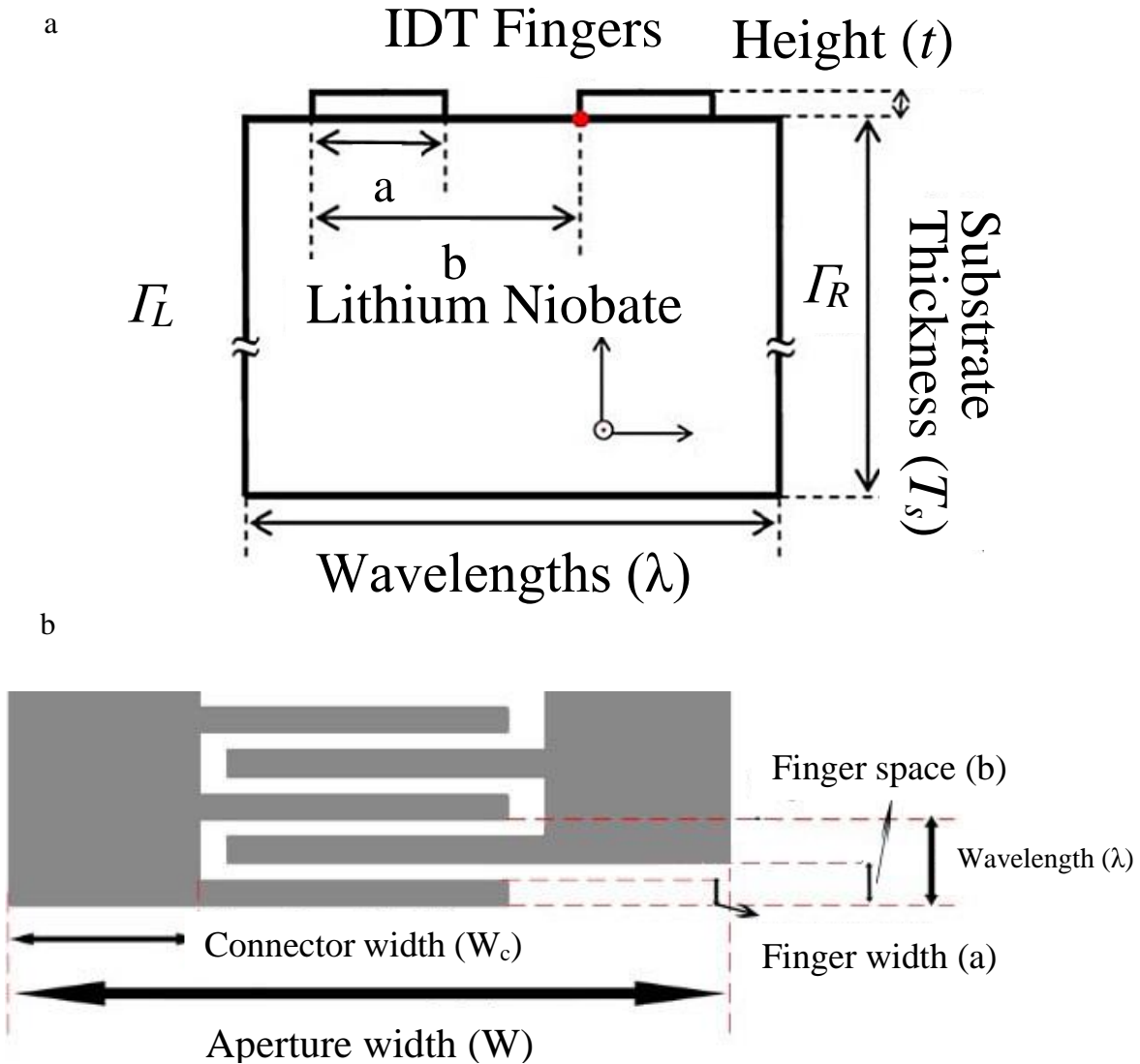


**Figure 3.1.** (a) 2D cell model design of the interdigital transducer in COMSOL; (b) interdigital transducer design parameters employed in this dissertation

For a relatively simple geometry, 2D modeling was sufficient to simulate the Rayleigh wave propagation at the free surface of piezoelectric substrate. After single finger geometry with a width of a wavelength was created, periodic boundary conditions were applied to the left and right edges to simulate infinite pairs of transducers with a very simple model. In order to understand the response of the transducer, the substrate displacement was obtained in the

eigenfrequency module with an input of applied voltage. In this dissertation, this developed simulation was employed to investigate finger metallization ratio, finger thickness ratio and substrate thickness ratio on a 36°YX cut lithium niobate wafer, 128°YX cut lithium niobate substrate and ST cut quartz. The metallization ratio ( $a/b$ ) is defined as the finger width ( $a$ ), as illustrated in Figure 3.1, divided by the space width ( $b$ ). The non-dimensional finger thickness ratio ( $t/\lambda$ ) is defined as finger thickness ( $t$ ) divided by wavelength ( $\lambda$ ), and substrate thickness ratio ( $T_s/\lambda$ ) is defined as thickness  $T_s$  of the substrate divided by wavelength ( $\lambda$ ). These three non-dimensional parameters were used in a 2D model with a parameter sweep study module to demonstrate the effects of different finger designs on the wave propagation phase velocity.

### 3.2.1. Eigenfrequency Analysis

In eigenfrequency analysis, a wavelength cell is created with a periodic boundary condition, as shown in Figure 3.1a. The surface wave was excited by applying 1V of electric potential on one finger while the other finger was connected to the ground. Eigenfrequency is normally used to identify the working frequency range and frequency changes of the SAW device. The electric potential and displacement distribution are also obtained in the eigenfrequency analysis.

### 3.2.2. Parameter Analysis

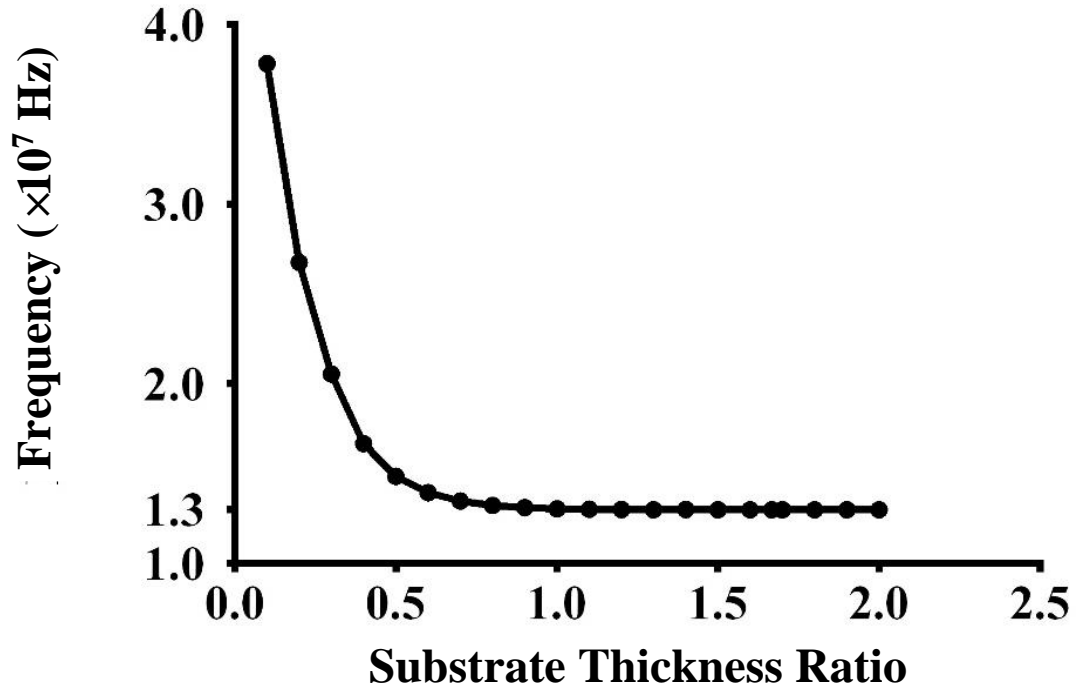
A parameter sweep was used in this study to investigate the finger thickness ratio, metallization ratio, guided layer thickness ratio, substrate thickness ratio and different mass loading on the surface of the substrate. In the 2D design, the finger thickness ratio, metallization ratio and substrate thickness ratio simulation were discussed in detail.

### 3.2.3. Effect of Substrate and Finger Design

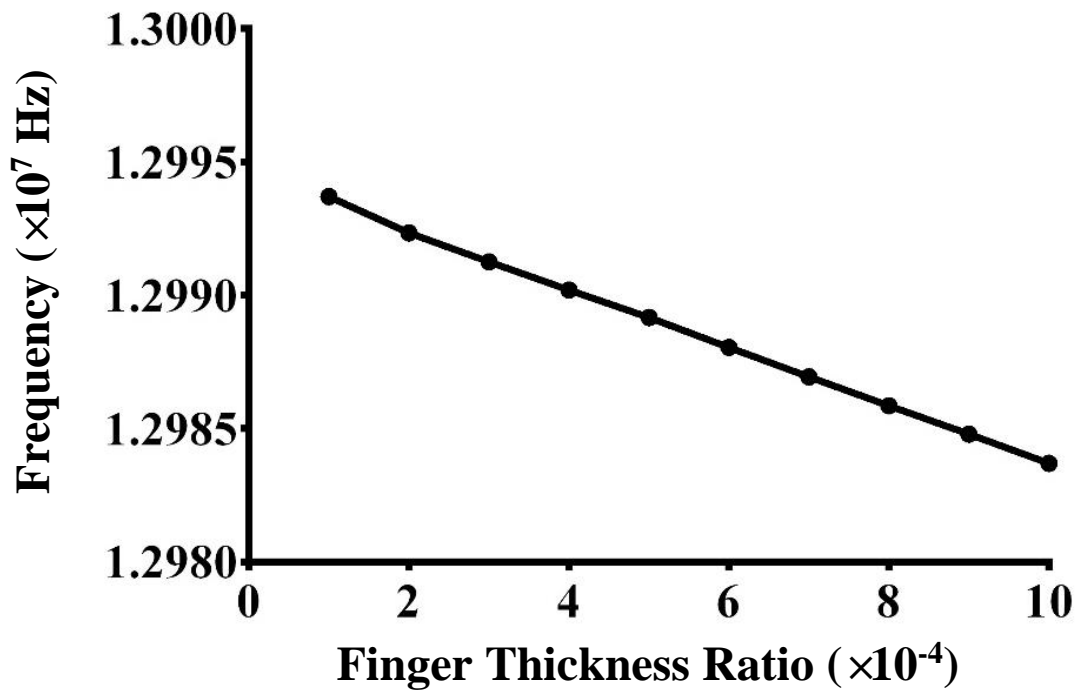
Three surface acoustic wave substrates are investigated in this dissertation lithium niobate 128 °YX cut, ST-quartz and lithium tantalate 36 °YX cut. ST-quartz and lithium tantalate 36 °YX cut generate SH-SAWs on the surface. Rayleigh waves can be excited on a 128 °YX cut lithium niobate surface. In the SH-SAWs model, the wave propagation plane did not coincide with the plane where particles move. But for Rayleigh waves, the particle movement and wave propagation remained in the same plane. Hence, a 2D model is sufficient to simulate 128 °YX cut lithium niobate which excites Rayleigh waves.

Figure 3.2 illustrates how simulated operation frequency as a function of substrate thickness ratio for a 128 °YX cut lithium niobate substrate. One can observe from this figure that increasing the substrate thickness results in decreasing operation frequency in a non-linear fashion. The initial wavelength, metallization ratio and finger thickness is 300 μm, 0.5 and 100 nm in this design. The parametric sweep of the lithium niobate substrate has a thicknesses ratio ( $T_s/\lambda$ ) ranging from 0.1 to 2 as illustrated in Figure 3.2. Figure 3.3 also shows the simulated center frequency as a function of finger thickness ratio for a 128 °YX cut lithium niobate substrate. This figure shows that increasing the finger thickness also decreases the frequency, but this time the decrease occurs in a linear fashion for the range investigated. The wavelength and metallization are the same as shown in Figure 3.2. But the chrome finger thickness ratio ( $t/\lambda$ ) ranged from  $10^{-4}$  to  $10^{-3}$ . Substrate thickness is 500 μm in this case. Figure 3.4 illustrates the simulated center frequency as a function of metallization ratio for a 128 °YX cut lithium niobate substrate. One can observe from this figure that increasing the metallization decreases the operation frequency for the range investigated. The metallization ratio ( $a/b$ ) varied from 0.1 to 0.9 while substrate thickness and finger thickness is kept the same as in prior simulations for fair comparison (500 μm and 100 nm).





**Figure 3.2.** Effect of substrate thickness on the center frequency of IDTs on 128 °YX cut lithium niobate substrate in 2D simulation model



**Figure 3.3.** Effect of finger thickness on the center frequency of IDTs on 128 °YX cut lithium niobate substrate in 2D simulation model

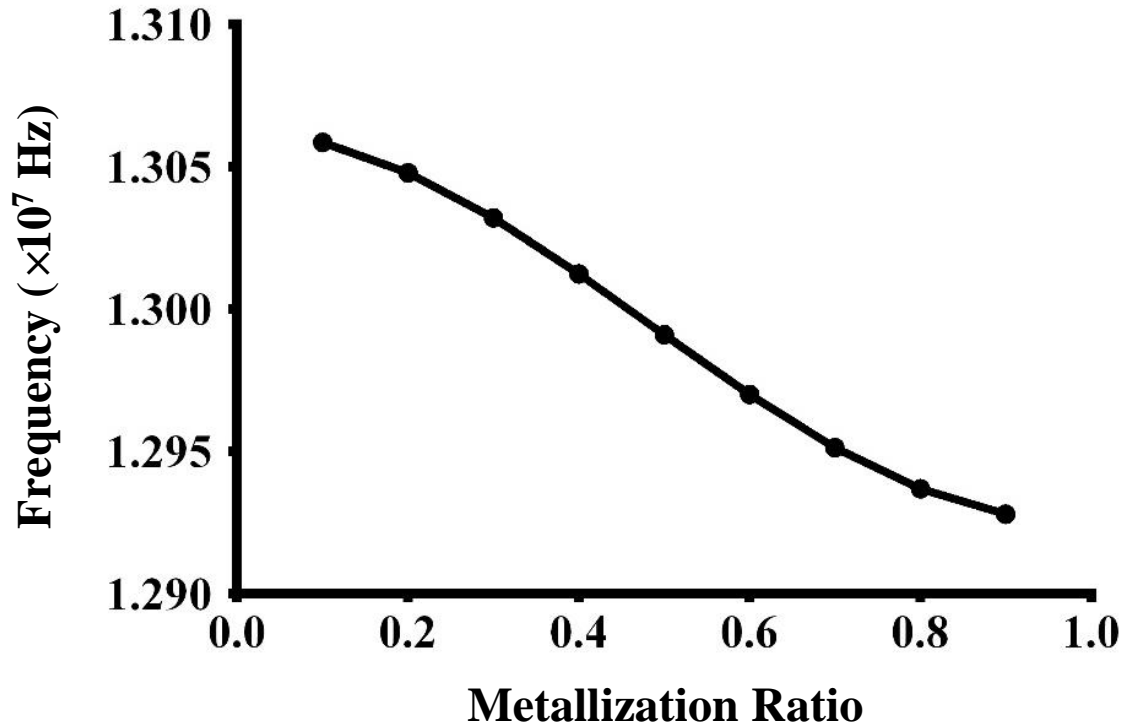


**Figure 3.4.** Effect of metallization ratio on the center frequency of IDTs on 128 °YX cut lithium niobate substrate in 2D simulation model

### 3.3. Interdigital Surface Acoustic Wave Transducer Design with 3D Simulations

The 3D simulation of the SAWs focused on both the finger design and the overall device design. A 3D cell model (as illustrated in Figure 3.5) was built to optimize the finger design by simulating different finger thickness ratios, substrate thickness ratios, metallization ratios and guide layer thickness ratios through an eigenfrequency analysis. Additionally microfluidic channel and SAWs were integrated in a 3D COMSOL simulation to investigate mass loadings and viscosities of the liquid in a microchannel. The simulation results for different viscosities of obtained by changing the glycerol concentration is in detail in Chapter 5, and the mass loading of different concentrations of cells is described in detail in Chapter 6.

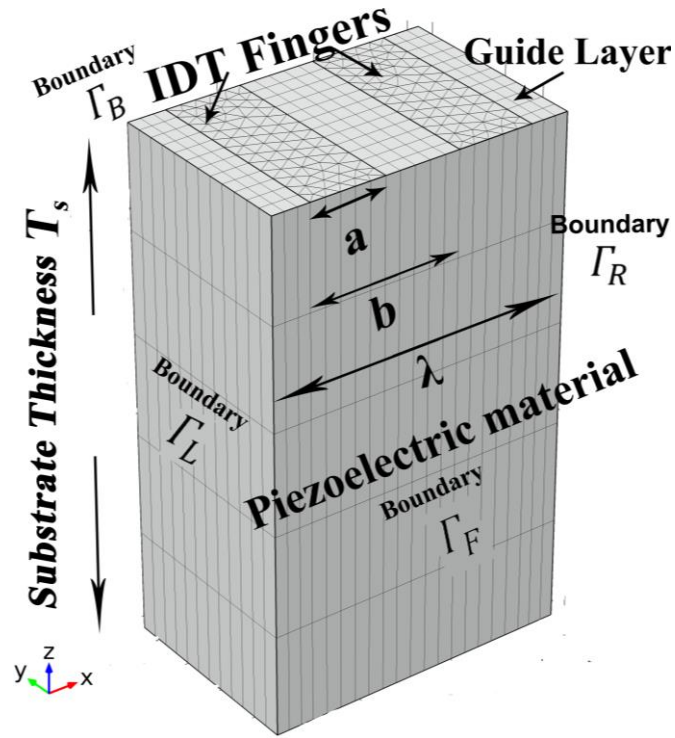


**Figure 3.5.** 3D cell model design of the interdigital transducer in COMSOL

### 3.3.1. Effect of Substrate and Finger Thickness Ratio

The thickness of the IDTs fingers affects the phase velocity on the surface of substrate, which is simulated by using the 3D cell model as illustrated in Figure 3.5. The simulated center frequency as a function of finger thickness ratio is presented in Figure 3.6 for 128 °YX cut lithium niobate substrate, in Figure 3.7 for 36 °YX cut lithium tantalate substrate, and in Figure 3.8 for ST-cut quartz substrate. Phase velocity ( $v$ ) is equal to the frequency, wavelength ( $\lambda$ ) multiplication. Increasing the finger thickness ratio increases the finger thickness, while keeping the wave length constant, resulting in a frequency and phase velocity decrease. One can observe from Figures 3.6, 3.7 and 3.8 that for all three substrate materials, increasing the finger thickness ratio results in decreasing in center frequency. However, a careful comparison among Figures 3.6, 3.7 and 3.8 indicates that the ST-quartz is more sensitive to finger thickness changes compared to the 128 °YX

cut lithium niobate substrate and 36°YX cut lithium tantalate substrate with same chromium electrode layer.

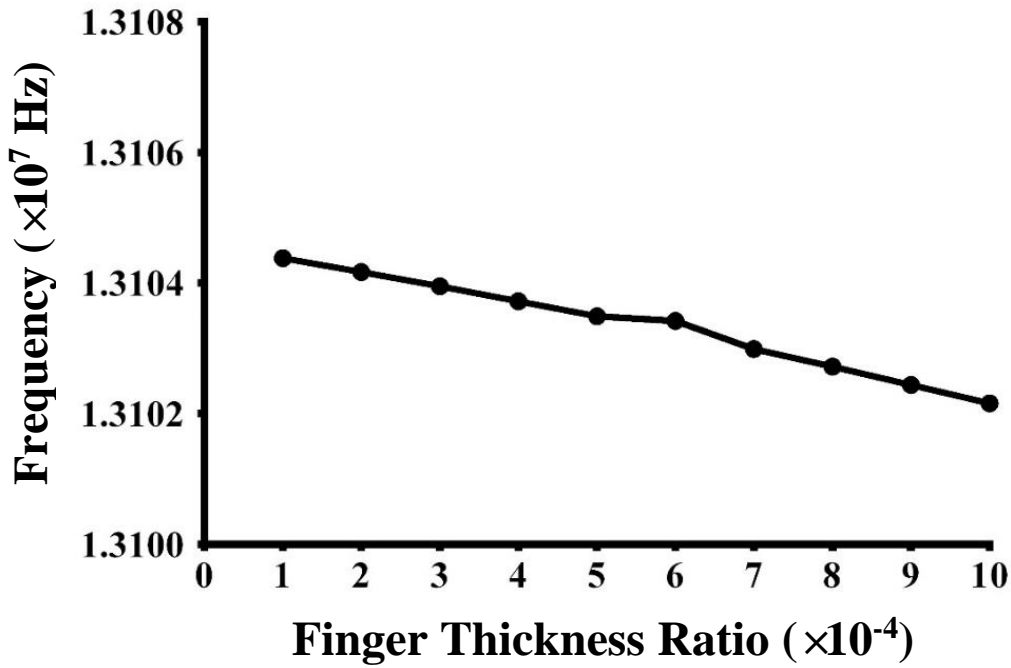


**Figure 3.6.** Effect of finger thickness on the center frequency of IDTs on 128°YX cut lithium niobate substrate

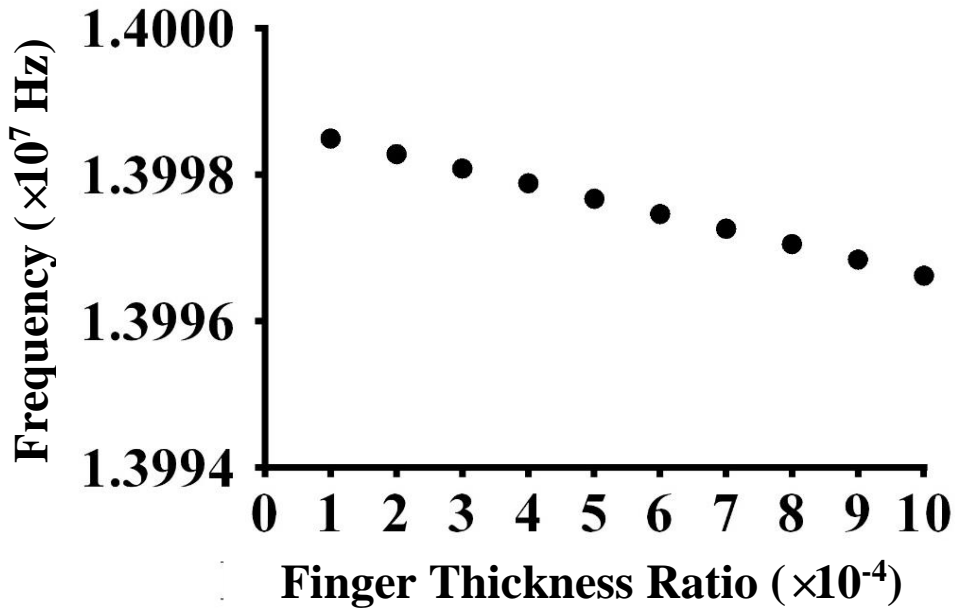


**Figure 3.7.** Effect of finger thickness on the center frequency of IDTs on 36°YX cut lithium tantalate substrate

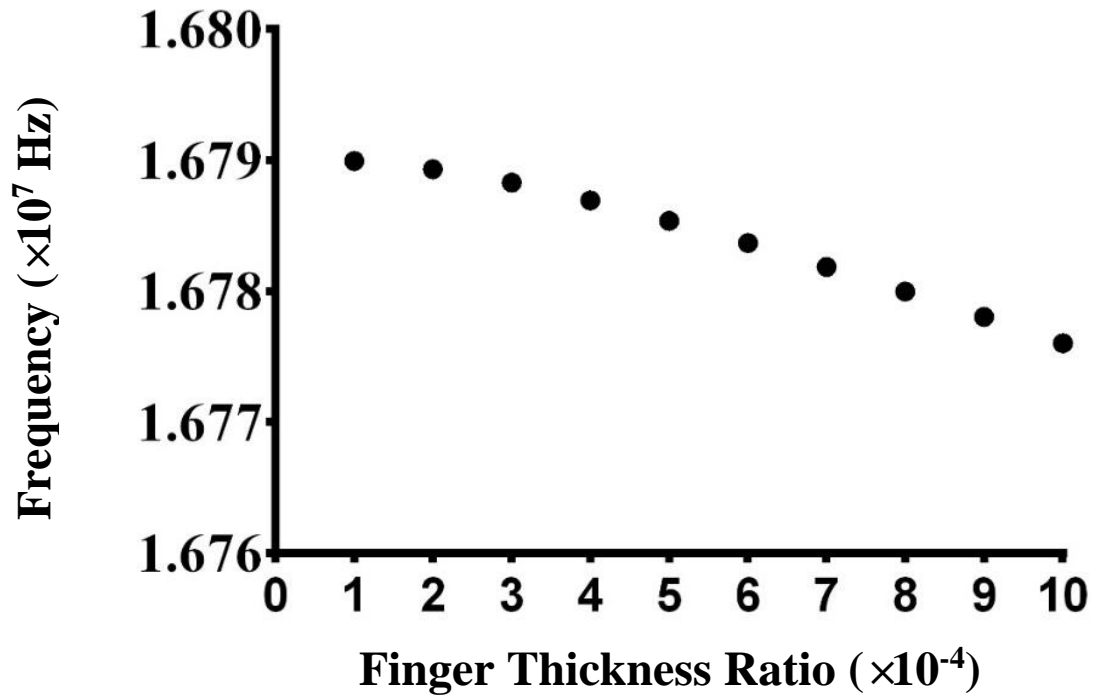


Figure 3.8. Effect of finger thickness on the center frequency of IDTs on ST-cut quartz substrate

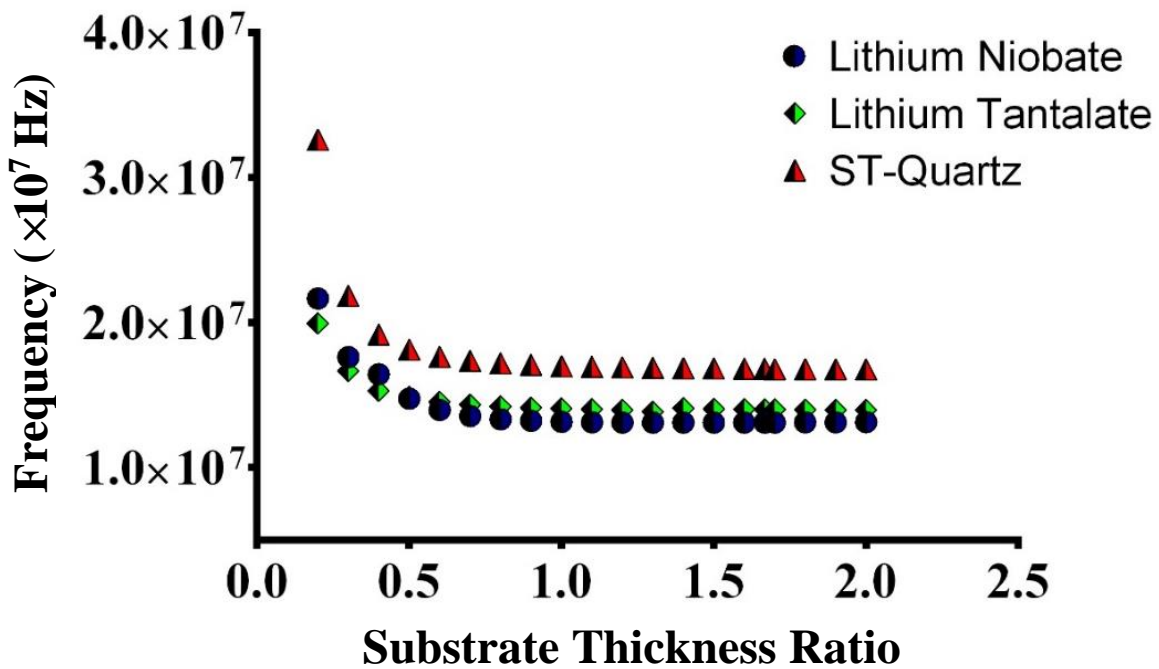
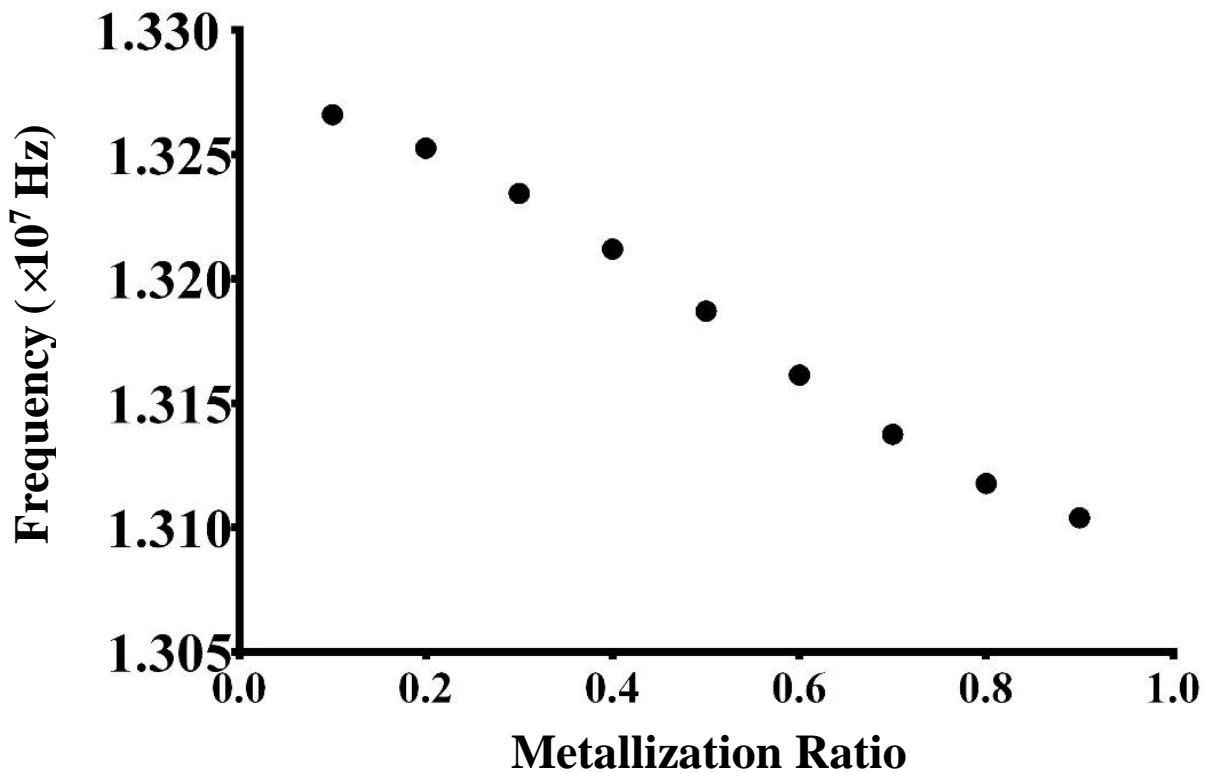


Figure 3.9. Effect of substrate thickness ratio on the center frequency of IDTs on different substrates

Figure 3.9 illustrates simulated center frequency as a function of substrate thickness ratio for 128 °YX cut lithium niobate, 36 °YX cut lithium tantalate and ST-cut quartz substrates. One can observe from Figure 3.9 that substrate thickness significantly affects the frequency and phase velocity of SAWs in the low substrate thickness ratio range from  $0.1\lambda$  to  $0.7\lambda$  for all three substrates investigated. However, once the substrate thickness ratio is above the  $0.7\lambda$ , then the center frequency is independent of the substrate thickness ratio for all three substrates for the substrate thickness ranges investigated.



**Figure 3.10.** Effect of metallization ratio on the center frequency of IDTs on 128 °YX cut lithium niobate substrate

The simulated center frequency as a function of metallization ratio is presented in Figure 3.10 for 128 °YX cut lithium niobate substrate, in Figure 3.11 for 36 °YX cut lithium tantalate substrate, and in Figure 3.12 for ST-cut quartz substrate. One can observe from all these three figures that increasing the metallization ratio results in lowering the operation center frequency;

however, the rate of change of frequency was different among different substrates investigated. For instance, for the ST-cut quartz substrate, the operation frequency changed slightly as a function of the metallization ratio. It should be emphasized that for a conventional IDT design, the metallization ratio is  $\eta=0.5$ , and the finger width is equal to the spacing between fingers, resulting in each spacing and finger width to be  $\lambda/4$ . At this point in this dissertation, it is important to assess whether both 2D and 3D simulations can successfully simulate surface acoustic waves on different substrates. The Rayleigh waves are two-dimensional waves only with a combination of longitudinal and transverse waves. However, Shear Horizontal waves and love waves are three-dimensional waves which are only sufficiently simulated in 3D simulation. Even though both 2D and 3D simulations capture the overall trends of Rayleigh waves successfully, the phase velocities obtained from 2D simulation are generally smaller than the phase velocity of 3D simulations as well as the values reported in literature. From 2D simulation, the Rayleigh waves phase velocity for frequency range investigated is obtained from 3879 m/s to 3915 m/s for 128 °YX cut lithium niobate substrate. In the 3D simulation results, the Rayleigh waves phase velocity ranges from 3979.5 m/s to 3930 m/s for 128 °YX cut lithium niobate substrate, the Shear Horizontal waves phase velocity from 4160 m/s to 4202.4 m/s for 36 °YX cut lithium tantalate substrate, and SH waves phase velocity from 5040 m/s to 5032.5 m/s for ST-quartz. Phase velocity from literature for 128 °YX cut lithium niobate substrate is 3992 m/s<sup>39</sup>, 4212 m/s on the free surface of 36 °YX cut lithium tantalate substrate<sup>46</sup> and 5040 m/s on the free surface of ST-quartz. One can clearly observe the advantage of employing 3D simulation where the simulated and theoretical phase velocities are very close to one another for all substrate materials investigated whereas the results are less accurate for simpler 2D cell design.

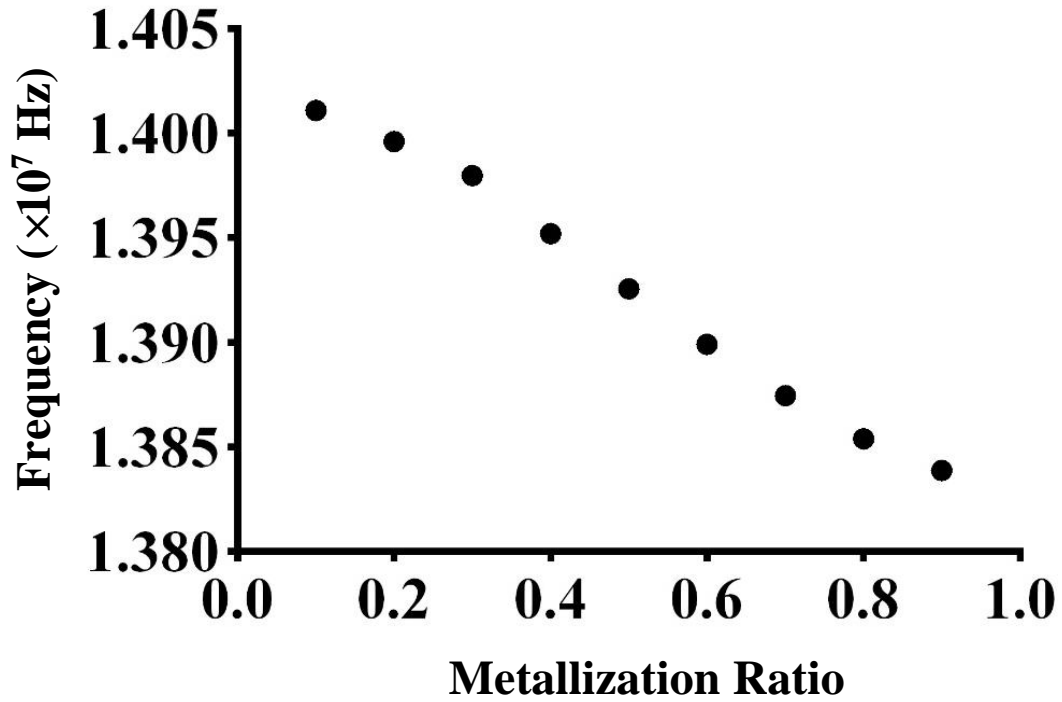


**Figure 3.11.** Effect of metallization ratio on the center frequency of IDTs on 36 °YX cut lithium tantalate substrate

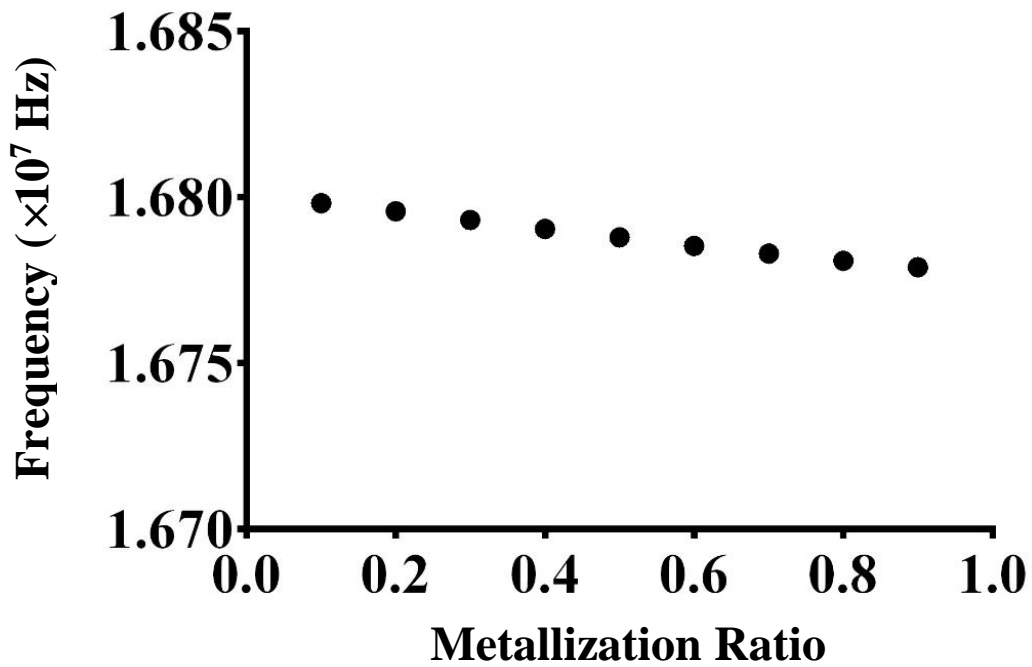


**Figure 3.12.** Effect of metallization ratio on the center frequency of IDTs on ST-cut quartz substrate



The simulated maximum displacement as a function of finger thickness ratio is presented in Figure 3.13 for 128 °YX cut lithium niobate substrate, in Figure 3.14 for 36 °YX cut lithium tantalate substrate, and in Figure 3.15 for ST-cut quartz substrate. The maximum center displacement of IDTs remained almost constant as a function of the finger thickness ratio on the 128 °YX cut lithium niobate and 36 °YX cut lithium tantalate substrates (Figure 3.13 and Figure 3.14). However for ST-quartz, Figure 3.15 shows that increasing the finger thickness ratio from  $1 \times 10^{-4}$  to  $5 \times 10^{-4}$  decreases the maximum center displacement. Comparing Figure 3.13 to Figure 3.14, the Rayleigh wave mode excited by the lithium niobate generates a large displacement on the surface.

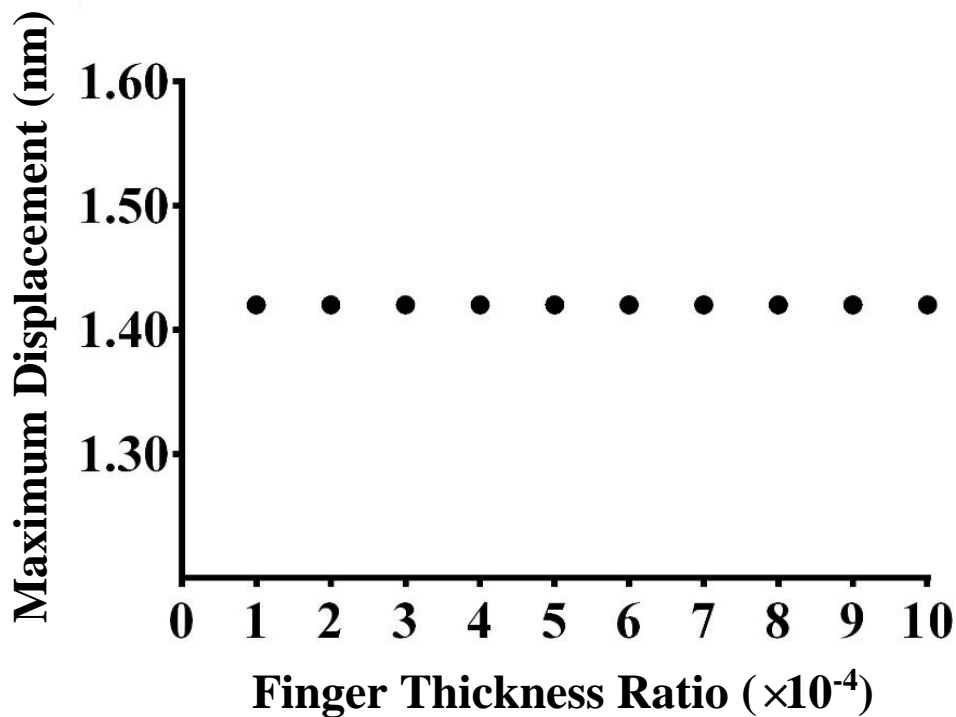


**Figure 3.13.** Effect of finger thickness on the center maximum displacement of IDTs on 128 °YX cut lithium niobate substrate

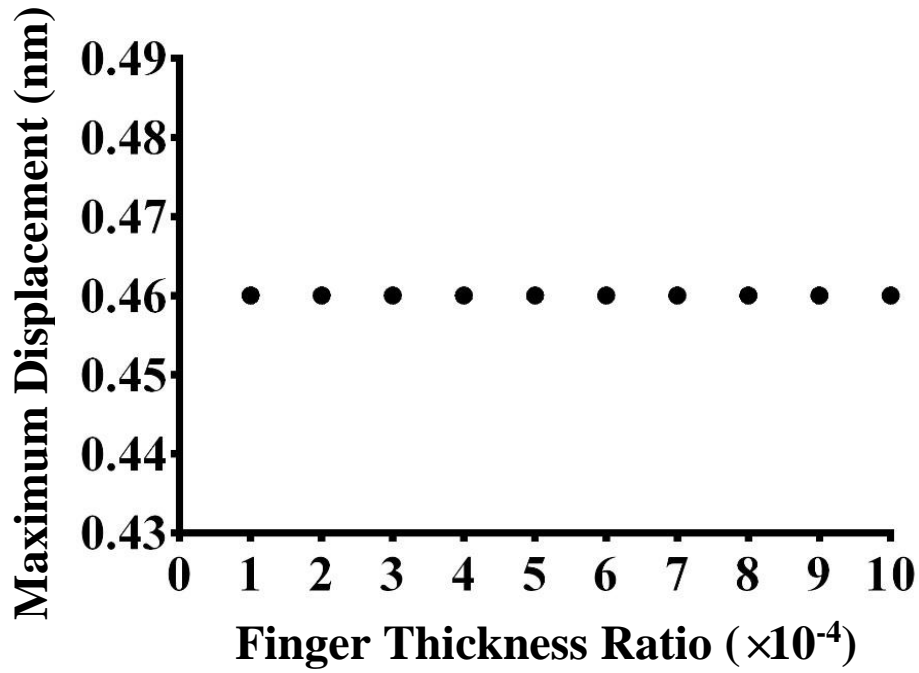


**Figure 3.14.** Effect of finger thickness on the center maximum displacement of IDTs on 36 °YX cut lithium tantalate substrate

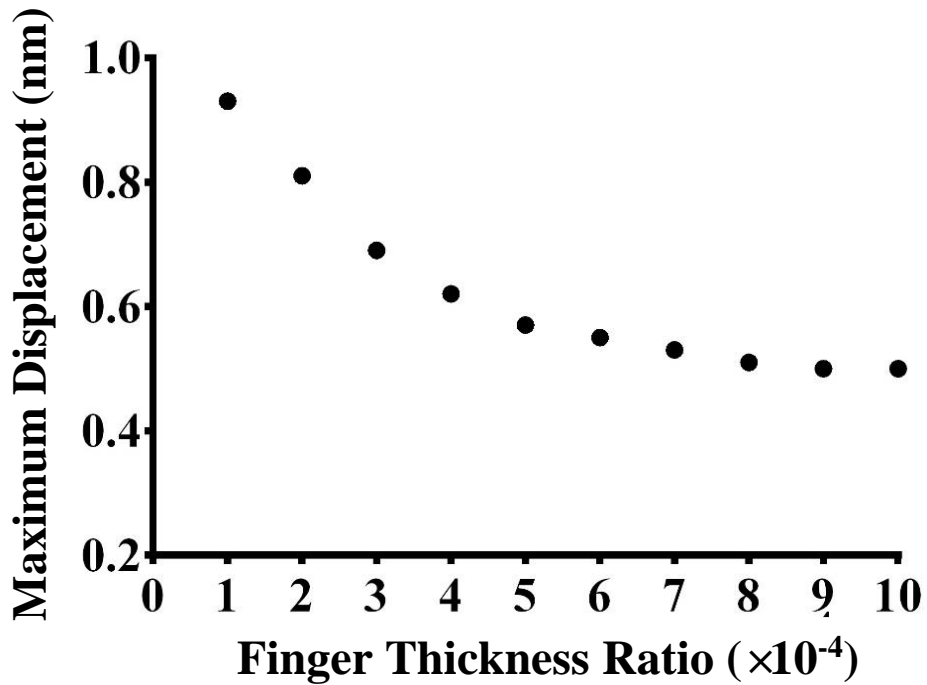


**Figure 3.15.** Effect of finger thickness on the center maximum displacement of IDTs on ST-cut quartz substrate

We also investigated the effect of substrate thickness ratio on maximum displacement for 128° YX cut lithium niobate substrate (Figure 3.16), for 36° YX cut lithium tantalate substrate (Figure 3.17), and for ST-cut quartz substrate (Figure 3.18). For 128° YX cut lithium niobate (Figure 3.16) and ST-cut quartz substrate substrates (Figure 3.18), the maximum displacement decreases when the substrate thickness ratio is increased from  $0.2\lambda$  to  $0.7\lambda$ . However, from  $0.8\lambda$  to  $2.0\lambda$ , the maximum displacement increases as the substrate thickness ratio increases. This behavior can be explained by the fact that for thin substrate thickness ratio ranges, the substrate thickness is much lower than the wavelength, hence the wave excited by the IDTs is not a pure Rayleigh wave or a shear horizontal wave. For the same thickness ratio, the lithium niobate wafer excites the largest maximum displacement compared to lithium tantalate and ST-quartz wafer alternatives. In the case of the lithium tantalate substrate in Figure 3.17, the maximum displacement is loosely related to the substrate ratio for the range investigated.

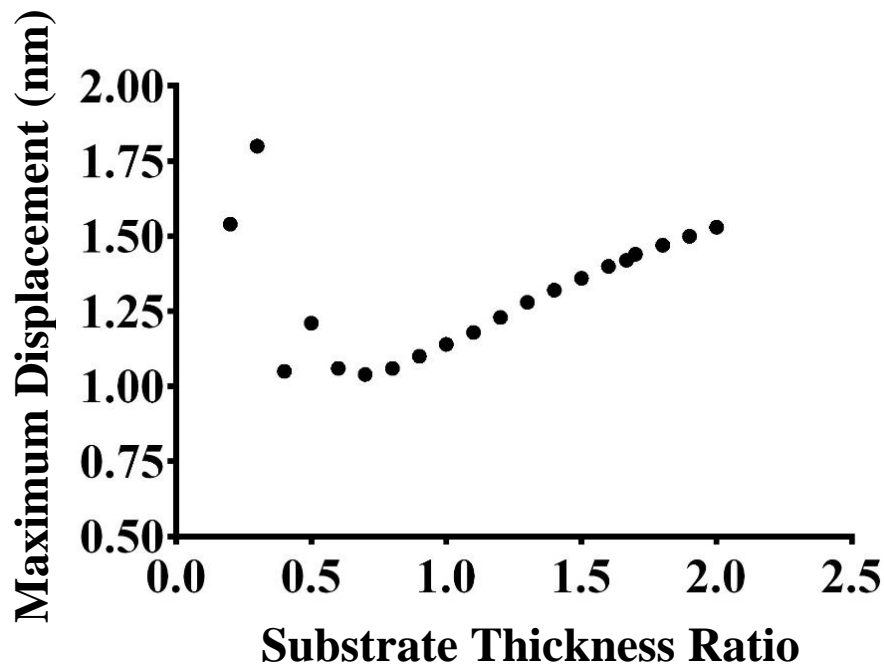


**Figure 3.16.** Effect of substrate thickness on the center maximum displacement of IDTs on 128° YX cut lithium niobate substrate

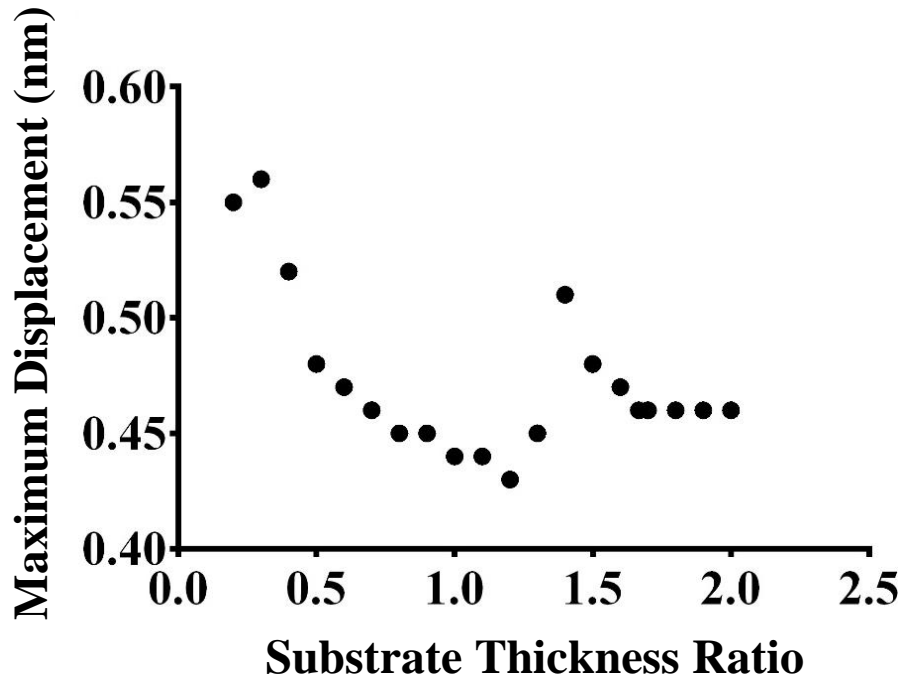


**Figure 3.17.** Effect of substrate thickness on the center maximum displacement of IDTs on 36 °YX cut lithium tantalate substrate

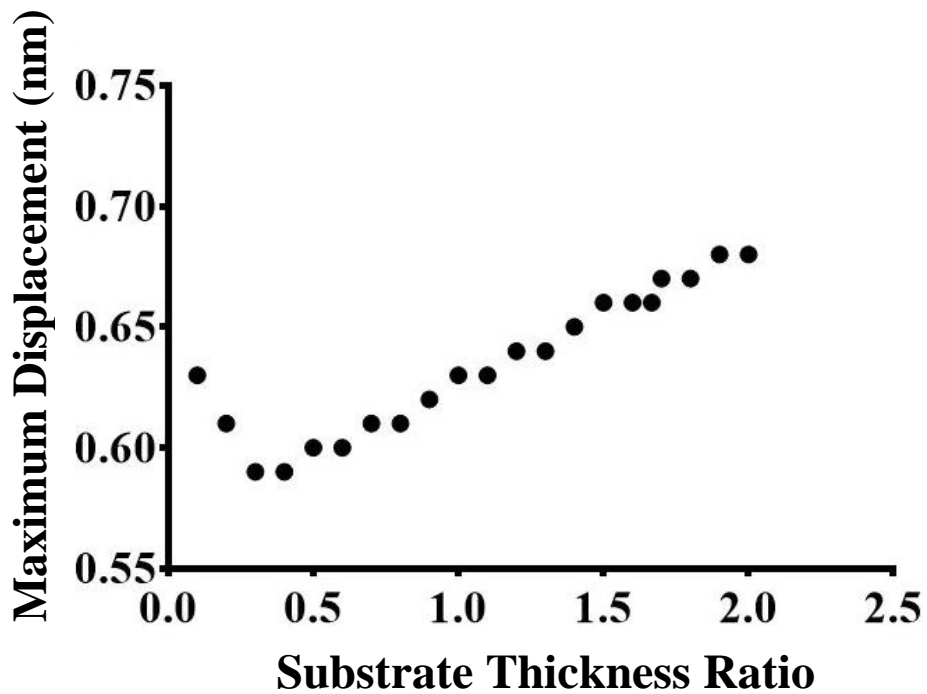


**Figure 3.18.** Effect of substrate thickness on the center maximum displacement of IDTs on ST-cut quartz substrate

Furthermore, we also investigated the effect of metallization ratio on maximum displacement for 128°YX cut lithium niobate substrate (Figure 3.19), for 36°YX cut lithium tantalate substrate (Figure 3.20), and for ST-cut quartz substrate (Figure 3.21). The metallization ratio is defined as the finger width divided by the finger spacing. For 128°YX lithium niobate substrate (Figure 3.19), the maximum displacement is independent from the metallization ratio. However the maximum displacement is increased for both 36°YX cut lithium tantalate and ST-cut quartz substrates for increasing metallization ratio. This behavior may be explained by investigating the definition of metallization ratio, which illustrates that by increasing the metallization ratio IDTs finger width is decreased, potentially resulting in amplified surface displacements as opposed to wider finger widths.

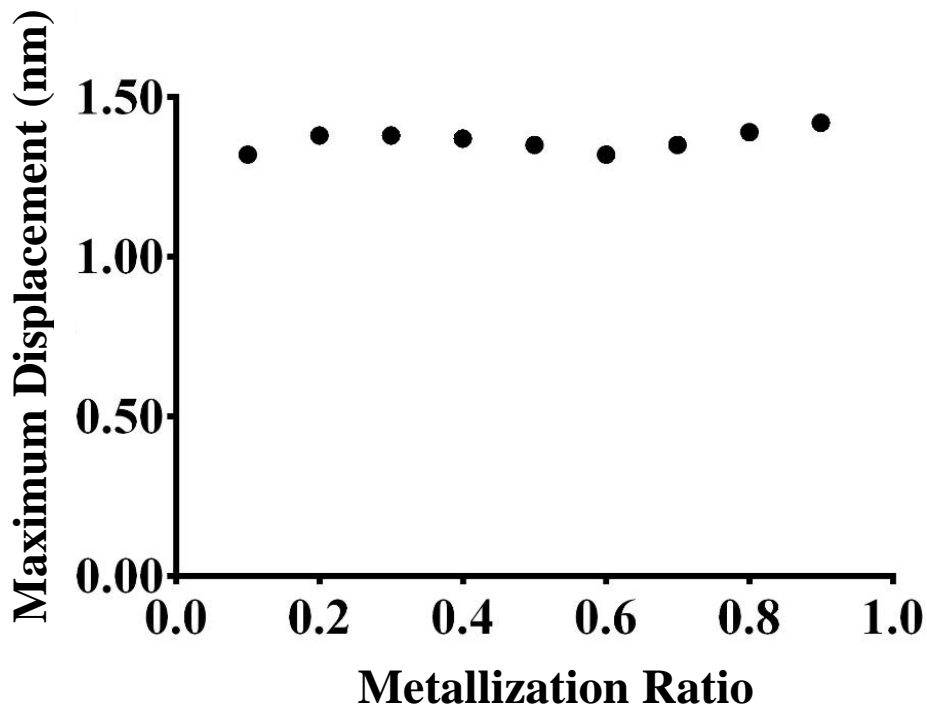


**Figure 3.19.** Effect of metallization ratio on the center maximum displacement of IDTs on 128°YX cut lithium niobate substrate

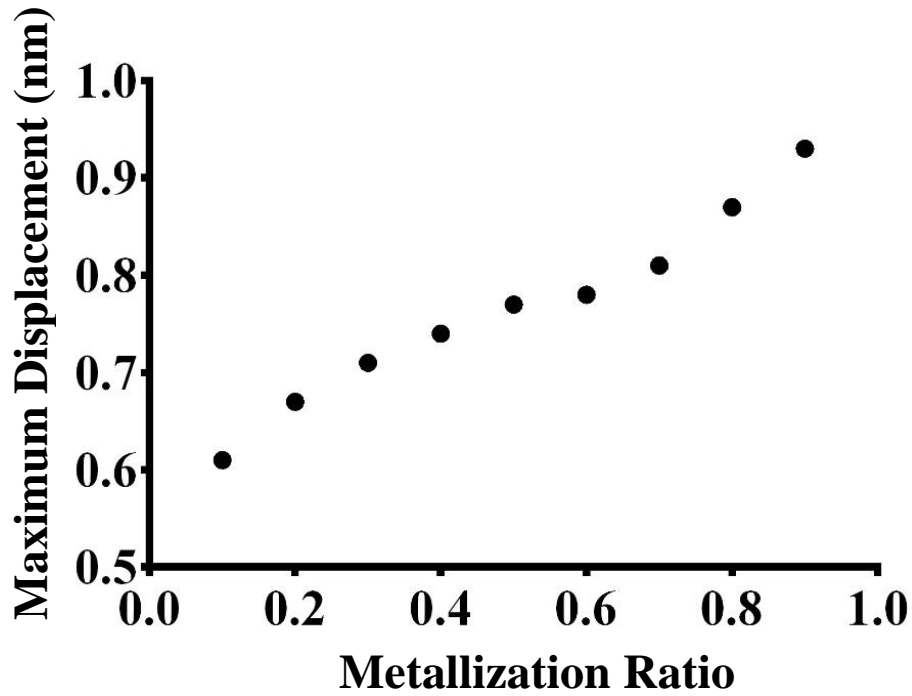


**Figure 3.20.** Effect of metallization ratio on the center maximum displacement of IDTs on 36°YX cut lithium tantalate substrate

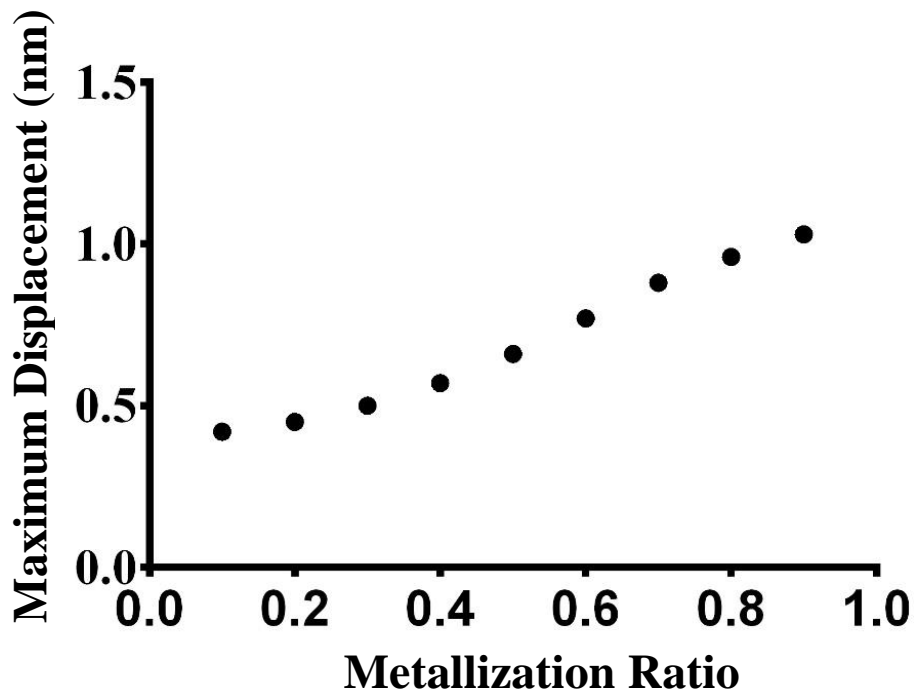


**Figure 3.21.** Effect of metallization ratio on the center maximum displacement of IDTs on ST-cut quartz substrate

### 3.3.2. Effect of Guide Layers in 3D Cells

Since wave travel velocity is a function of different guide layers, the effect of various guided layer material selection does impact the operation of the SAW sensors and transducers. The dielectric properties of different guide layers also affect wave properties differently. The effect of guided layer material on the center frequency is investigated for lithium tantalate (Figure 3.22) and St-quartz substrates (Figure 3.23). Figure 3.22 illustrates that increasing  $\text{TiO}_2$  layer thickness deposited on lithium tantalate increases the surface acoustic wave frequency. This increase, also indicates an increase in phase velocity. This phenomenon is in contrast to the ZnO layer and  $\text{SiO}_2$ , which have the opposite effect to  $\text{TiO}_2$  layer existence. Such a relation has been discussed in a prior publication<sup>47</sup>. However, as illustrated in Figure 3.23 increase in the thickness of all guide layers materials investigated, caused a reduction in the frequency for ST-cut quartz substrate.

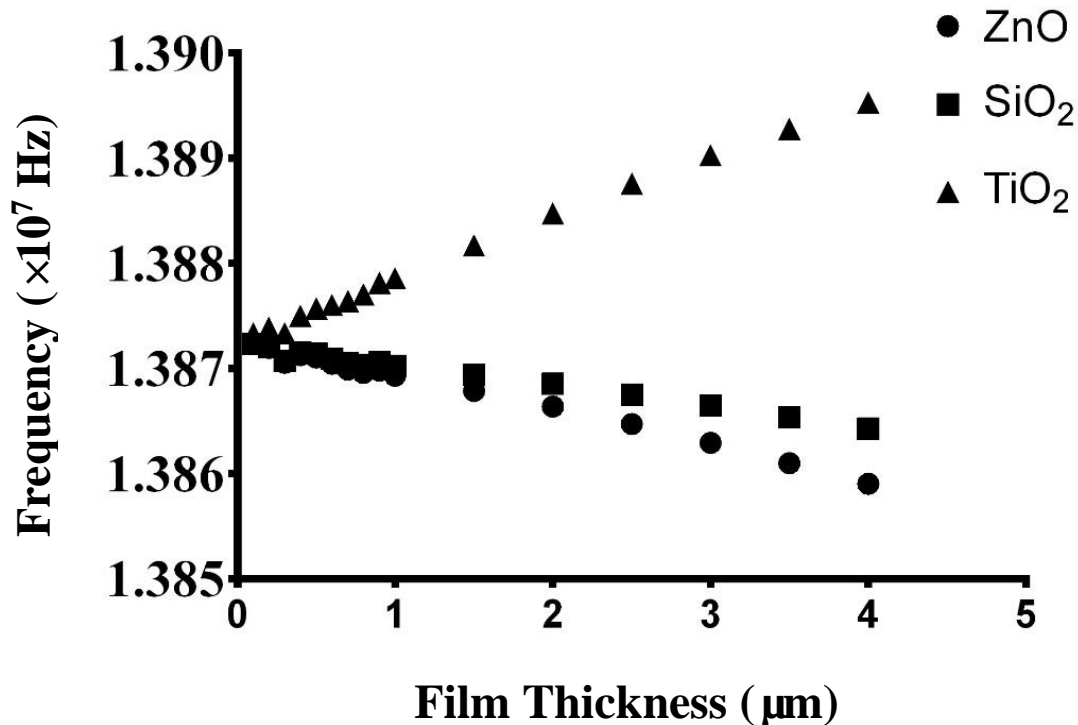


**Figure 3.22.** Effect of different guide layer thicknesses on the center frequency of IDTs on  $36^\circ\text{YX}$  cut lithium tantalate substrate

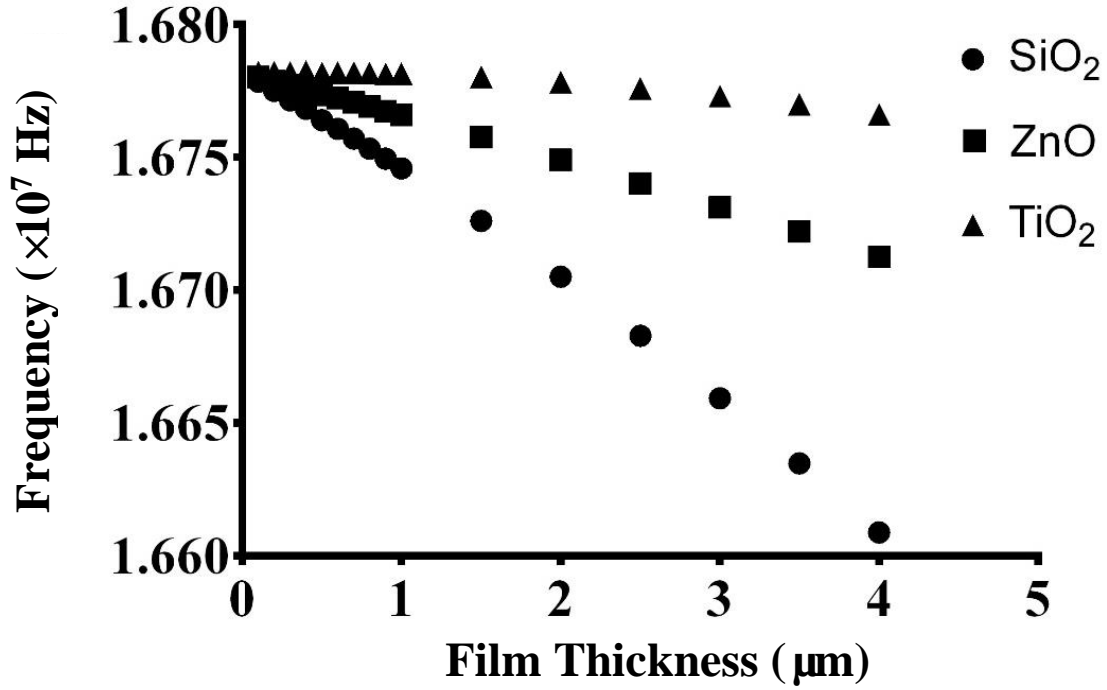


**Figure 3.23.** Effect of different guide layer thicknesses on the center frequency of IDTs on ST-cut quartz substrate

### 3.3.3. Frequency Sweep Analysis in 3D Model

Additionally, a frequency sweep analysis was conducted to demonstrate the acoustic wave propagation at the surface wave mode frequencies. After the model was created as illustrated in Figure 3.24, device resonance frequency was obtained by using the frequency domain in COMSOL. Voltage potential (0.5 V) was applied to the finger at transmit side and then a voltage tester probe was applied at receiver side for the receiver the voltage response. The insertion loss is calculated by Equation 3.1<sup>48</sup>.

$$IL = 20 \times \log_{10} |V_{output}/V_{input}| \quad \text{Equation 3.1}$$

Then the sweep frequency range was applied to the system with range from 10 to 15 MHz and to each step of 0.01 MHz. Figure 3.25 illustrates the obtained frequency spectrum response for 128 °YX cut lithium niobate, a 500 μm substrate thickness, 100 nm finger thickness and a metallization ratio of 0.5. Comparison between the frequency response illustrated in Figure 3.25



and the experimentally measured frequency response is discussed in detail in Chapter 5 of this dissertation.

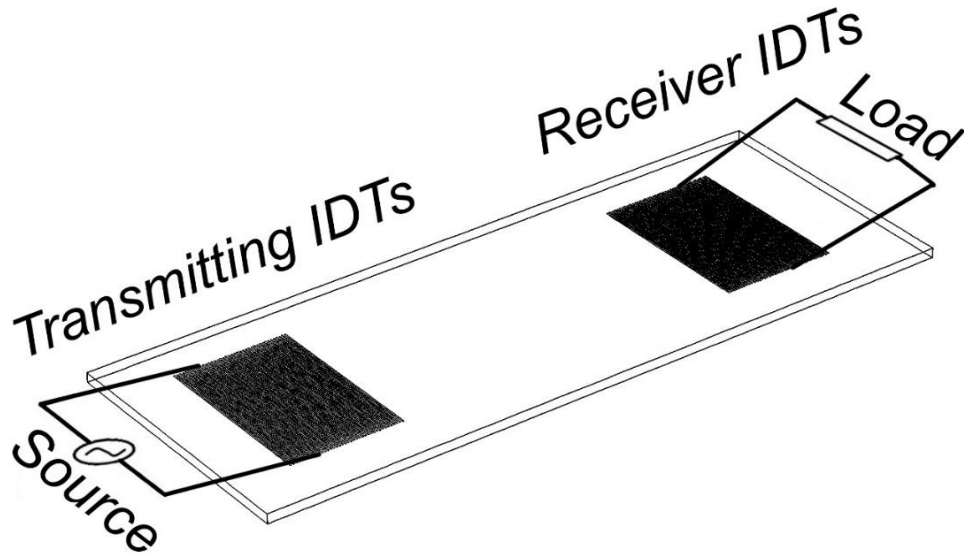


**Figure 3.24.** Realistic model to simulate the responses of receiver IDTs

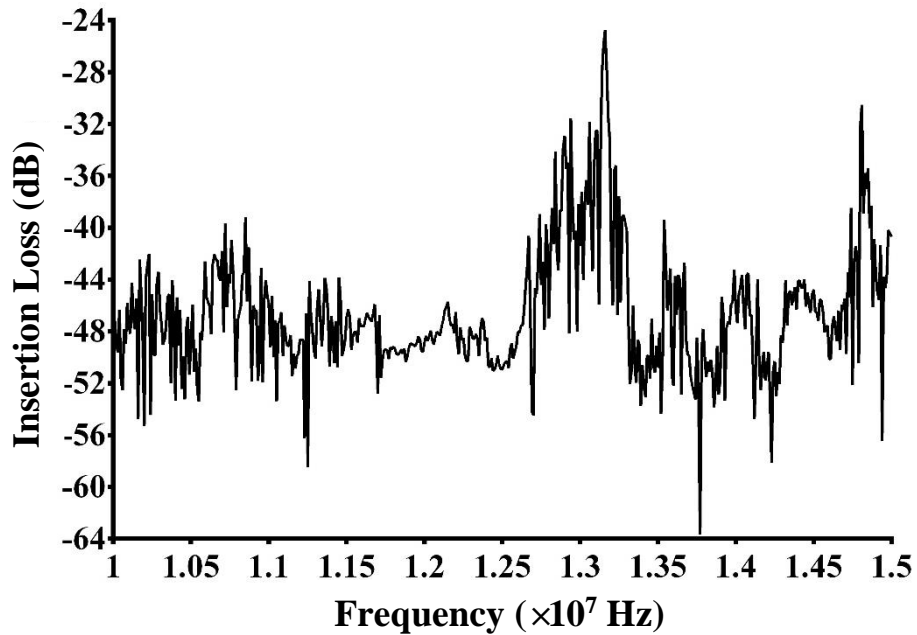


**Figure 3.25.** Frequency spectrum simulation results of 128°YX cut lithium niobate substrate by using frequency sweep analysis methods

## CHAPTER 4. SURFACE ACOUSTIC WAVE BASED MICROFLUIDIC PUMP

### 4.1. Note to Reader

The manuscript and the results presented in this chapter have been previously published<sup>49</sup> and are utilized with permission of publisher.

### 4.2. Introduction

Pumping, mixing and separation in microfluidic systems are actively investigated due to increased demand for low-cost and portable devices for biomedical, chemical and mechanical applications. Many fairly high-efficiency devices have been thoroughly investigated for mixing<sup>50-52</sup> and separation<sup>53-56</sup> purposes. Pumps are one of the key components for delivering and controlling flow in microfluidic systems. Typically, liquids are difficult to pump in microchannel due to having a low Reynolds number well below 10. At low Reynolds numbers, friction forces dominate the pumping forces and liquid appears to be more viscous than it is, resulting in large flow resistances and laminar flow profile. Currently, the most widely used types of pumps in microfluidic systems are mechanical and electrical pumps<sup>57,58</sup>. However, mechanical pumps need high power and electrical pumps need high voltage for efficient operation. SAW-based droplet manipulation on free surfaces has been reported to have high velocity, up to several centimeters per second<sup>59</sup>. However, only efficient droplet pumping on free surfaces, not within a microfluidic channels, has been reported. As compared to alternatives, liquid manipulation and pumping with SAW is a non-contact technique capable of precise and highly repeatable flow manipulation. Also, SAW pumps do not require high power or voltage for high-efficiency operation.

Previous studies reported that SAWs can only push liquids in a closed microchannel for a very short distance (1.1 mm), which is essentially a filling process from outside the channel with very low filling speed in the SAW propagation direction. However, microfluidic applications necessitate not just forcing liquid into a microchannel with only a few nanoliters to one hundred nanoliters liquid volume<sup>60,61</sup> but precise fluid manipulation within a microchannel<sup>62</sup>. A recent surface-wave-driven pump accomplished continuous liquid pumping inside a polydimethylsiloxane (PDMS) closed channel<sup>63</sup>. However, this device requires water and glass layers in the design between substrate and channel. The existence of precisely controlled water and glass layers limits its reliability, repeatability and mass production potential. In this dissertation, we introduce a novel integrated SAW-based liquid delivery and precise manipulation within a microchannel that does not involve a filling or sucking process. We demonstrate high speed, large volume delivery and manipulation from a long distance with low sample media loss. PDMS is widely used as a biocompatible material with advantages of low reflection effect on SAW propagation, wide temperature range and high optical transparency<sup>64</sup>. The device employs a hydrophobic surface coating (Cytop) on the microchannel to decrease the friction force and increase bonding. When compared to other closed-channel micropumps in the literature, this device can precisely manipulate a liquid inside a microchannel over a long distance of up to 8 mm without requiring high power input.

### **4.3. Device Operation, Simulation and Design**

Figure 4.1 illustrates a conceptual view of the SAW-based fluid manipulation and pumping method investigated in this study. After surface waves are generated by judiciously designed interdigital transducers (IDTs), the waves propagate toward the microchannel from the IDTs and interact with the liquid located in the channel. The compressional component of the wave is

diffracted at the Rayleigh angle into the fluid. When the surface acoustic waves travel through the substrate, the temperature increases as the applied voltage is increased<sup>65</sup>. Hence, the IDTs transfer the heat to the air and liquid inside the microchannel. As the temperature of the air and water is increased due to wave propagation, the saturation pressure of water vapor will increase. This will cause an increase in the evaporation rate, pushing the liquid forward. Therefore, the force that causes fluid manipulation in the channel is the resultant force of the body force and expansion force that moves the liquid with low power consumption.

$$\frac{dN_e}{dt} = A_e \alpha_v \frac{1}{\sqrt{2\pi m k T}} (P_e - P) \quad \text{Equation 4.1}$$

$$\rho_w = \frac{P_e}{RT} M \quad \text{Equation 4.2}$$

From the Hertz-Knudsen formula (Equation 4.1)<sup>66</sup>, which is expressed as the absolute rate of evaporation at the liquid and vapor interface, the evaporation rate can be estimated with temperature ( $T$  is temperature of the liquid) and vapor pressure ( $P_e$  and  $P$  are the equilibrium vapor pressure and ambient hydrostatic pressure, respectively). In Equation 4.1,  $m$  is the mass of the liquid,  $k$  is the Boltzmann constant,  $\alpha_v$  is the sticking coefficient and  $A_e$  is the evaporating surface of area. In the majority of applications, the evaporation rate is small and the expansion force is negligible. However, when the temperature of the liquid is increased from room temperature (22 °C) to 38 °C as a result of propagating the acoustic wave, the evaporation rate for the liquid can be estimated as  $1.353 \times 10^{-5}$  µl/s ( $1.353 \times 10^{-11}$  kg/s). Note that this calculation was performed for a microchannel with 500 µm width, 70 µm height and 0.22 µl media volume. The density of the water vapor can also be estimated (Equation 4.2)<sup>67</sup>. From the evaporation rate and vapor density, the volumetric vapor generation rate can be obtained as 0.01 µl/s. As compared to the small liquid volume of 0.22 µl, vapor generation rate will apply a significant expansion force on the liquid.

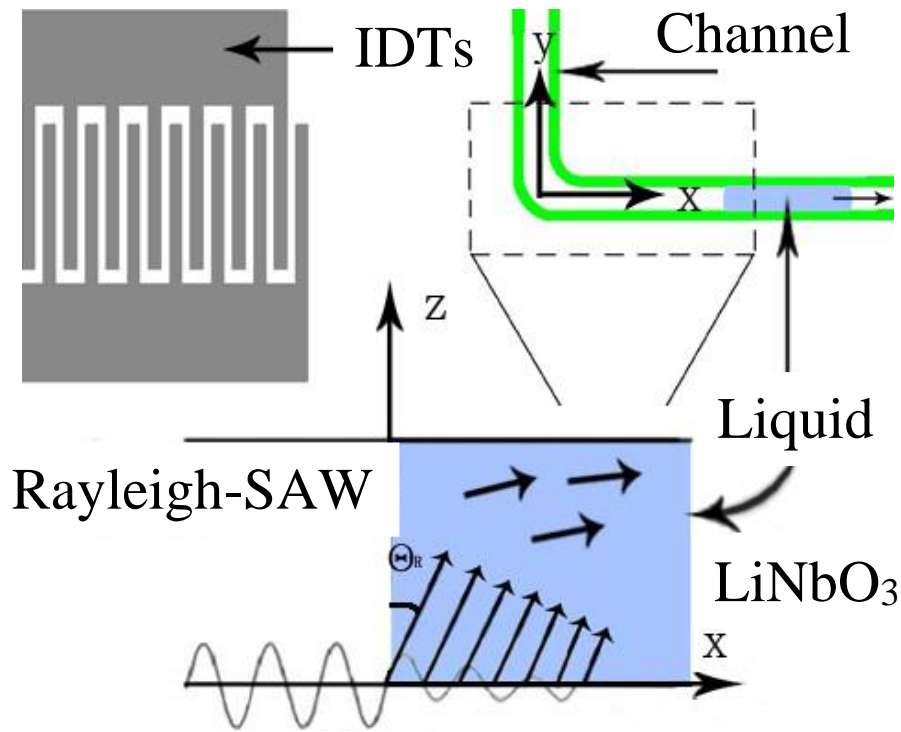


**Figure 4.1.** Conceptual view of the liquid pumping and manipulation induced by surface acoustic waves

A finite element model simulation (FEM) was conducted as part of this study to optimize the design parameters by using the commercial COMSOL Multiphysics 4.4 software<sup>68,69</sup>. As illustrated in Figure 4.2, we simulated only a single wavelength portion of the entire SAW device to simplify the geometry and reduce the computing power. In the simulation, the structure and electric potential boundaries ( $\Gamma_L$  and  $\Gamma_R$  as indicated in Figure 4.2a) were set as periodic in nature to simulate multiple pairs of IDT fingers with a simplified geometry. This model allowed us to investigate the SAW velocity as a function of the IDT finger thickness and its material. We investigated the effect of the gold and chromium finger heights ranging from 90 nm to 1  $\mu\text{m}$  on the transducer frequency response. An optimized layer thickness and materials will result in operation frequency closer to the design frequency.

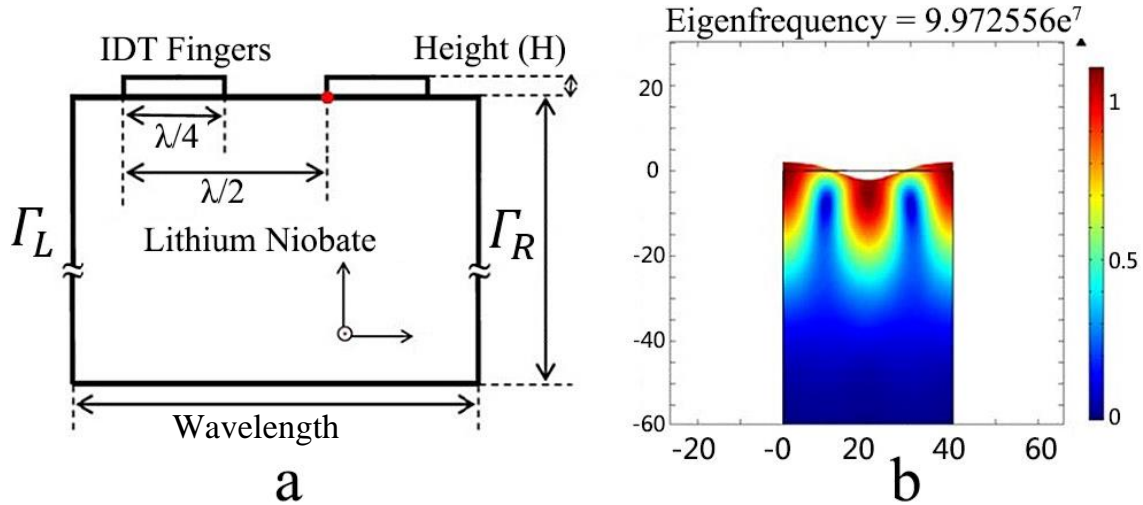


**Figure 4.2.** (a) SAW transducer geometry employed in the simulations; (b) profile of the IDT fingers formed by 100 nm chromium deposited on a 500  $\mu\text{m}$  127.8° lithium niobate substrate

The first group of simulations was conducted by employing the eigenfrequency module of the COMSOL to obtain the effect of different heights and materials on the design frequency (Figure 4.3a). For a constant substrate thickness of 500  $\mu\text{m}$  and wavelength ( $\lambda$  as indicated in Figure 4.2a) of 40  $\mu\text{m}$ , the theoretical design resonance frequency turns out to be 99.75 MHz ( $f=V_{\text{saw}}/\lambda$ ). It should be highlighted that the effects of finger height and substrate thickness are not captured in the theoretical resonance frequency calculation that is employed by many researchers. However, as can be clearly observed from Figure 4.3a, the operation frequency of the device is a function of the IDT finger height. In fact, if one employs gold (Au) with chromium (Cr) as the adhesion layer, the operation frequency is a significant function of the finger height. For instance, if one uses a 0.5  $\mu\text{m}$ -thick finger in the design, the actual operation frequency is shifted to 95.5 MHz from 99.75 MHz. Employing chromium as the IDT finger material results in far less variation in the operation frequency for the entire range of finger heights investigated in this study. A second group of simulations was conducted to investigate the effect of substrate thickness on the operation frequency of the SAW devices (Figure 4.3b). One can observe from this figure that the effect of substrate thickness on the device operation frequency is minimal. In fact, this is an

important result in that many of the wafer substrate manufacturers do not specify the exact wafer thickness but rather substrate thickness range (such as 500  $\mu\text{m}$ -550  $\mu\text{m}$ ). Hence even with the existence of this variation, the operation frequency stays almost constant. It should be highlighted that these simulations were conducted for 100 MHz operation frequency; for applications requiring high-frequency operation (such as in the GHz range), the effect of substrate thickness may in fact become more significant. Based on these simulation studies, we employed a 100 nm chromium IDT finger material patterned on a  $\sim 500 \mu\text{m}$  lithium niobate substrate.

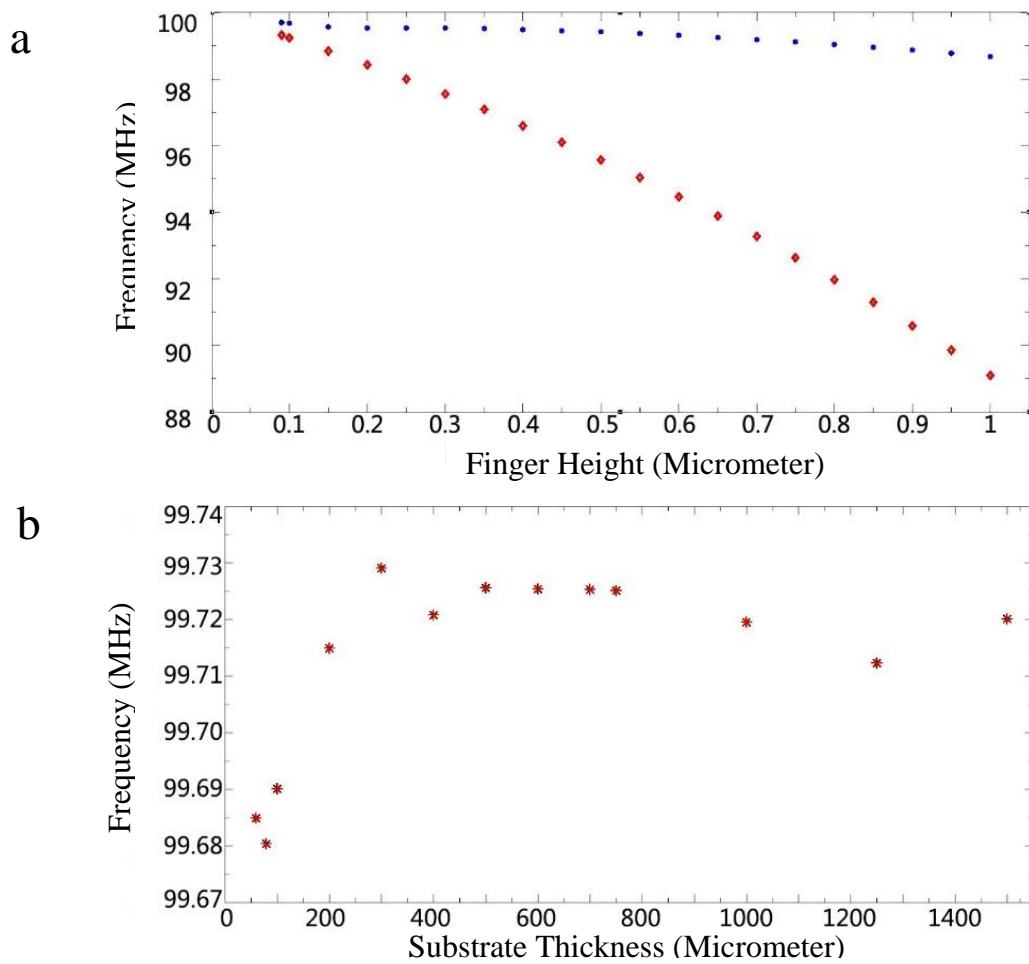


**Figure 4.3.** (a) Simulated operation frequency as a function of IDT finger height and material selection; (b) simulated operation frequency as a function of substrate thickness

Table 4.1 illustrates the final design parameters of the IDTs used in this study. The wavelength, width and pitch of the IDT fingers, and aperture were designed as 40  $\mu\text{m}$ , 10  $\mu\text{m}$  40

$\mu\text{m}$ , and 5 mm, respectively. Two different channel widths were used: 500  $\mu\text{m}$  and 250  $\mu\text{m}$ . The channel height was kept constant at 70  $\mu\text{m}$ . Different channel widths were investigated to quantify the effect of the liquid velocity. The transducer operation (resonant) frequency was obtained by the ratio of the velocity of the propagating wave to the wavelength ( $\lambda$ );  $f=V_{\text{saw}}/\lambda$ .

**Table 4.1.** Device parameters used for the design and fabrication of the IDT transducers.

Wavelength ( $\lambda$ )	40 $\mu\text{m}$	Channel width 1	500 $\mu\text{m}$
Finger width	10 $\mu\text{m}$	Channel width 2	250 $\mu\text{m}$
Finger pitch	40 $\mu\text{m}$	Channel height	70 $\mu\text{m}$
Number of fingers	50 pairs	Operation frequency	97.75 MHz

#### 4.4. Transducer Fabrication and Microchannel Integration

The surface acoustic wave pump was fabricated in four steps: patterning of interdigital transducers (IDTs) on a lithium niobate wafer, PDMS microchannel fabrication, Cytop layer coating, and bonding of the PDMS microfluidic channel to the lithium niobate wafer housing the IDTs<sup>70</sup>. Figure 4.4 illustrates the fabrication process flow of the SAW pumping device. The IDTs were formed from Y-cut X-propagation lithium niobate wafer (128° LiNbO<sub>3</sub>, Universitywafer, MA, USA). After rinsing the lithium niobate substrate with acetone, methanol and DI water, a 100nm chrome was deposited by using the CRC sputtering system. Then, a 1.6  $\mu\text{m}$ -thick photoresist layer (S1813, Shipley, Marlborough, MA, USA) was spun on the lithium niobate substrate. After exposure and developing, the chrome was etched by the chrome etchant (CR-7S, Cyantek, Fremont, CA, USA). IDT fabrication was then completed after the final step of photoresist stripping.



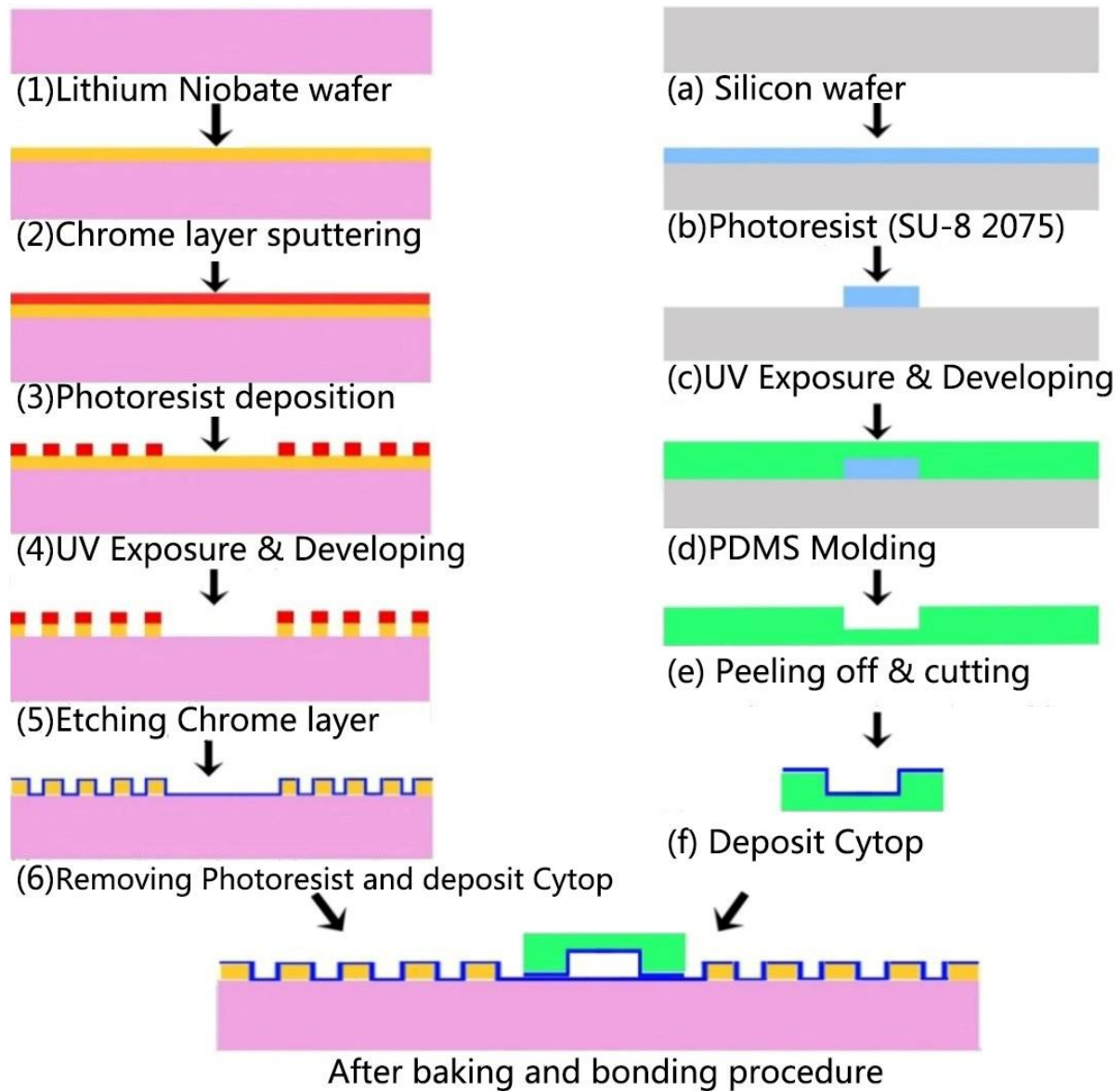


**Figure 4.4.** Fabrication process flow for SAW transducers, PDMS molding, Cytop layer spinning and bonding. All steps were completed in the cleanroom facilities of the University of South Florida

The microchannel was fabricated by PDMS micro molding technique. After the channel mold is formed, PDMS (Sylgard™ 184 kit Dow Corning, Midland, MI, USA) is poured into the SU-8 mold. Bonding of the IDT substrate and microchannel as well as the Cytop layer deposition was conducted after the fabrication of IDTs and microchannel separately. The PDMS channel was treated with oxygen plasma first; then both the IDT substrate and the PDMS channel were coated

with Cytop® 809M (ASAHI GLASS Co. Ltd, Japan) via spin coating with the average thickness of 1.8  $\mu\text{m}$  on the substrate. After separately pre-baking in an oven at 100  $^{\circ}\text{C}$ , a gauge needle was used to create the inlets and outlets. The Cytop layer was annealed at 160  $^{\circ}\text{C}$  for an hour as a final step<sup>71</sup>. Finally, the PDMS and the substrate were bonded and uniform pressure was applied. The fabricated IDTs and channel feature on the substrate are illustrated in Figure 4.5.

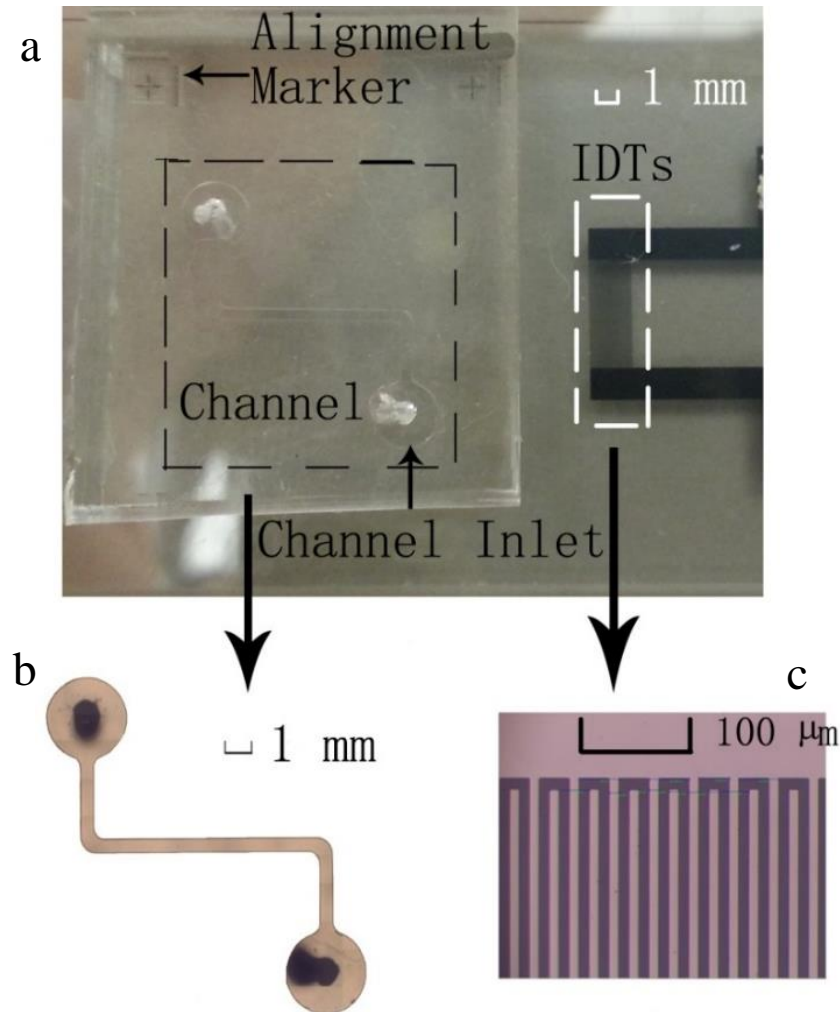


**Figure 4.5.** (a) Aligned IDTs and microchannel on the substrate; (b) close-up of the microchannel design investigated in this study; (c) details of the chrome IDTs

#### 4.5. Experimental Setup

An inverted microscope (IX-51, Olympus) with a CCD camera was used to visualize and record the experimental data collected (Figure 4.6). De-ionized water was injected into the channel from the inlet by an external syringe pump (KDS200, KD Scientific, Holliston, MA, USA). RF power amplifier (325LA, ENI) was used to amplify an AC signal generated by a function generator (AFG3022B, Tektronix). Displacement inside the microchannel was recorded by a CCD camera at 21 fps with a resolution of 1376 x 1038.

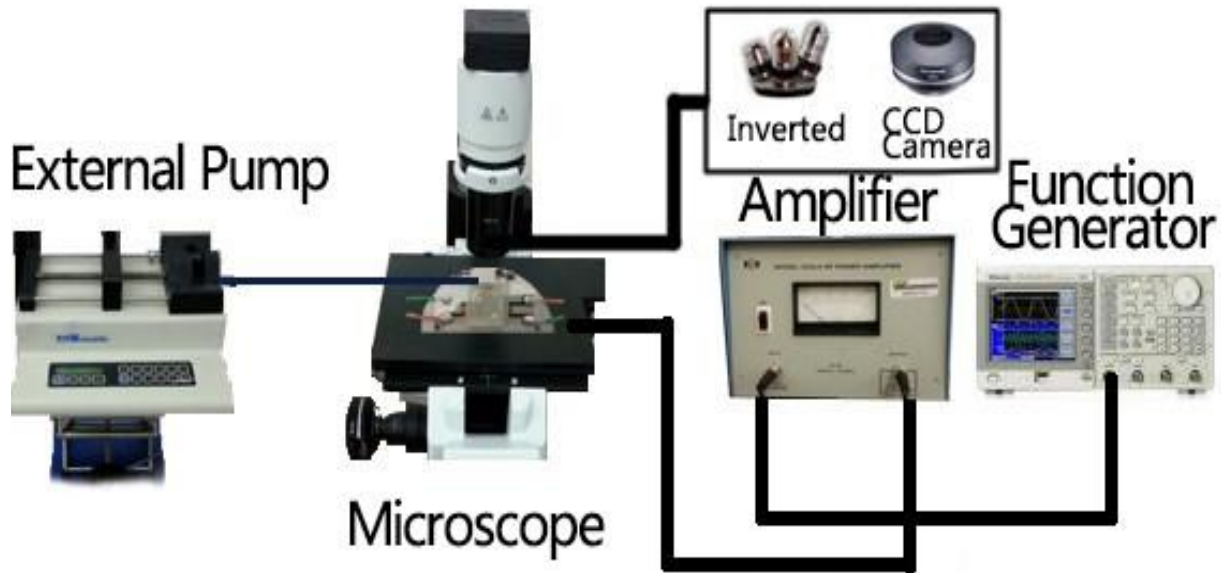


**Figure 4.6.** Experimental setup: An external pump was connected to the channel inlet to pump the liquid into the channel. Function generator generated a continuous sine wave to the amplifier, which is connected to the IDTs. An inverted microscope with a CCD camera was used to visualize and record the liquid pumping

As the input power is related to the amplitude of the SAW that determines the pumping velocity<sup>72</sup>, a wide range of applied input power values (ranging from 0 to 7.5 watts) was investigated to obtain the velocity dependence on input power. Also, in order to investigate the effect of liquid volume on the pumping velocity, two different representative volumes (0.22  $\mu\text{l}$  and

0.11  $\mu\text{l}$ ) were used. Additionally, channel widths of 250  $\mu\text{m}$  and 500  $\mu\text{m}$  were used to investigate the effect of channel width on pumping velocity.

Before delving into a detailed parametric study, we investigated the effect of the most common microfluidic channel material choice, PDMS, on the pumping. The contact angle of water on PDMS, which is hydrophobic, is around  $110^\circ$  for static drops<sup>73</sup>. However, fluid tends to stick to the PDMS surface due to the high contact angle hysteresis. The conventional syringe pump method was used to show the large adhesion force between the fluid and the PDMS surface after plasma bonding. First, a droplet ( $\sim 2 \mu\text{L}$ ) of de-ionized (DI) water was placed onto the substrate, then a needle was inserted into the droplet. A programmable syringe pump was connected to the other end of the needle and fluid was added to the droplet at a flow rate of 5  $\mu\text{L}/\text{min}$ . After 3 minutes, the pumping direction was reversed and fluid was withdrawn from the droplet. The shape of the droplet was captured using a digital camera during the infusion/withdrawing of the fluid, and the image was processed using ImageJ software. The contact angles of the droplet during the infusion and withdrawing phases are defined as the advancing angle and the receding angle, respectively. Figure 4.7 shows a large difference between the advancing and receding contact angles, which was also observed in prior studies<sup>74</sup>. The difference between the two angles is commonly known as contact angle hysteresis, which can cause a strong adhesion force that will prevent the motion of the fluid or droplet. To prevent this, a 1  $\mu\text{m}$  layer of Cytop coating was introduced to both the PDMS channel and the lithium niobate substrate. The static contact angle was significantly increased by the Cytop layer, as shown in Figures 4.7E and 4.7F, and contact angle hysteresis decreased from  $35^\circ$  to  $10^\circ$ . The only drawback of the existence of hydrophobic layer in the design was that the insertion loss of the IDTs increased by around 2 dB.

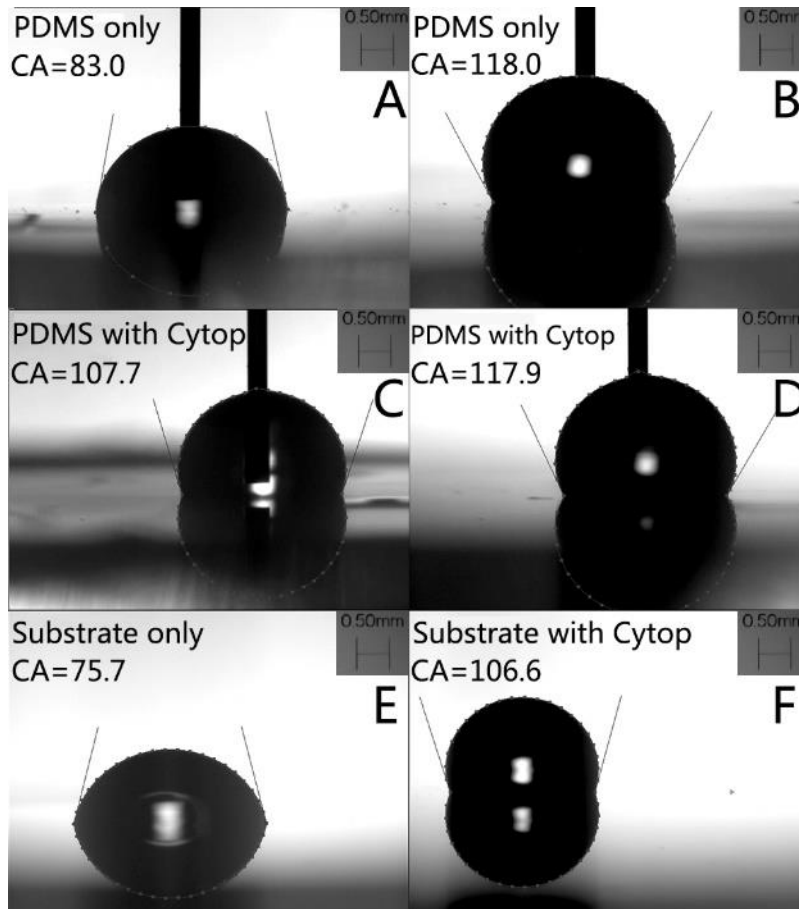


**Figure 4.7.** (A) Receding contact angle of the drop on the PDMS surface without Cytop layer; (B) advancing contact angle of the drop on the PDMS surface without Cytop layer; (C) receding contact angle of the drop on the PDMS surface with Cytop layer; (D) advancing contact angle of the drop on the PDMS surface with Cytop layer; (E) static contact angle of the drop on the lithium niobate substrate surface without Cytop layer; (F) static contact angle of the drop on the substrate with Cytop layer

#### 4.6. Results and Discussion

The liquid pumping was accomplished in this study with IDTs placed 5 to 8 mm away from the microchannel sidewalls. Initial experiments were conducted with both inlet and outlet open (Figure 4.8). Figure 4.9 illustrates the pumping experiment in the 250  $\mu\text{m}$  sealed channel without Cytop layer in the device design over 75 seconds. The power applied for this case was 6.5 watts (W), and liquid volume was 0.11  $\mu\text{l}$ . After the SAWs were excited with continuous sine waves, the liquid initially started to eject droplets at the low power condition (commonly referred as

atomization), as illustrated in Figure 4.9. As the input power was increased, the ejected droplet diameter started increasing<sup>75</sup>. At around 3 watts of input power in addition to atomization, the liquid started to move, and at 6 watts of input power, the atomization stopped while the liquid was being pumped.

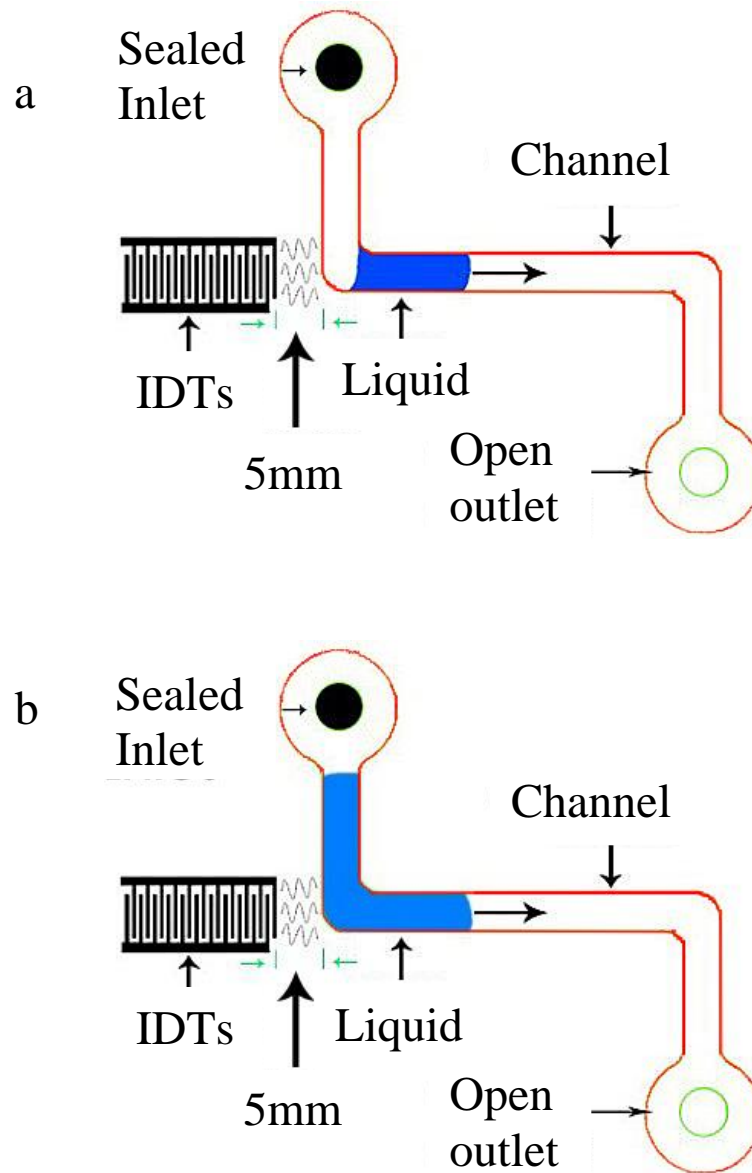


**Figure 4.8.** An illustration of different volumes of liquid pumping in the channel with sealed inlet and open outlet. The liquid volumes in Figure 4.8a and Figure 4.8b are  $0.11 \mu\text{l}$  and  $0.22 \mu\text{l}$ , respectively



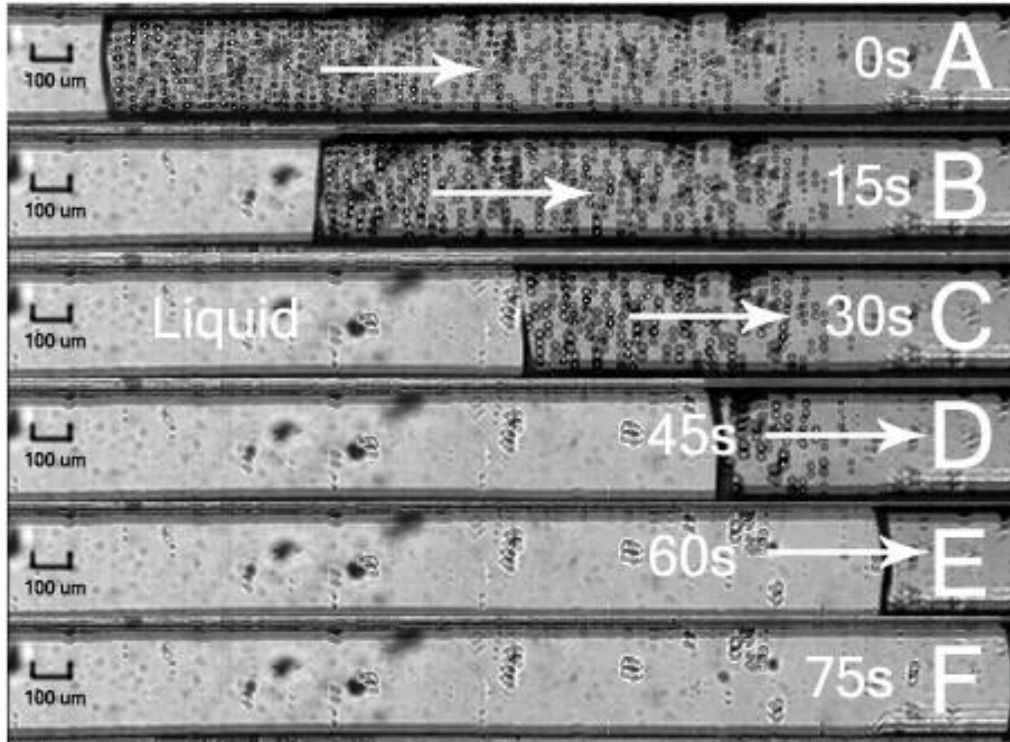


**Figure 4.9.** The pumping experiment in the 250  $\mu\text{m}$  channel without Cytop over 75 seconds. The power is 6.5 watts and liquid volume is 0.11  $\mu\text{l}$ . Due to the limitation of the field of view of the microscope, only part of the channel is shown

Additional sets of experiments were conducted by sealing the inlet of the microchannel with an off-the-shelf masking tape as illustrated in Figure 4.8. The applied input power ranged from 2 to 6.5 watts, and two types of surface coating were used (lithium niobate substrate without any coating and lithium niobate substrate and channel walls coated with Cytop). Increasing the input power caused increased acoustic wave amplitude. This led to higher acoustic body force as well as evaporation rate. As a result, the pumping force was composed of both acoustic body force and an expansion force. Increasing the input power resulted in higher heat generation, further increasing the total pumping force. Hence, the applied input power was found to be proportional to the pumping velocity. Figure 4.10 illustrates the pumping velocity as a function of applied input power with two different liquid volumes in a 500  $\mu\text{m}$  microchannel with the Cytop layer in the design. Increasing the input applied power resulted in increasing the pumping velocity for both

liquid volume cases investigated. One can observe from individual experimental data points that for applied input power range from 2 to 3 watts, the pumping velocities were not a strong function of the volume of the liquid being pumped. Note that this power range corresponds to pumping of the liquid sample with atomization present. However, the larger liquid volume case (0.22  $\mu\text{l}$ ) resulted in larger pumping velocity as compared to the lower liquid volume case (0.11  $\mu\text{l}$ ) once the power was further increased. Higher pumping velocity was obtained with the higher liquid volume case for the same power input because the liquid in the higher volume case was exposed to a larger body force in the direction of wave propagation. As can be observed from Figure 4.8, the larger volume case also had less inlet space available for expansion as the liquid was pushed in the desired direction.

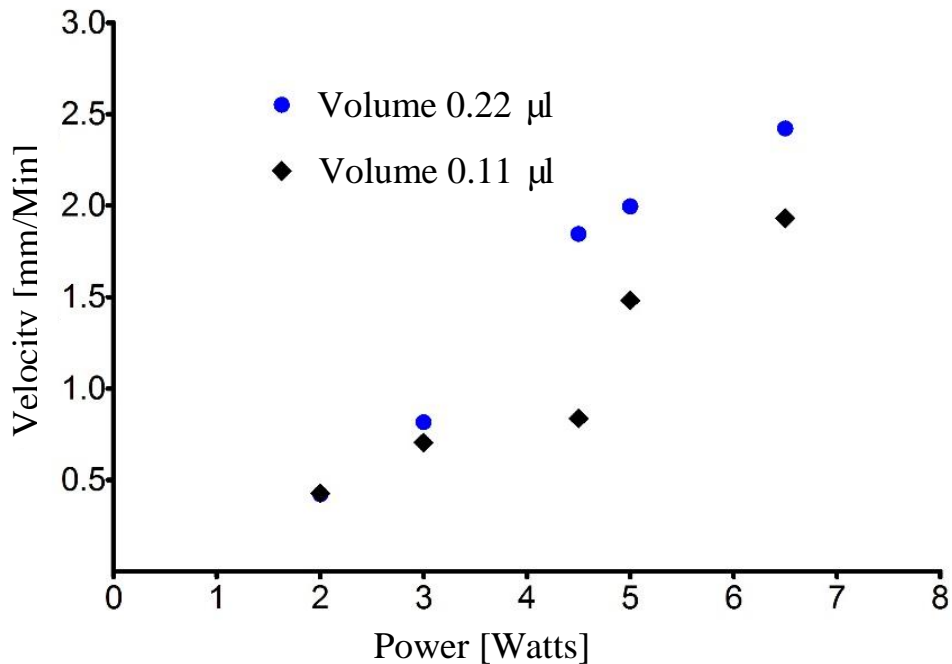


**Figure 4.10.** Experimental pumping velocity as a function of applied input power with two different liquid volumes (0.22  $\mu\text{l}$  and 0.11  $\mu\text{l}$ ) in a 500  $\mu\text{m}$  microchannel with the Cytosol layer coating in the design



In addition, extensive experiments were conducted to investigate the effect of the coating of the microchannel surfaces on pumping velocity. Figure 4.11 illustrates the experimentally obtained pumping velocity as a function of applied input power for a 500  $\mu\text{m}$  microchannel with/without the Cytop layer in the design for two different liquid volumes: 0.22  $\mu\text{l}$  (Figure 4.11a) and 0.11  $\mu\text{l}$  (Figure 4.11b). Additionally, Figure 4.12 shows the experimentally obtained pumping velocity as a function of applied input power for a thinner (250  $\mu\text{m}$ ) microchannel with/without the Cytop layer in the design for two different liquid volumes: 0.11  $\mu\text{l}$  (Figure 12a) and 0.054  $\mu\text{l}$  (Figure 4.12b). Increasing the input applied power resulted in increasing the pumping velocity for all microchannel width and liquid volume cases investigated. One can observe from both Figures 4.11 and 4.12 that for the same liquid volume and input power applied cases, hydrophobic surface coating (Cytop) increases the pumping velocity for both microchannel widths and liquid volumes investigated. When one compares Figure 4.11b to Figure 4.12a, the effect of hydrophobic surface coating on the pumping velocity for the same liquid volume for different microchannel widths can be observed. In the low input power cases (2-3 W), there was no significant effect of hydrophobic coating on the pumping velocity due to increased (2 dB) insertion loss with the Cytop layer in the design. However, in the larger power consumption cases (>3 W), the inclusion of hydrophobic coating in the channel design had an increased effect on the pumping velocity for the wider microchannel (500  $\mu\text{m}$ ) as compared to the thinner channel width (250  $\mu\text{m}$ ). The reason for obtaining higher pumping velocity for a thinner microchannel as opposed to a wider channel with the same liquid volume is that the length of the fluid within the microchannel is longer for the thinner microchannel, resulting in increased resultant force in the longitudinal direction (along the length of the microchannel) and thus higher pumping velocity.

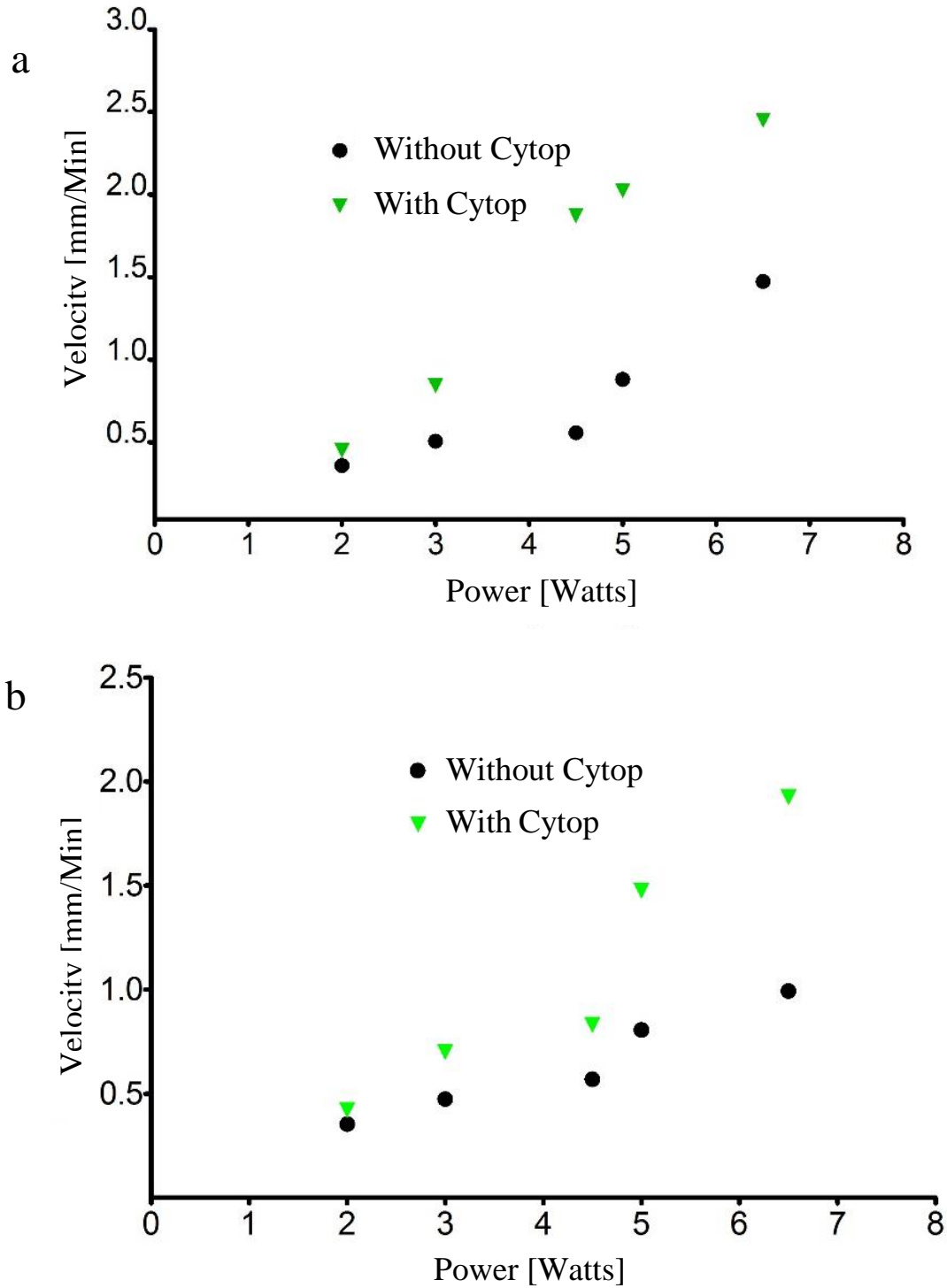


**Figure 4.11.** Experimental pumping velocity as a function of applied input power in a 500 μm microchannel with/without the Cytop layer in the design for two different liquid volumes: 0.22 μl (Figure 4.11a) and 0.11 μl (Figure 4.11b)

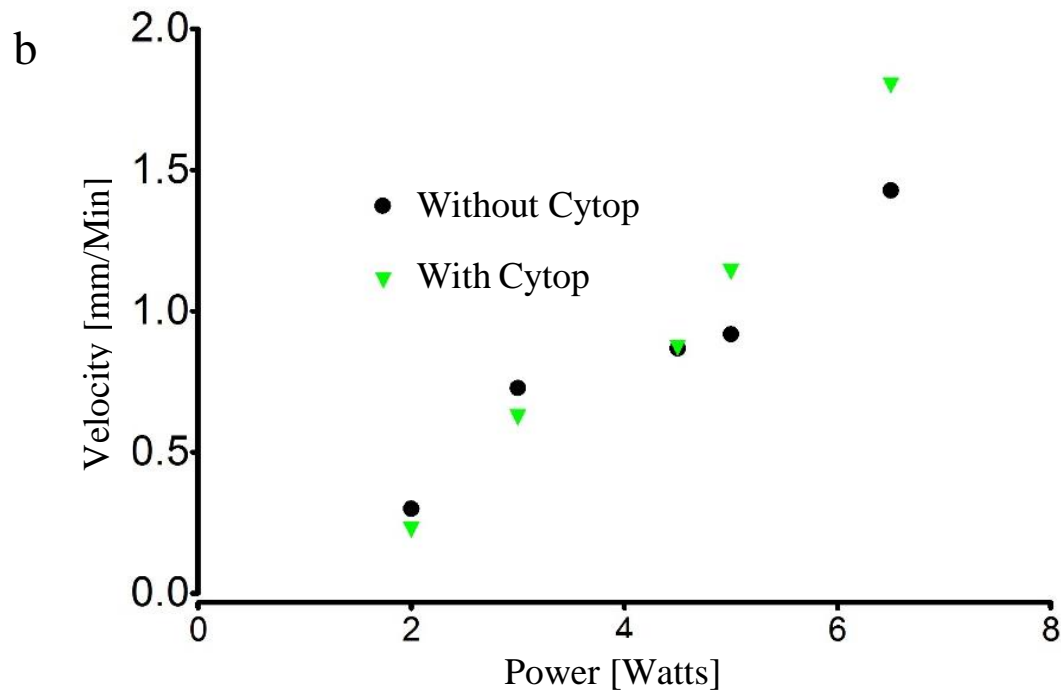
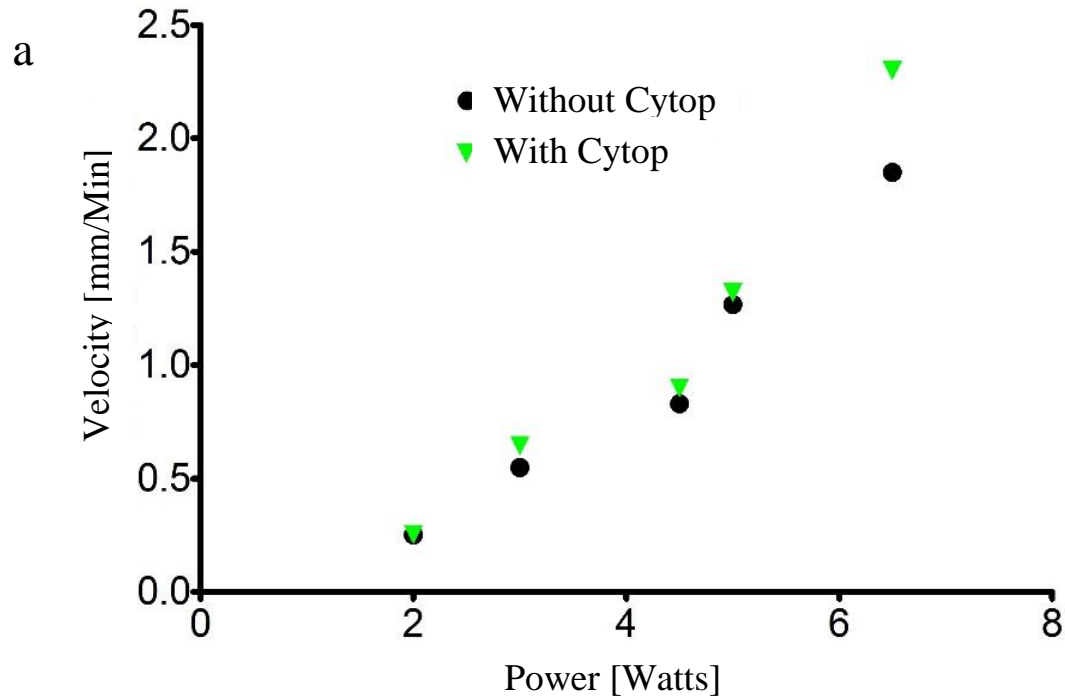


**Figure 4.12.** Experimental pumping velocity as a function of applied input power in a 250 µm microchannel with/without the Cytop layer in the design for two different liquid volumes: 0.11 µl (Figure 4.12a) and 0.054 µl (Figure 4.12b)

#### 4.7. Conclusions

In this study, we conducted a thorough investigation of liquid pumping within a microfluidic channel by using the phenomenon of surface acoustic wave force and heat expansion force. We illustrated successful pumping within a microchannel with surface acoustic wave devices located outside the microchannel patterned on a piezoelectric substrate. Significant advantages of this device are protection of the liquid within the channel, easy and low-cost fabrication, no contact between the pumping device and the liquid, homogenous steady laminar flow, and small-scale, precise liquid control and delivery. Due to the large friction force of the microchannel walls surrounding the liquid, a hydrophobic surface coating (Cytop) was investigated in detail, and increased pumping velocity was demonstrated. Our studies indicate that the pumping velocity for a constant liquid volume with the same applied input power can be increased by over 130% (2.31 mm/min vs 0.99 mm/min) by employing a hydrophobic surface coating (Cytop) in a thinner microchannel (250  $\mu\text{m}$  vs 500  $\mu\text{m}$ ) design. This microchannel pump can be used in circulation, dosing, metering and drug delivery applications in which small-scale, precise liquid control and delivery are important.

## CHAPTER 5. LIQUID PROPERTY SENSING WITH A SURFACE ACOUSTIC WAVE BASED SENSOR

### 5.1. Introduction

Even though surface acoustic waves (SAW) have been used in the electronics industry for many decades, there is a need to improve their sensitivity and stability in order for SAW technology to be competitive among its alternatives. In this part of the dissertation, we focused on improving the sensor sensitivity and demonstrating liquid property sensing in a microfluidic channel. In order to achieve this goal; we first optimized the interdigital transducer (IDT) design by using the commercially available simulation package COMSOL. During the optimization process, a two-port SAW resonator was designed with low insertion loss and high Q-value on ST-cut quartz substrate using a simple and efficient IDT electrode structure. The devices demonstrate enhanced stability for liquid sensor applications integrated with PDMS microfluidic system environments. High sensitivity, low insertion loss, large Q-value and good stability were obtained by optimizing the metallization ratio, substrate thickness ratio, finger thickness ratio and acoustic aperture. The details of the optimization study were discussed in detail in the Chapter 3 of this dissertation.

The majority of liquid sensors need grating or films deposited on the sensor area in order to protect the interdigital transducers and to improve the sensitivity<sup>26,27</sup>. Only a few of the devices developed have employed a microfluidic channel to monitor the properties of the liquid in real time<sup>24,28</sup>. Without a fluidic system in the design, the liquid to be tested is directly in contact with

the environment open atmosphere, causing fast evaporation. Hence these sensors can only be used for static testing of a few drops, not for real time monitoring of continuous flow. The major advantages of implementing a microfluidic channel in a lab-on-a-chip device are low liquid sample consumption, fast analysis time, flow rate detection and protection of media from environmental effects. Another limitation of many sensors is that the design uses a delay line configuration, which has low quality factor of stability and reproducibility. Therefore, a delay line design may easily result in varying oscillation frequency, which reduces stability and results in poor repeatability. Resonator design can improve reproducibility and stability compared to delay line sensors, especially for long-term operation<sup>14,76</sup>.

In this dissertation, we focus on weight concentration differentiation of microfluidic particles based on a polydimethylsiloxane (PDMS) channel and a surface acoustic wave resonator. PDMS has been widely used as a biocompatible material for biomedical devices. However, PDMS is a non-reflective material and is generally always used as an absorber in sensor applications<sup>77,78</sup>. A stable signal generated by a resonator shows that the device is more competitive than a delay line sensor. The results confirm that our device exerts an ultra-stable status to detect liquid properties by monitoring continuous fluids, which also shows its potential for use in biomedical and industrial areas as a fluidic sensor.

## **5.2. Working Principle**

The SH-SAWs frequency shift results in propagation loss when a wave travels through the flow inside the PDMS channel. When the liquid is loaded on the path where the surface acoustic wave propagates, the phase velocity and attenuation of the wave are related to the characteristics of the liquid, including mechanical properties such as viscosity and density, and electrical characteristics such as permittivity and conductivity as shown in Equation 5.1 and Equation 5.2.

$\eta_1$  and  $\eta_{REF}$  are the viscosity of the test liquid and reference liquid.  $\rho_1$  and  $\rho_{REF1}$  are the density of the test liquid and reference liquid<sup>79</sup>.

$$\frac{\Delta V}{V} = -C(\sqrt{\eta_1 \rho_1} - \sqrt{\eta_{REF} \rho_{REF1}}) \quad \text{Equation 5.1}$$

$$\frac{\Delta \alpha}{k} = C(\sqrt{\eta_1 \rho_1} + \sqrt{\eta_{REF} \rho_{REF1}}) \quad \text{Equation 5.2}$$

### 5.3. Device Design and Fabrication

A delay line path and two-port resonator were designed as illustrated in Figure 5.1. The parameters of the delay line and resonator designs are shown in Table 5.1. 50 stripes of reflectors and 30 fingers of interdigital transducers were used in the resonator design. A large number of reflectors increase the quality factor  $Q$  and reduce the insertion loss. The SAW wavelength, IDT finger pitch, finger width and aperture were designed as 300  $\mu\text{m}$ , 300  $\mu\text{m}$ , 75  $\mu\text{m}$  and 9 mm, respectively. The resonator parameter  $d_m$  in Figure 5.1 is the distance between the IDT ports and is calculated by using Equation 5.3. The reflection grating,  $d_g$  (Equation 5.4), is the distance between the reflector and the nearest IDT finger, which enables the wave that is excited by the first finger in the pair travel back towards the first finger with the same phase angle. For delay line design, the  $d_m$  is equal to  $n \times \lambda$ .

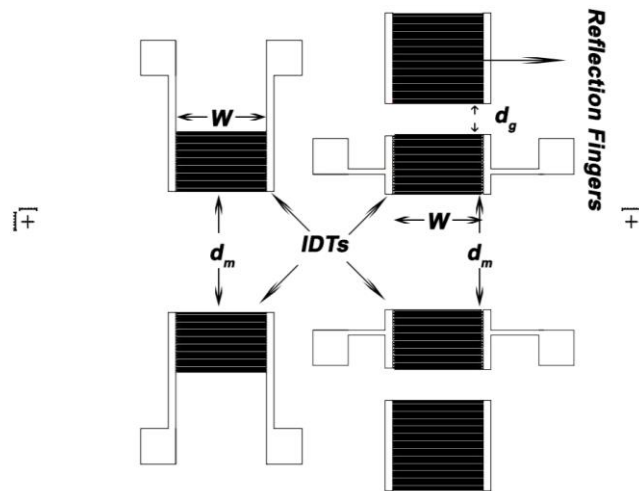


**Figure 5.1.** Delay line and two-port resonator design with channel alignment mark

$$d_m = \lambda/4 + n \lambda/2, (n=0,1,2,3\dots) \quad \text{Equation 5.3}$$

$$d_g = \lambda/8 + n \lambda/2, (n=0,1,2,3\dots) \quad \text{Equation 5.4}$$

**Table 5.1.** Parameter of delay line and resonator design

Parameters	Delay line path	Two-port resonator
Wavelength ( $\lambda$ )	300 $\mu\text{m}$	300 $\mu\text{m}$
Pairs of fingers	30	30
Pairs of reflecting fingers	0	50
Finger width	75 $\mu\text{m}$	75 $\mu\text{m}$
Wavelength of reflecting fingers	0	300 $\mu\text{m}$
Aperture ( $w$ )	9.8 mm	9.8 mm
Channel width	1 mm	1 mm
Channel width (particle properties measurement)	2 mm	2 mm
Channel height	100 $\mu\text{m}$	100 $\mu\text{m}$
Finger height	100 nm	100 nm
Phase velocity (SH-WAW)	4160 m/s	4160 m/s
Phase velocity (leaky SAW)	4112 m/s	4112 m/s
Distance $d_g$	0	3.0375 mm
Distance $d_m$	12 mm	11.475 mm
Design frequency	13.9 MHz	13.9 MHz



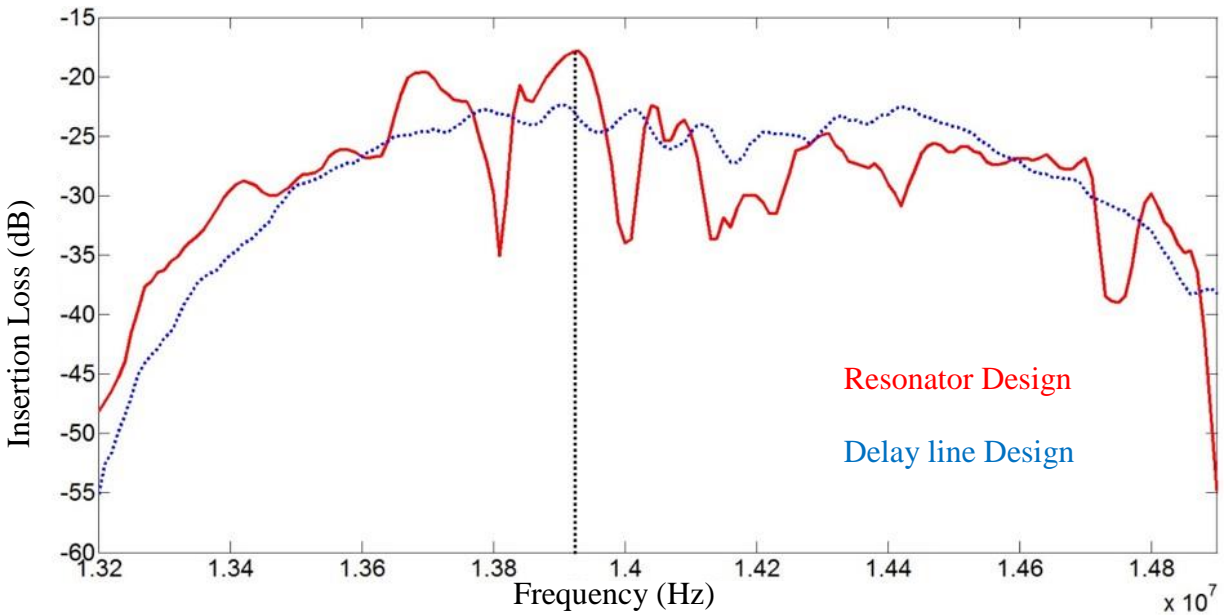


**Figure 5.2.** Frequency spectrum for resonator design and delay line design by network analyzer

By using the design parameters listed in the Table 5.1 and the leaky SAW of 36 °YX LiTaO<sub>3</sub> speed of 4112 m/s, the resonator leaky wave frequency can be obtained at around 13.7 MHz. Given that, the surface transverse wave speed is 4160 m/s, one can obtain the resonator transverse wave frequency to be around 13.87 MHz. After both the delay line and resonator designs are fabricated by the transducer fabrication process discussed in Chapter 4 (Figure 4.4), the resonance frequency of each design was measured by a network analyzer (Agilent 5061A, Agilent Technologies Inc.) as illustrated in Figure 5.2. Figure 5.2 shows the peak frequencies for the delay line design around the design frequency to be close to one another. It is difficult to pick the resonance frequency. The resonator design decreases the overall insertion loss (−17.5 dB for resonator design and −22.2 dB for delay line design) and also increases the insertion loss difference between the neighboring resonance frequency peaks (0.6 dB difference for delay line design and 2.1 dB difference for resonator design). Figure 5.2 also illustrates that the resonance frequency for the resonator design is 13.9 MHz, which is close to the design transverse wave frequency. The closest resonance frequency peak at left is 13.71 MHz and also fits the leaky wave frequency. Experiments with

delay line design for 36 °YX LiTaO<sub>3</sub> at low frequency range resulted in the resonance frequency recorded by frequency counter jumping between neighboring peaks, which is highly undesirable. Therefore, resonator design was chosen in this study to quantify the properties of liquid in microfluidic channel.

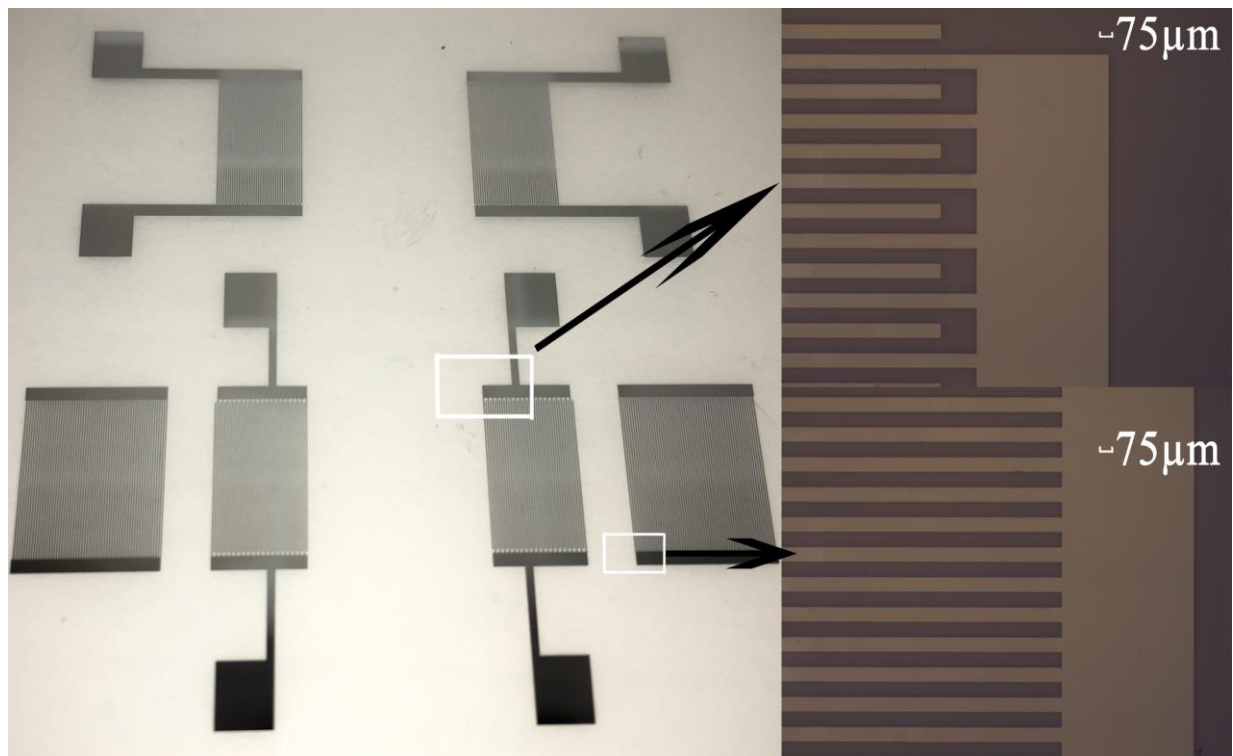


**Figure 5.3.** Aligned resonator and microchannel on the substrate

The microchannel was fabricated by a PDMS micro molding technique. The SU-8 channel was fabricated by pouring PDMS (Sylgard™ 184 kit, Dow Corning, Midland, MI, USA) onto a channel mold with 100  $\mu\text{m}$  height, and the channel length at the sensing cross section of 10 mm. The volume of liquid in sensing area is 2  $\mu\text{l}$ , and the total volume of the media inside the channel is 9  $\mu\text{l}$ . Figure 5.3 illustrates a completed device where both resonator and microchannel are integrated on a single substrate.

## 5.4. Experimental Setup

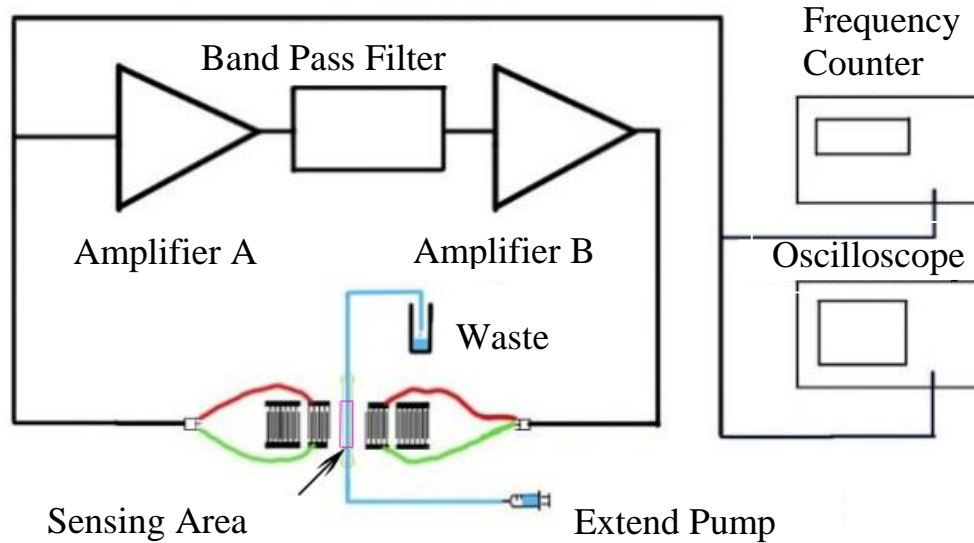


**Figure 5.4.** Conceptual view of the oscillatory circuit system for liquid properties detection

A custom-designed oscillatory circuit system was used for quantifying the glycerol and particle concentrations, as shown by Figure 5.4 in the conceptual view. An oscillatory circuit configuration was selected due to higher sensitivity and stability as demonstrated in prior publications<sup>16,80</sup>. The resonator device was used as a filter and feedback element of the RF amplifier A and B (Figure 5.4). The frequency shift related to the surface acoustic wave phase velocity changes on the path (through the microfluidic channel from transmit to receiver finger) which resulted from the density and viscosity changes of the liquid. The setup used two variable gain RF amplifiers (Olympus 5073PR and Olympus 5072PR, Olympus NDT Inc., Waltham, MA, USA), a digital frequency counter (Agilent 53220A, Agilent Technologies Inc., Santa Clara, CA, USA) and an oscilloscope (Tektronix TDS2001C, Tektronix Inc., Beaverton, OR, USA). Two oscillation conditions had to be created before the test. The first one was to adjust the two amplifiers' gains to compensate the losses in the loop by obtaining an input gain to guarantee that the total gain in the loop was at least 0 dB. The second oscillation condition was to make the total

loop phase equal to 0<sup>al6</sup>. This method was intended to reduce undesirable frequency peaks and phase noise in the loop. After the system was set up, a very stable signal was generated with a frequency between 13,889,920 Hz and 13,890,000 Hz with a shift range of only 80 Hz. Figure 5.5 illustrates the long-term stability of the device at 180 minutes. This device is very stable for long time operation and similar to other published study results<sup>81</sup> (0.7 ppm in this dissertation and 0.4 in reference).

After the system switched on, the frequency would return to this range (from 13,889,920 Hz to 13,890,000 Hz) after about 30 minutes. At this range, this system can reduce the background noise frequency in a stable environmental to an average of 45 mHz/s. This range of stability was sufficient to obtain the different frequency shifts with particles or glycerol with different densities and viscosities passing through the integrated microfluidic channel. An external syringe pump (KDS200, KD Scientific, Holliston, MA, USA) was used to pump the particle and glycerol mixture into the channel. Then the data sheets were recorded by a digital frequency counter with a sampling rate of 10 Hz as the liquid passed through the sensing area.

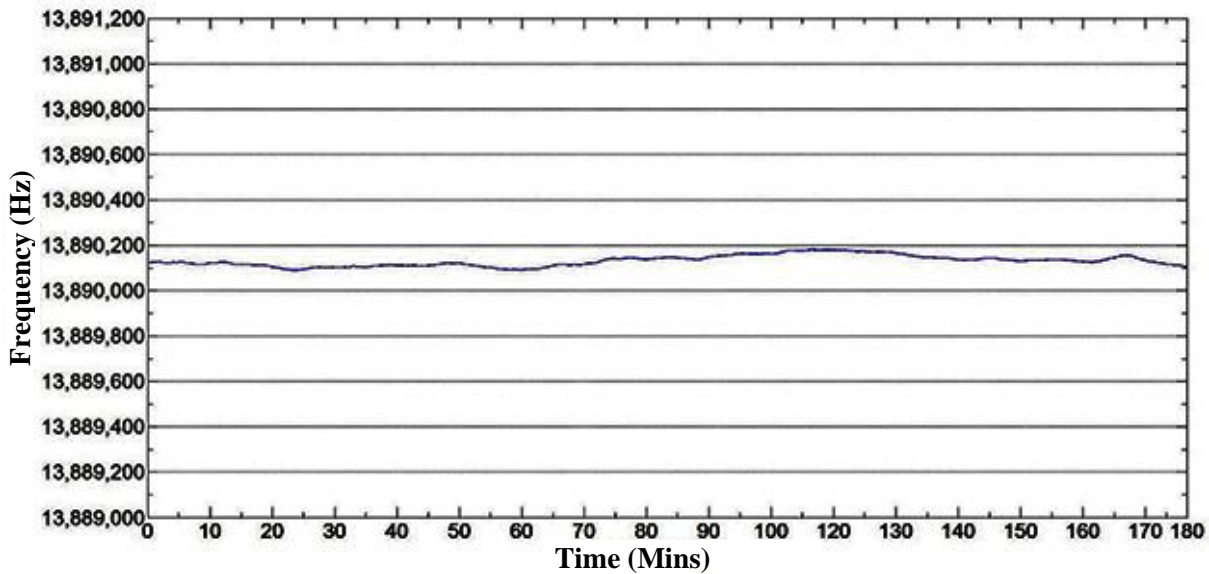


**Figure 5.5.** Long-term experiment to test stability

## 5.5. Results and Discussion

### 5.5.1. Experiment for Flow Rate Measurement

When the liquid was pumped to the sensing area with a fixed flow rate, a frequency shift was observed by the frequency counter and recorded at the remote computer. The flow rate was calculated by multiplying the velocity by the area of the sensing cross section. The velocity was obtained from the aperture length ( $w$ ) divided by the time ( $t_s$ ) of liquid passing through. Then the time  $t_s$  could be calculated simultaneously from the number of dots ( $N$ ) in the data sheet recorded by the frequency counter which is  $t_s = N/10$ .

$$Q = R \frac{SL}{N} \quad \text{Equation 5.5}$$

The flow rate of the liquid can be calculated from the number of frequency shift data as demonstrated in Equation 5.5.  $Q$  is the flow rate of the liquid, and  $N$  is the total number of dots when the flow passes the sensing section. On the other hand,  $t_s$  depends on the sampling rate ( $R$ ) and the aperture length ( $L$ ).  $S$  represents the cross section area of the microchannel. The total frequency shift data dots  $N$  were recorded and sent to the remote computer and then processed by a custom-written program in MATLAB®.

Experimental flow rates ranging from 3  $\mu\text{l}/\text{min}$  to 20  $\mu\text{l}/\text{min}$  were investigated by the fabricated integrated device. Figure 5.6 shows that the theoretical calculation results from Equation 5.5 compared to the experiments. The results of the experiments matched the results of the calculations, and the error bars were much smaller than in the higher flow rate cases. At the low flow rate, due to the longer travel time through the sensing area, a large amount of noise reflection and background noise data was collected increasing the standard deviation. These would increase the error rate after these false dots were processed. The maximum flow rate of this resonator sensor was related to the aperture of the IDT fingers and the limitation of the sampling rate of the

frequency counter. The detection system was qualified to detect the maximum flow rate of 1080  $\mu\text{l}/\text{min}$ . Increasing the length of the aperture increased the limits of the maximum flow rate. The channel's width and height would had no effect on the sensitivity of the flow rate but could affect the limitation of the maximum flow rate.

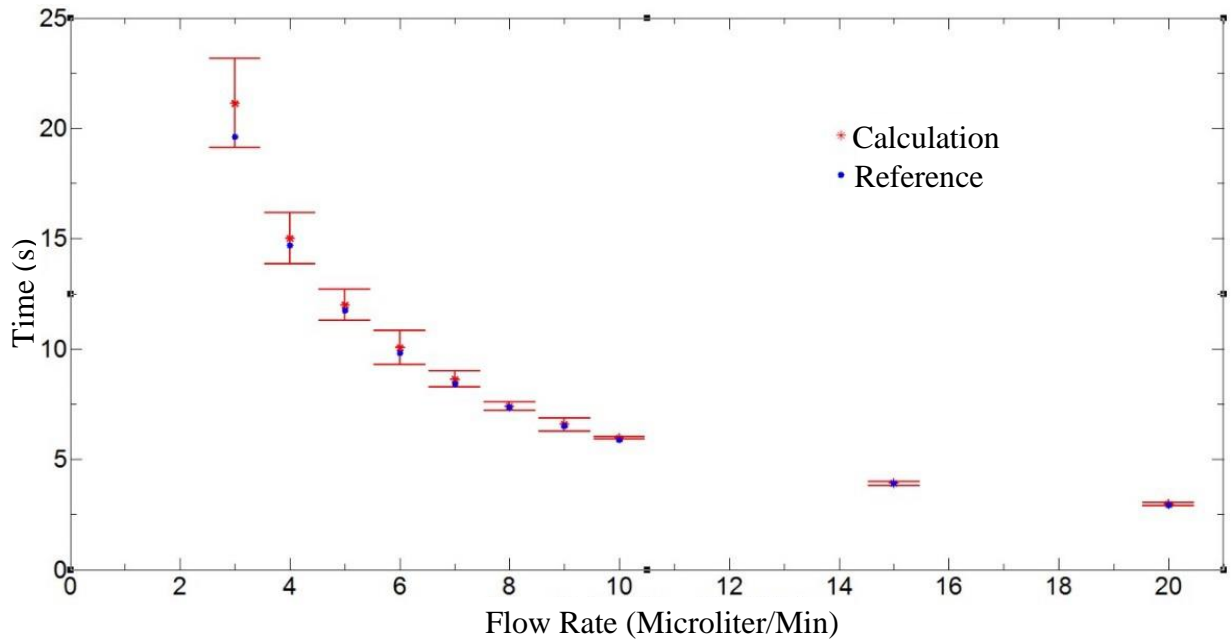


**Figure 5.6.** Results of calculation of the flow rate from the equation compared to the experimental results

### 5.5.2. Finite Element Simulations

A group of glycerol mixture solutions (Thermo Scientific, Waltham, MA, USA) were mixed up by weight concentration. Frequency shift would be measured to calculate the mechanical properties  $\sqrt{\rho\eta}$  by Equation 5.1 and Equation 5.2. Before the experiments, finite element simulations (FEM) were conducted as part of this study to verify the resonator design's qualification by using the commercial COMSOL Multiphysics software.

A 3D COMSOL model of a two-port resonator was built to characterize the wave propagation characteristics resulting from the mechanical property changes inside the channel. For the 3D model simulation, a unit cell [300  $\mu\text{m}$  (L)  $\times$  200  $\mu\text{m}$  (W)  $\times$  500  $\mu\text{m}$  (H)] of the lithium tantalite

resonator was built (Figure 5.7) to obtain the resonance frequency of the device by using the eigenfrequency module created in COMSOL. A 3D-cell model would narrow down the frequency range to find the resonator frequency for a 3D realistic simulation as illustrated in Figure 5.8. In the simulation, the structure and electric potential boundaries ( $\Gamma_L$ ,  $\Gamma_R$ ,  $\Gamma_F$  and  $\Gamma_B$  as indicated in Figure 5.7) were set as periodic in nature to simulate multiple pairs of IDT fingers with a simplified geometry. Figure 5.7 shows the design of the interdigital transducer with one wave length and two fingers on the top with one of them connected to the ground. A tetrahedral mesh was applied on the model with a minimum element size of  $0.8 \mu\text{m}$  and complete mesh of 101,787 domain elements. As expected, the shear horizontal wave propagated in the  $x$  direction and the substrate polarized in the  $y$  direction as illustrated in Figure 5.7. The estimated frequency of the 3D-cell model was 13.87057 MHz, which was close to the device resonance frequency of 13.89014 MHz.

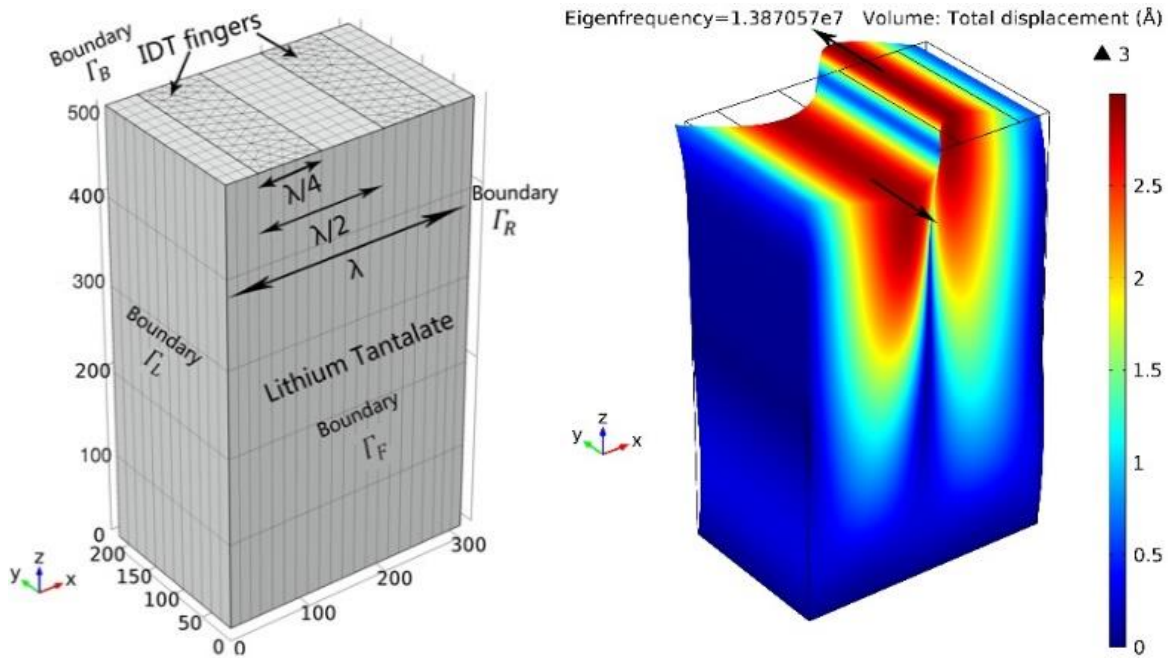


**Figure 5.7.** 3D-cell simulation of resonance frequency



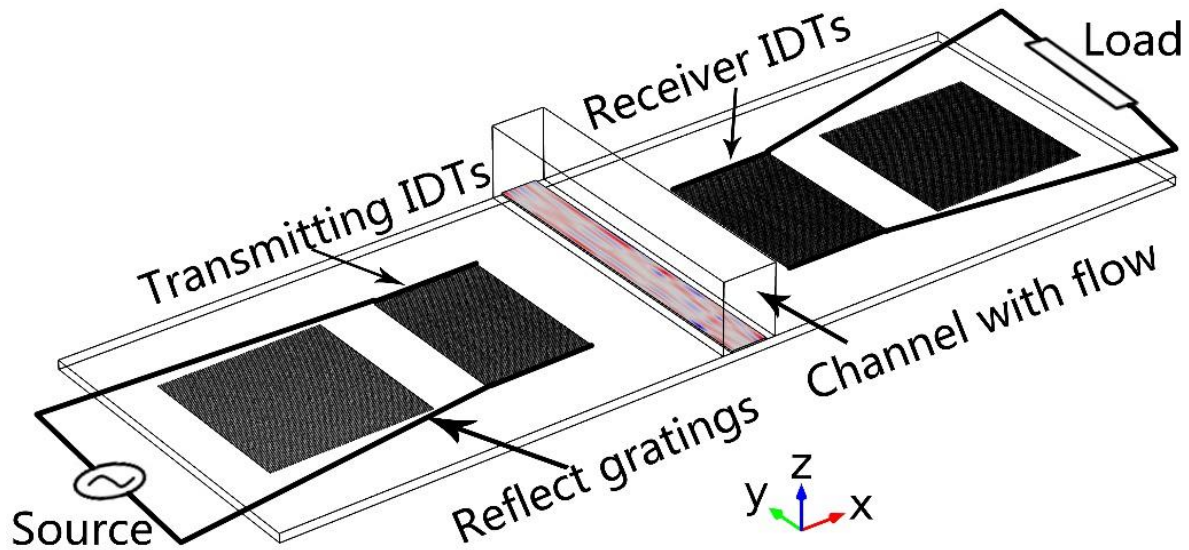


**Figure 5.8.** 3D simulation of insertion loss effected by the mechanical properties of the different weight concentrations of glycerol

After the 3D model was built, an acoustic-piezoelectric module in a realistic model was applied to conduct a frequency domain study as illustrated in Figure 5.8. The parameters of density and viscosity of the different weight concentrations of glycerol ranging from 0%-95% used in the 3D simulation as shown in the Table 5.2. For the purpose of simplifying the problem and reducing the computational cost, a static glycerol solution was applied in the microfluidic channel instead of a continuous flow. A fine mesh by use of tetrahedral elements was applied on the model with a complete mesh of 45,945 domain elements, 24,218 boundary elements and 1,421 edge elements. An acoustic module and acoustic boundary condition were applied to the system which included hard sound boundaries at left and right cross section, acoustic structure boundary on the glycerol body, and a fixed constraint on the bottom of the substrate. In Figure 5.8, the transmitting IDTs were applied with a 0.5 V potential voltage signal. An output signal was obtained at the receiver IDTs with the voltmeter probe. Since the designs of the input and output IDTs were symmetric, the insertion loss was quantified by the input and output signals<sup>82</sup> as shown in Equation 5.6.



$$IL = 20 \times \text{Log}_{10}|V_{out}/V_{in}| \quad \text{Equation 5.6}$$

**Table 5.2.** Density and viscosity of the different weight concentrations of glycerol<sup>83</sup>

Weight Concentration (%)	DENSITY (kg/m <sup>3</sup> )	Viscosity (cP)
0	0.99823	1.05
10	1.0221	1.31
20	1.0469	1.76
30	1.0727	2.5
40	1.0993	3.72
50	1.1263	6
60	1.1538	10.8
70	1.18125	22.5
80	1.2085	60.1
90	1.2351	219
95	1.24825	523

### 5.5.3. SH-SAW Measurements of Liquid Mechanical Properties

Different weight concentrations of glycerol, ranging from 0% to 95%, were separately injected into the microchannel by the external pump at a constant room temperature (23 °C) and fixed flow rate (2 µl/min). The initial experiment was conducted in the 1 mm width channel, which was not efficient for distinguishing the different weight concentrations. Then a 2 mm width channel with the same height of 100 µm was applied to the experiment. Therefore, it took 48 seconds for the flow to pass through the sensing area. After each experiment, the channel was flushed by the DI-water five times and then baked in the oven for 20 minutes. Real-time data was

recorded for 3 minutes and illustrated that frequency would shift down to a lower frequency due to the increase in density and viscosity. Figure 5.9 shows that frequency shifts were normalized to the DI-water control group, which made it easier to distinguish the difference in weight concentrations. Glycerol mixtures ranging from 0% to 60% weight concentration had been measured in a few papers as Newtonian fluids<sup>83</sup>. Those in the range 70%-95% were non-Newtonian fluids, and Figure 5.10 shows that density and viscosity multiplication of both Newtonian and non-Newtonian fluids in reference Table 5.2 matched the increasing trend of the experimental results (Figure 5.9). The simulation results as illustrated in Figure 5.11 also matched Newtonian fluid trends for insertion loss. This indicated that the COMSOL enabled reasonable predictions for different concentrations of the glycerol.

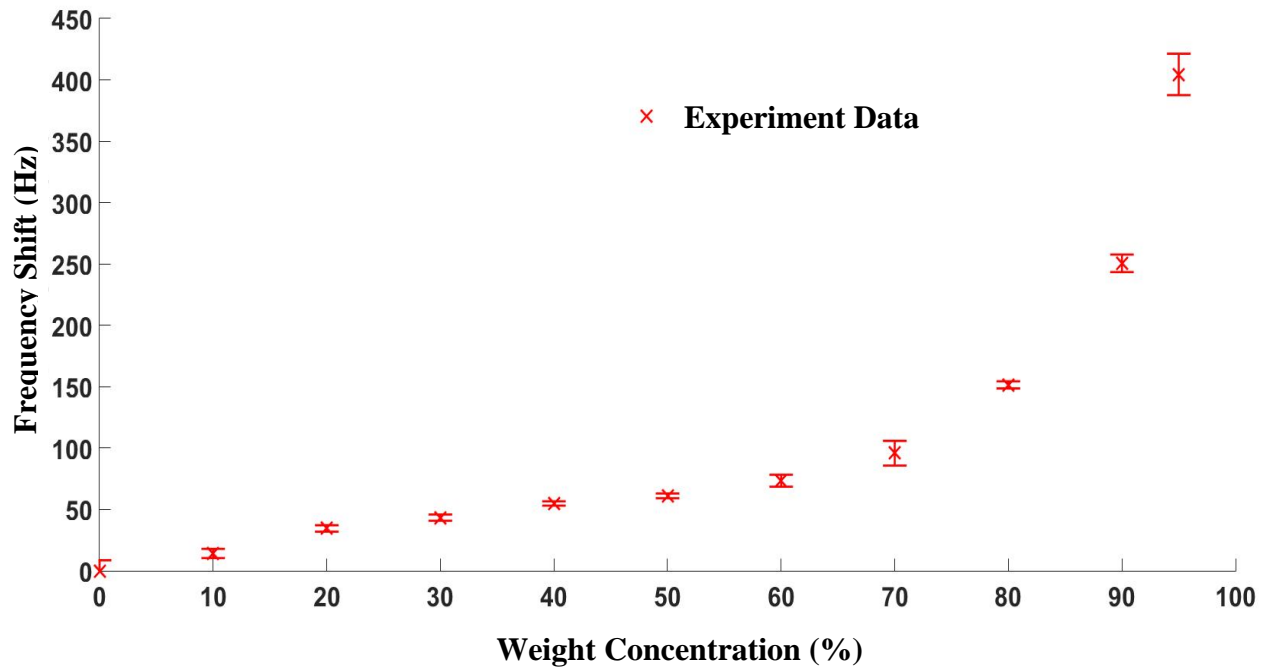


**Figure 5.9.** Relative frequency shift of different concentration of glycerol

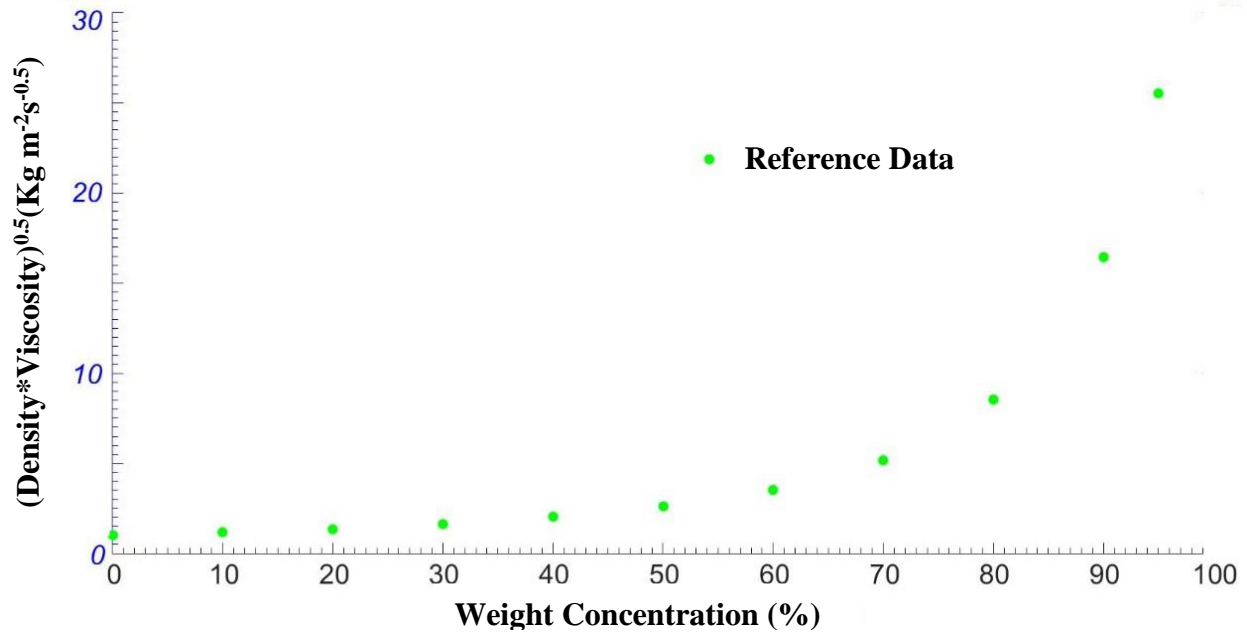


**Figure 5.10.** Different weight concentrations of glycerol with relation to multiplication of density and viscosity

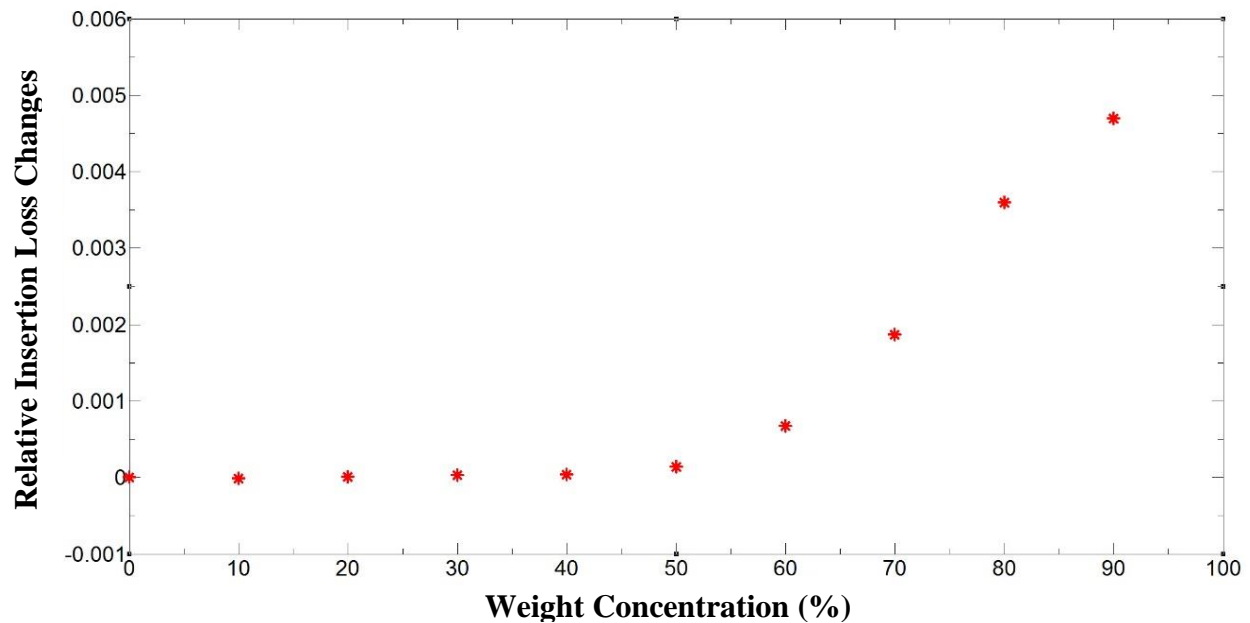


**Figure 5.11.** Simulation results of designed resonator's response on different weight concentrations of glycerol

After the weight concentrations of glycerol were detected by the designed system, particle weight concentration (Thermo Scientific, Waltham, MA, USA) experiments were conducted to

investigate the different weight concentrations of particles in fluids flowing at a constant flow rate (2  $\mu\text{l}/\text{min}$ ). A 2 mm width channel with the same height of 100  $\mu\text{m}$  was also used for the experiments. Solutions with same particles (8  $\mu\text{m}$  in size and 1.09  $\text{g}/\text{cm}^3$  in density) of different weight concentrations (0%, 1%, 2.5% and 5%) were used in experiments. Pure DI-water (density of 0.998  $\text{g}/\text{cm}^3$ ) was used as a control group. As the weight concentration changed slightly, the dielectric properties did change minimally, but did not affect the experimental results. Viscosity and density caused the resonator frequency changes, as shown in Figure 5.12, which was normalized to the reference DI-water. Due to the slight density and viscosity changes, the frequency shift of different weight concentration was small but sufficient enough to be detected.

Long-term and short-term stability enabled the detectable changes. A large error bar in the 5% concentration resulted from some particles accumulating at the inlet and reducing the weight concentration of flow in the detection section. Increasing the flow rate and enlarging channel width reduced the accumulation effect.

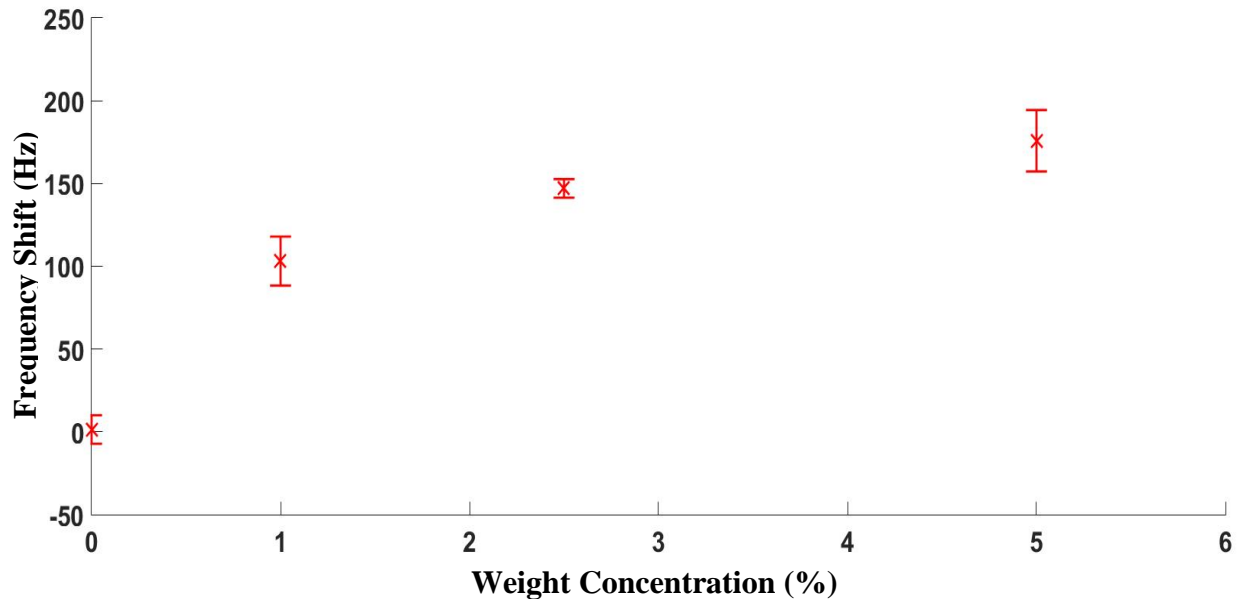


**Figure 5.12.** Relative frequency response to different weight concentrations of particles (8  $\mu\text{m}$  in diameter and 1.09  $\text{g}/\text{cm}^3$  in density)

## 5.6. Conclusions

In this study, a surface acoustic wave sensor integrated with microchannel was used for determination of the flow rate of liquid, weight concentration of glycerol and particle detection. SH-SAWs were generated by the optimized resonator to realize a very stable signal for fast analysis. Real-time monitoring of the flow rate and weight concentrations were remotely recorded and processed by the computer. This device was based on viscosity and density changes, which would reduce the speed of SH-SAWs phase velocity. COMSOL was first time used to simulate the SH-SAW sensor insertion response to liquid concentration. With the advantages of low liquid sample consumption, fast analysis and real-time flow monitoring made this device a viable low-cost choice for microfluidic system.

## CHAPTER 6. CELL QUANTIFICATION WITH A SURFACE ACOUSTIC WAVE MICROFLUIDIC SENSOR

### 6.1. Note to Reader

The manuscript and the results presented in this chapter have been previously published<sup>84</sup>; available for open access and are utilized with permission of publisher.

### 6.2. Introduction

Detection and quantification of cell viability and growth in two-dimensional (2D) and three-dimensional (3D) cell cultures commonly involve harvesting of cells and therefore requires a parallel set-up of several replicates for time-lapse or dose–response studies. Currently, cell growth or proliferation of flat 2D cultures utilize MTT assay, flow cytometry and Ki67 staining. Similarly, measuring cell growth and proliferation in 3D cultures consist of terminal studies that may include trypsinization and staining with trypan blue and quantification. Thus, a non-invasive and touch-free detection of cell growth or proliferation in longitudinal studies, especially for 3D tumor spheroid cultures and stem cell regeneration remains a major unmet research need.

Surface acoustic waves (SAWs) have been broadly applied in many areas of micro-sensor technology. Gas sensors<sup>14</sup>, biosensors<sup>16,85</sup> and chemical sensors<sup>86</sup> are a few of the leading applications for SAW sensors. Generally, biosensors are widely used in cancer biomarker detection and bio-agent detection. Due to SAWs' advantages of low cost, small size and ease of assembly, SAW-based biosensor technologies have the potential to transform the cancer and bio-

agent detection fields <sup>16,87</sup>. However, the potential application of SAWs for the detection of cell growth has not been reported and remains to be elucidated.

SAWs consist of two particle displacement components. One is along the direction of wave propagation and the second one is normal to the surface, such as Rayleigh waves. Rayleigh waves, which generate compressional waves, are affected and damped by the liquid loading and dissipate the wave energy into the liquid. Therefore Rayleigh surface acoustic waves are less sensitive to mass loading changes<sup>88</sup>. Shear horizontal-surface acoustic waves (SH-SAW) with the substrate polarized normal to wave propagation are most commonly used in sensor applications that involve fluidics. Many different wafer types with special cuts are used for shear horizontal wave excitation, such as ST-cut Quartz<sup>15,89,90</sup> and 36 °Y-cut LiTaO<sub>3</sub><sup>88,91,92</sup>. ST-cut Quartz and 36 °Y-cut LiTaO<sub>3</sub> are very stable substrates for sensor applications. However, the electroacoustic coupling coefficient ( $K^2$ ) of ST-cut Quartz is much smaller than that of 36 °Y-cut LiTaO<sub>3</sub> (36 °Y-cut LiTaO<sub>3</sub> is 4.7<sup>93</sup> and ST-cut Quartz is 0.0016<sup>94</sup>).

Because of its high electroacoustic coupling coefficient, the 36 °Y-cut LiTaO<sub>3</sub> generates more stable signals when the SH-SAWs travel through polydimethylsiloxane (PDMS), which absorbs the majority of the energy generated by the interdigital transducers<sup>77,78</sup>. PDMS has been widely used in biomedical devices due to its biocompatibility and ease of manufacture into fluidic channels. An optimization of the PDMS channel sidewall thickness was demonstrated to reduce the damping effect of the PDMS on the wave propagation<sup>64</sup>, thereby increasing the sensitivity of the sensor. Even though 36 °Y-cut LiTaO<sub>3</sub> has a higher electroacoustic coupling coefficient, it also has a higher temperature coefficient compared to the ST-Quartz. Various guide layers can be deposited on the LiTaO<sub>3</sub> to change the phase velocity and temperature coefficient of the system. Zinc Oxide (ZnO) is a relatively common material in sensor and SAW fields. The majority of

SAW devices coated with ZnO are used as Ph<sup>95</sup> or UV sensors<sup>96</sup>. Coating a ZnO layer on a LiTaO<sub>3</sub> substrate reduces the temperature coefficient and increases the mass sensitivity<sup>97-100</sup>, hence addressing the shortcoming of the LiTaO<sub>3</sub> substrate as opposed to its alternatives.

We have been investigating the possibility of non-invasive touch-free monitoring of cell proliferation/growth in long-term 2D and 3D cell cultures. Serendipitously, we discovered that SAW-based biosensing produced a different frequency shift on different cell concentration. We reasoned that SH-SAW using 36 °Y-cut LiTaO<sub>3</sub> wafers coated with ZnO might have the potential to measure and quantify cellular mass changes. To test this idea, we utilized a PDMS channel/well and surface acoustic wave transducers coated with a ZnO layer to measure mass changes due to increasing cell numbers in normal murine RAW264.7 macrophages and human A549 lung adenocarcinoma cell lines. Our results indicate that the proposed microfluidic SAW device is capable of monitoring and quantifying cell density of both cell lines in suspension as well as cultured on a 3D-nanofiber scaffold.

### 6.3. Working Principle

The frequency of the SH-SAW shifts when the waves travel through the media inside the PDMS well due to propagation loss. When the substrate where the surface acoustic wave propagates is liquid loaded, the phase velocity and attenuation of the wave can be related to the mechanical properties of the media such as viscosity and density, and electrical characteristics such as permittivity and conductivity. The perturbation formula was originally derived from Auld's perturbation theory which applies to gas sensors and then extended to liquid phase applications by J Kondoh *et al.*<sup>86,101,102</sup>.

Change in velocity:

$$\frac{\Delta V}{V} = -\frac{K_S^2 (\sigma_1/\omega)^2 + (\epsilon_1 - \epsilon_{REF})(\epsilon_1 + \epsilon_{PIEZO})}{2 (\sigma_1/\omega)^2 + (\epsilon_1 + \epsilon_{PIEZO})^2} \quad \text{Equation 6.1}$$



Change in attenuation:

$$\frac{\Delta\alpha}{k} = \frac{K_S^2 (\sigma_1/\omega)(\epsilon_{REF} + \epsilon_{PIEZO})}{2 (\sigma_1/\omega)^2 + (\epsilon_1 + \epsilon_{PIEZO})^2} \quad \text{Equation 6.2}$$

In the equations,  $K_S^2$  represents the electromechanical coupling factor of the substrate,  $\epsilon_{PIEZO}$  is the effective dielectric constant,  $\epsilon_1$  is the dielectric constant of sample liquid,  $\epsilon_{REF}$  is the dielectric constant of the reference liquid,  $\sigma_1$  is the conductivity of the sample liquid, and  $\omega$  is the angular frequency of the SH-SAW. Based on the equation above, mixtures containing particles of different density can easily be distinguished by the SH-SAW device.

## 6.4. Design and Fabrication of Bio-Sensor

### 6.4.1. Device Design

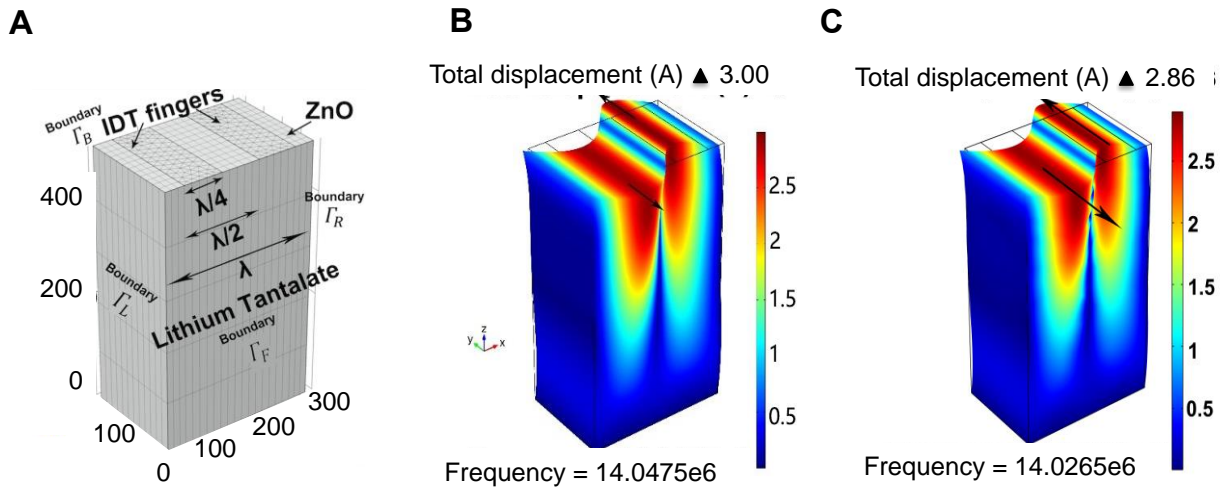


**Figure 6.1.** A 3D COMSOL model and simulation results based on the 36 °Y-cut LiTaO<sub>3</sub>: (A) 3D cell model geometry with mesh; (B) resonance frequency of the IDTs with a 200 nm thick ZnO layer; and (C) resonance frequency of the IDTs with 12.5 K cells media on the 200 nm thick ZnO layer surface

A 3D COMSOL model that consists of a two-port resonator was built to characterize changes to the wave propagation characteristics resulting from alterations to mechanical properties inside the well. A simplified 3D cell model of the Lithium tantalate resonator was built to obtain the resonator frequency shifts by the Eigen frequency module of the COMSOL software. The

individual 3D cell was set as periodic to simulate the entire SAW sensor with a fairly-simplified geometry. Figure 6.1 illustrates one wavelength cell of the simulated design with interdigital transducers (IDTs). Two interdigital transducer fingers are illustrated where one of them was connected to the ground. After the model was built and material properties were applied, a mesh was created with total degrees of freedom of 679,924. The mesh consisted of 111,679 domain elements, 28,942 boundary elements and 2892 edge elements. 36 °Y-cut LiTaO<sub>3</sub> with or without a ZnO coating was employed as the choice of substrate to simulate the resonator frequency. The simulation results indicated that the operation frequency would be 14.0475 MHz without ZnO while the fabricated operation frequency was experimentally measured as 14.056 MHz. The simulation result of the 3D-cell with ZnO is 14.03296 MHz, while the experimentally measured value is 14.04120 MHz, illustrating the validity of the developed simulation designs. As expected, the shear horizontal wave propagated in the *x* direction with the substrate polarized in the *y* direction, as illustrated in Figure 6.1B, C. Additional device design details are given in Table 6.1.

**Table 6.1.** Device parameters used for the simulation and fabrication of the IDT transducers

PARAMETERS	SETTINGS
Wavelength ( $\lambda$ )	297 $\mu\text{m}$
Number of reflecting fingers	30 pairs
Finger width	74.25 $\mu\text{m}$
Wavelength of reflecting fingers	297 $\mu\text{m}$
Number of fingers	30 pairs
Well diameter	6.5 mm
SAW velocity	4160 m/s
ZnO layer thickness	200 nm
Finger height	100 nm
Operation frequency	14.05 MHz

### 6.4.2. Device Fabrication

The IDTs were fabricated by the traditional micro-lithography methods while the microfluidic well was fabricated by the conventional PDMS micro molding technique. Further details on the fabrication process can be found in our recent reports<sup>50,54,55</sup>. After the IDTs were fabricated on the lithium tantalate substrate, ZnO sputtering was carried out. A 200 nm thick ZnO film was deposited at 150 °C in 2.5 h. After the ZnO deposition, the PDMS well was bonded to the lithium tantalate substrate after being exposed to 30 s oxygen plasma for increased bonding.

The SAW resonator can be used as a propagation delay-line with a pair of IDT transducers that serve to excite and receive the acoustic wave. Therefore a custom-designed oscillatory circuit system was used for quantifying the cell concentrations as shown in the conceptual view in Figure 6.2. Compared to other detection methods such as network analyzer, an oscillatory circuit was employed as it offers higher stability as well as higher sensitivity<sup>16,80</sup>. In the oscillator circuit detection system, the SAW sensor was employed as the feedback element of the RF amplifier. The relative change of SAW velocity due to mechanical and electrical changes resulted in an oscillation frequency shift. These changes in oscillation frequency were detected with a digital frequency counter. The setup used two variable gain RF amplifiers (Olympus 5073PR and Olympus 5072PR, Olympus NDT Inc., Waltham, MA, USA), a digital frequency counter (Agilent 53220A, Agilent Technologies Inc, Santa Clara, CA, USA), an oscillator (Tektronix TDS2001C, Tektronix Inc., Beaverton, OR, USA), as reported previously<sup>16</sup>. A band pass filter was used on the amplifier to eliminate the frequencies lower than 5 MHz and higher than 20 MHz in the loop. The two oscillation loops were employed to minimize the background noise and relate the frequency shift to the mass loading of different cell concentrations. A constant volume of different cell concentrations media was supplied to the well in the test loop for each experiment. During the

experiments, the frequency changes for the test group while the frequency of the control group remained nearly constant. From the perturbation theory, when the surface acoustic waves propagates thru the detection area of the sensor, the phase velocity changes due to mass loading from the cell media. In Equation (6.3) and (6.4) presented below,  $V_1$  is the surface wave phase velocity of the control group device and  $V_2$  is the surface wave phase velocity of the actual tested device.  $V_2'$  represents the phase velocity of the surface acoustic wave travelling through different cell concentrations. During the experiments, the only real time relative frequency  $\frac{f_2}{f_1}$  was recorded by the frequency counter. Then the data were sorted by MATLAB<sup>®</sup> and plotted out in normalized relative frequency shift.

$$\frac{\Delta V}{V} = \frac{V_2 - V_2'}{V_1} \quad \text{Equation 6.3}$$

$$\frac{\Delta f}{f} = \frac{\Delta V}{V} = \frac{f_2 - f_2'}{f_1} \quad \text{Equation 6.4}$$

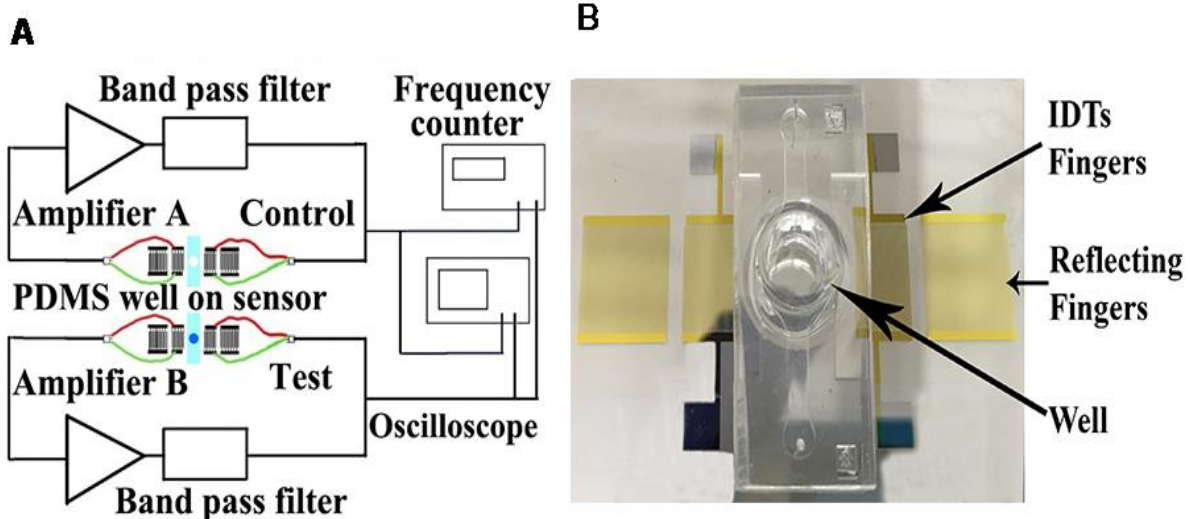


**Figure 6.2.** (A) Conceptual view of the oscillatory circuit system. Two resonators with custom-designed oscillatory circuit system were used with one of them as control group. (B) Fabricated and assembled resonator and fluidic well

## **6.5. Experimental Setup**

### **6.5.1. Experimental Protocol for SAW Measurement**

A549 human lung adenocarcinoma cells were maintained in RPMI media containing 10% fetal bovine serum (FBS) and 1% penicillin streptomycin. RAW-264.7 murine macrophages (used as an example of a non-cancerous cell) were maintained in Dulbecco's modified eagle medium (DMEM) media containing 10% FBS and 1% penicillin streptomycin. All cells were cultured in a humidified incubator at 37 °C in a 5% CO<sub>2</sub> atmosphere. Cells were collected via trypsinization and counted using a hemocytometer. For SAW measurement of cells in suspension, cell suspensions of decreasing concentration were prepared by serial dilution in phosphate buffered saline (PBS) containing 1% FBS. Half a minute after the frequency counter started to record, 100 µL of each suspension was placed on the chip of test group to record the relative frequency response for a duration of 10 min. After recording each sample, the cell suspension was removed by vacuum and the well was washed with three changes of PBS followed by three changes of water to clean the sensing area.

### **6.5.2. Experimental Protocol for Measuring Cell Viability**

We determined the cell viability using trypan blue staining in combination with a T20<sup>TM</sup> automated cell counter (Bio-Rad). Cell suspension was mixed with trypan blue at a ratio of 1:1 respectively and the resulting cell suspension was loaded on to a cassette for measurement in the cell counter. The T20<sup>TM</sup> uses microscopy in conjunction with an algorithm to calculate the total cell count and assesses the cell viability by trypan blue exclusion without any interference from the user. The advantage of this methodology is that it ensures reproducibility in the cell count independent of the users. Additionally, we validated the instrument for measuring the cell viability

by using a cell suspension sample that was heated for 15 min at 56 °C to induce cell death and show that the cell counter was able to detect increase in cell death.

### **6.5.3. Experimental Protocol for Measuring Cell Proliferation**

To examine any long term effects on cell proliferation a re-plating experiment was performed in which cells were collected and then seeded onto a 96 well culture plate after SAW measurements and allowed to grow for three days. Cell number and morphology were compared to untested control cells by both light microscopy (Olympus BX51) and by staining the cells with Hoechst 33342 (NucBlue, Life Technologies) and then capturing images using fluorescence microscopy (Olympus BX51). This assay was designed to reveal any changes to the cell proliferation rate as a result of SAW measurement.

### **6.5.4. Experimental Protocol for Culturing 3D Tumoroids**

For growing cell cultures in three-dimensions (3D), we used a fibrous scaffold developed by our lab (3P scaffold) which promotes the growth of 3D “tumoroids” when seeded with cancer cells. 3P scaffold was prepared by electrospinning as described previously<sup>103</sup>. Scaffold was placed into a 96 well plate and 5000 A549 cells were seeded into each well in RPMI media. Cells were allowed to grow on the scaffold for eight days and the culture media was changed every two days. Successful growth of cells in 3D was confirmed by staining the cells with Hoechst 33342 (NucBlue, Life Technologies) and then capturing images using fluorescence microscopy (Olympus BX51).

## **6.6. Results and Discussion**

### **6.6.1. Cell Viability and Cell Proliferation Is Not Affected after SAW Measurements**

One of our first concerns was that the cellular stress due to seeding of the cells in our device followed by exposure to acoustic waves would have a negative impact on the cells’ viability and their ability to proliferate. To demonstrate the procedure’s innocuous nature and thus its utility in

translational lab setting, we determined cell viability as described in the experimental setup. We tested the viability of both normal (RAW 264.7) and cancerous (A549) cells immediately following SAW measurement by trypan blue exclusion. Three replicates were tested for each concentration of both cell lines. A student's *t*-test was used to determine any significant difference in viability between each pair of control and SAW tested groups. A *p*-value  $\leq 0.05$  was considered to be significant. As seen in Figure 6.3, out of the 12 groups compared, only one showed any significant difference in viability.

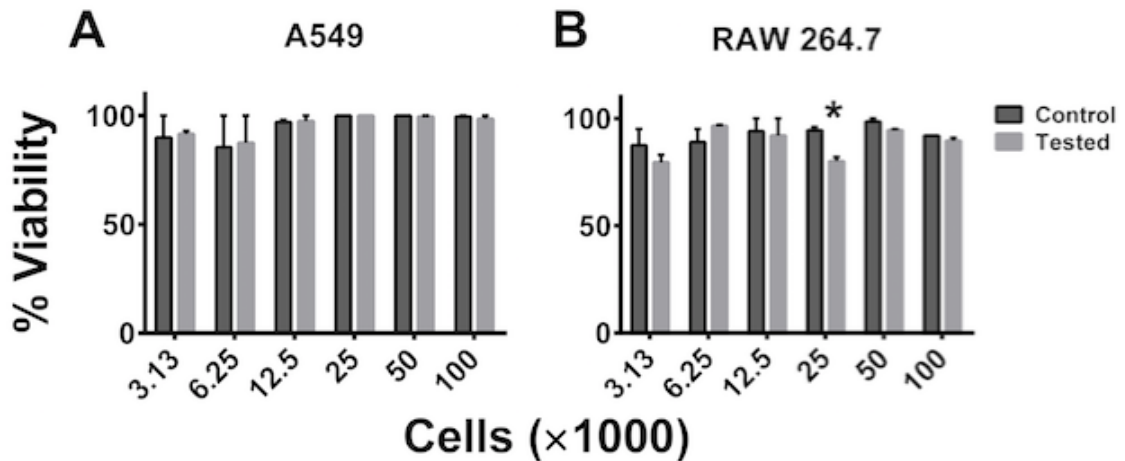


**Figure 6.3.** Cell viability following SAW measurement.

Immediately following SAW measurement the viability of (A) A549 and (B) RAW 264.7 cells was determined by trypan blue exclusion. Data is plotted as mean  $\pm$  standard error of the mean. The data is a representative of a study that was performed in triplicates and performed at least two independent times. A student's *t*-test was used to evaluate significance (\*  $p \leq 0.05$ , when compared to control). Next, we looked at the long-term effect of the SAW measurement on cell proliferation by performing a re-plating assay as described earlier. Briefly, A549 cells were collected and then seeded onto a 96-well culture plate after SAW measurements. As seen in Figure 6.4, A549 cells exposed to SAW (Figure 6.4A) and control untested cells which were not exposed to the SAW device (Figure 6.4C) reveals no obvious changes to cell morphology or growth rate



after 72 h. The nuclear staining in Figure 6.4B shows that cells have in-tact nuclei and appear healthy.

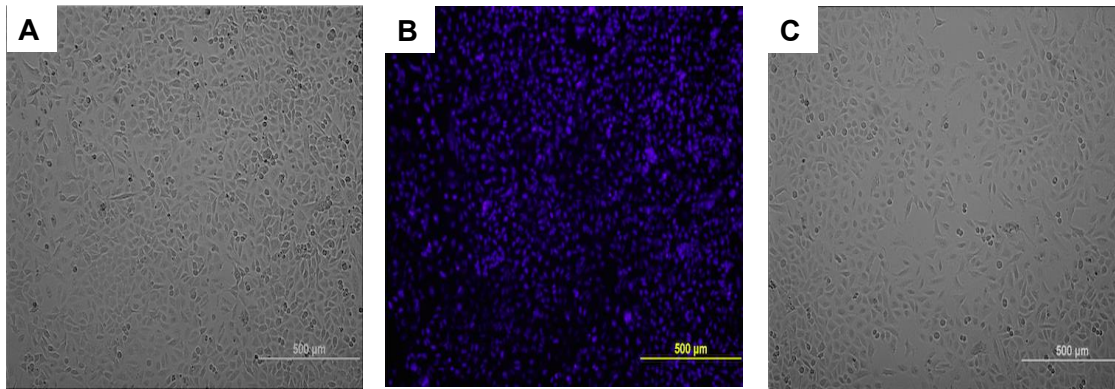


**Figure 6.4.** Cell proliferation following SAW measurement. Immediately following SAW measurement A549 cells were seeded onto a 96-well plate at a density of 5000 cells per well. Representative images of control and tested groups are shown: (A) A549 cells 72 h after SAW test, (B) NucBlue staining of A549 cells 72 h after test, and (C) control cells after 72 h

### **6.6.2. Frequency Shift Increases with Increasing Cell Concentration and Sensitivity Is Further Aided by the Use of ZnO**

Once we confirmed that our bio-sensing device and measurement protocol was bio-compatible, we next wanted to determine the sensitivity of our device in accurately measuring cell concentrations. For this we used two variations of our device, one that was coated with ZnO and the second that was kept bare. The SAW measurement protocol for both the devices was kept constant as described in the experimental setup section. Both the non-cancerous (RAW 264.7) and cancerous (A549) cells were examined in the devices at 6250, 12,500, 25,000 and 50,000 cells per 100  $\mu\text{L}$ . The concentration of cells were chosen based on cell density that we would encounter when performing actual research studies. As seen in Figure 6.5, we saw a cell dependent increase in the frequency shift in both the cell lines tested. Interestingly, the layer of ZnO increased the sensitivity of the device in recording changes in cell numbers in both of the cell lines tested. Specifically, comparing sensors containing the ZnO layer (Figure 6.5B, D) to those with the bare



substrate (Figure 6.5A, C) revealed that the ZnO layer increased the relative frequency response by four times which means it increased the sensitivity of the device.

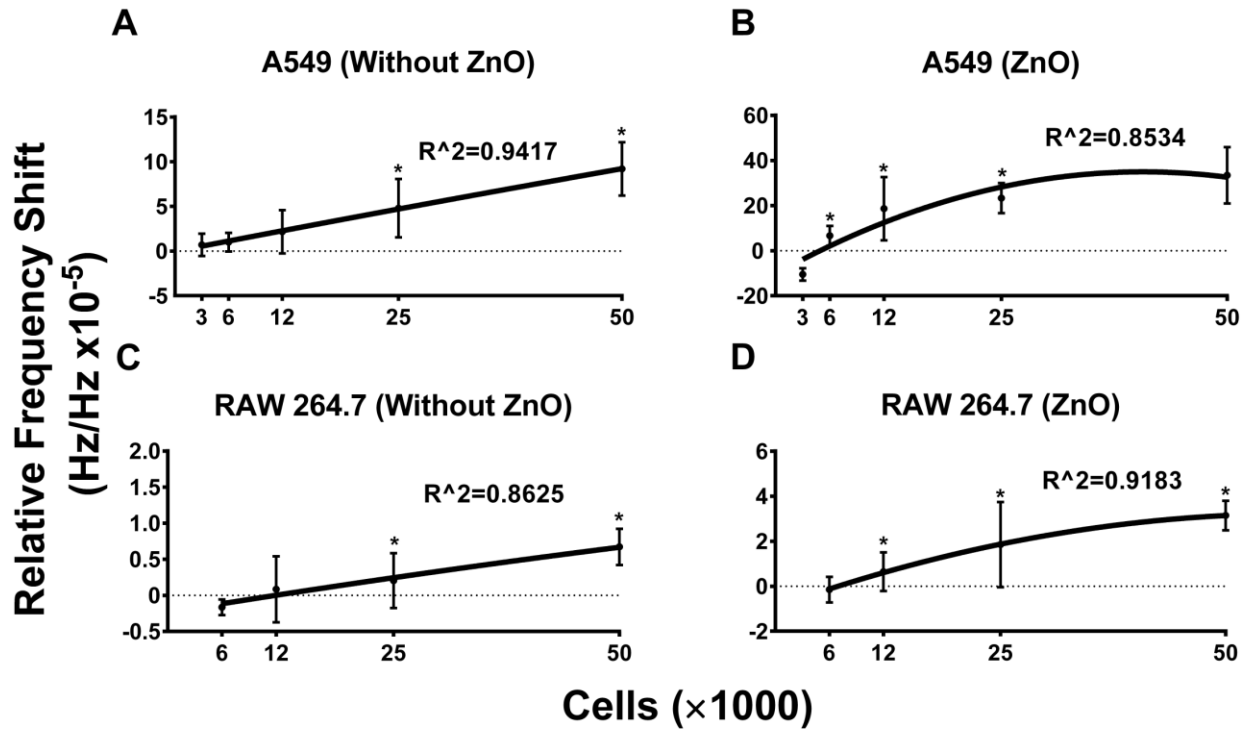


**Figure 6.5.** Relative frequency shift response to the different cell concentrations. (A,C) The bare SAW resonator response to cell with concentrations of 3000, 6250, 12,500, 25,000 and 50,000 in 100  $\mu$ L media for each test, A549 (A) and RAW 264.7 (C). (B,D) The SAW resonator coating with ZnO layer response to cells with concentration of 3000, 6250, 12,500, 25,000 and 50,000 in 100  $\mu$ L media for each test, A549 (B) and RAW 264.7. (D) Data are plotted as mean  $\pm$  95% CI. The data are representative of a study that was performed in triplicates and performed at least two independent times. A student's *t*-test was used to evaluate significance ( $p \leq 0.05$ ). \* indicates a significant difference in the frequency shift between the labeled group and the adjacent lower concentration. Best fit curves were calculated using a second order polynomial model in the GraphPad Prism software application

### 6.6.3. SAW Measurements of Cell Density Match Simulation Results

Having confirmed that our device accurately distinguishes between cell numbers, we further optimized our device for future experimental protocols. For this, we decided to establish a working theoretical model based on the 3D COMSOL model by adding mass loading module that best mimicked our bio-sensing device. One advantage of having such a model is that it will enable us to tweak several parameters on our device and run a simulation experiment without having to

spend time and money on actual experiments. Towards this goal, we set up the simulation studies, wherein the weight of each individual cell was assumed to be 1pg and different concentrations of cells were added to the ZnO surface (thickness 200 nm) on 36 °Y-cut LiTaO<sub>3</sub> substrate by modifying the mass loading in the developed model. The cell concentrations simulated were 0, 6250, 12,500, 25,000, 50,000, and 100,000 cells/microwell. After the cell (mass) loading was applied, the relative frequency response to the different cell concentrations was simulated (Figure 6.2).

In order to normalize the frequency shift obtained in response to the cell concentration, relative frequency response, which is the frequency shift over the operation frequency ( $\Delta f/f$ ), was plotted. With the cell concentration increasing (hence the mass), the phase velocity of the substrate decreased which resulted in decreasing frequency. The simulated relative frequency shift was found to be about one order of magnitude higher than the experimental results, without applying any to the simulation when presenting the results. The mismatch between the raw simulation data presented and the experimental data is expected which may be attributed to the following factors. First, the weight of the individual cell was assumed to be 1pg in the simulations for referencing purposes, whereas in actual experimentation the weight of the cells can differ significantly depending on the cell type. Second, the cells with media were placed on the bottom of the well in the actual experiments performed. On the other hand the mass loading on the entire sensor chip surface was simulated for the 3D COMSOL model. Nonetheless, there is a very good concordance of the simulated and experimental data, with a very similar match in the trends obtained (Figure 6.6). One can easily apply a correction factor to the simulation for the specific cell lines or application if closer frequency shift magnitude is needed.

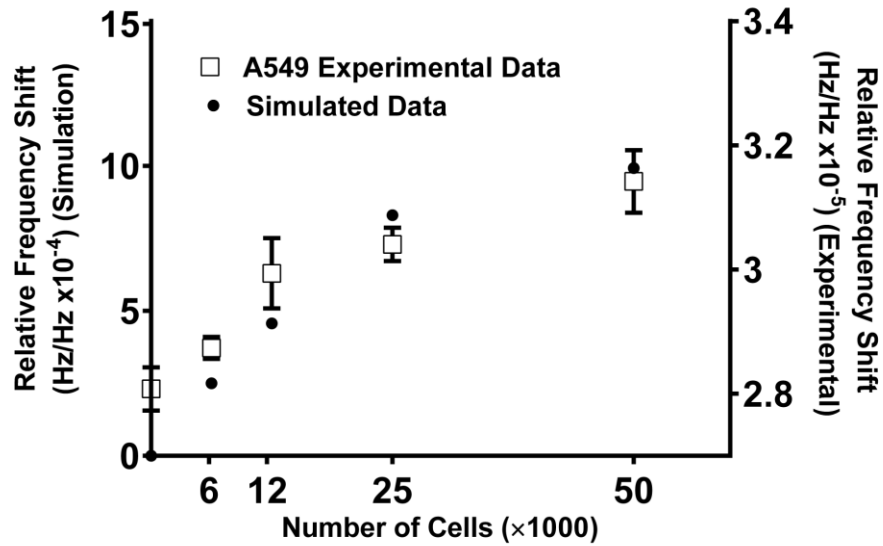


**Figure 6.6.** SAWs experiment data matches the tendency of the simulation results on the ZnO coated sensor. Experimental data are plotted as mean  $\pm$  standard error of the mean. The data is a representative of a study that was performed in triplicates

#### 6.6.4. SAW Measurements Aid in Monitoring Growth of A549 3D Spheroid Cultures

Use of 3D cell culture techniques in cancer research is rapidly expanding due to the limited ability of traditional 2D culture to accurately model *in vivo* cell behavior. To test whether the SAW device is able to measure the cell density of 3D spheroids, (also referred to as tumoroids) growing on a fiber matrix we cultured A549 cells on the matrix. A549 cells were allowed to grow on the scaffold for eight days and the culture media was changed every two days (Figure 6.7A). The 3P scaffold alone was first measured as control and corresponding reading was designated as day 0. On days 4, 6, and 8 scaffolds were removed from the plate and assayed on the SAW sensor. Data shown in Figure 6.7B demonstrate that the sensor was able to detect the change in density resulting from cell proliferation over time in the 3D environment. There was a linear increase in frequency shifts observed in A549 tumoroids with time. This increase was similar to increases in tumoroid size and number reported previously for other cancer cell lines<sup>103</sup>.

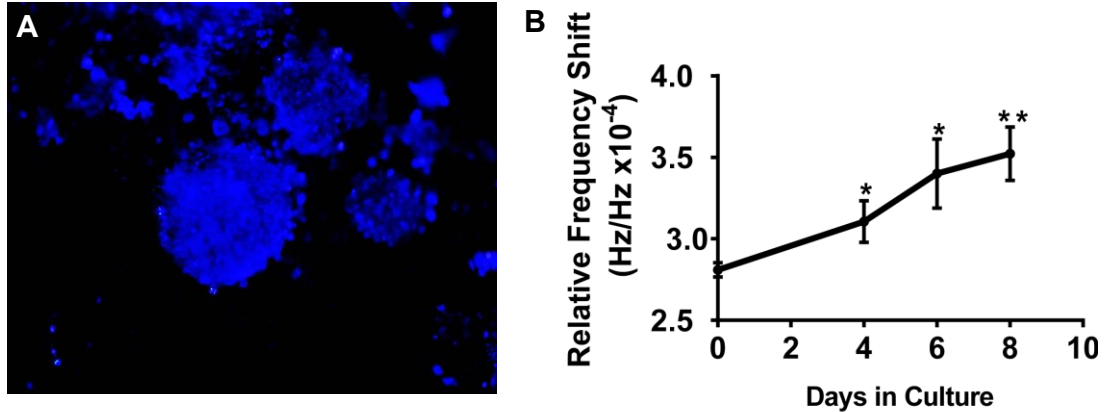


**Figure 6.7.** (A) Representative image of A549 cells growing in 3D tumoroid structures on the 3P scaffold using NucBlue nuclear stain on day 8 of culture. (B) A549 cells were cultured on the 3P scaffold for eight days. On days 0 (scaffold with no cells), 4, 6, and 8 scaffolds were collected and transferred to the SAW device with ZnO layer for measurement. Data is plotted as mean  $\pm$  standard error of the mean. The data is a representative of a study that was performed in triplicates. \* = significant increase from day 0; \*\* = significant increase from day 4 ( $p \leq 0.05$ )

## 6.7. Conclusions

Based on these results, the acoustic measurement procedure seems to have no ill effect on cell viability in either the A549 cancer cell line or the RAW 264.7 macrophages. Cell proliferation was also unaffected by SAW measurements in A549. The device's ability to detect changes in cell density on the 3D scaffold over time along with its biocompatibility reveal great potential for this device to be incorporated into 3D in vitro cancer models. The platform thus created would enable continuous real-time measurement of cell growth in a 3D environment during bio assays including drug screens, multi cell co-cultures, gene knockdown/knockout, etc.

There are several potential translational implications for these. Acoustic biosensing involves a highly sensitive and tunable SAW (37–46), which can be performed without any electrode touching the tumoroids and acoustical response can be acquired independent of existence of a magnetic/electrical field and iron oxide/MnO nanoparticles in the flow field. The potential for miniaturization and integration of complex functions into “multi-cell tumoroids on chip” exists, which is expected to revolutionize real-time tracking of biomarkers and clinical diagnostics and

prognostics of cancers in a point-of-care setting for personalizing therapy. In addition, monitoring of physiologic/metabolic tumor markers via acoustic bio-sensing is expected to increase resemblance of tumoroid cultures to in vivo tumors and provide a precise, stable, and well-defined culture environment for cellular assays.

## CHAPTER 7. CONCLUSIONS AND FUTURE WORK

### 7.1. Summary and Contributions

In this dissertation, both an acoustic actuator and an acoustic sensor platform integrated with a microfluidic system were investigated based on the surface acoustic wave properties. The background of piezoelectric materials and theory of surface acoustic waves were demonstrated in this dissertation. A simulation was carried out to improve and optimize the interdigital transducer design to increase the stability and sensitivity of the devices. Additionally, a theoretical approach was used to analyze the effect of mass loading and viscosity in microfluidic systems.

Firstly, a surface acoustic wave (SAW) based pump on a lithium niobate substrate was designed and fabricated. Experimental studies were conducted by using the thermal expansion force and body force generated by SAWs to pump the liquid inside the PDMS channel. An additional hydrophobic layer was used on the contact surface of the channel to reduce the friction force. Also, different levels of power consumption were applied to investigate the relation between power and average pumping velocity. Our results indicated that the pumping velocity for a constant liquid volume with the same applied input power could be increased by over 130% (2.31 mm/min vs 0.99 mm/min) by employing a hydrophobic surface coating (Cytop) in a thinner microchannel (250  $\mu\text{m}$  vs 500  $\mu\text{m}$ ) design.

The IDT design improvement optimization was based on the 2D and 3D COMSOL simulation results. The experiment results confirmed these improvements. Different metal ratios, finger heights, substrate thicknesses, guide layer thicknesses and guide layer materials were

investigated in detail. A full understanding of the surface acoustic wave behavior was carried out in different finger designs with different metallization ratios, finger thickness ratios and substrate thicknesses. After finger design, the 3D simulation applied different media with various mass loadings and viscosity properties, even for the dielectric properties on the surface of the substrate.

Secondly, a full research investigation was conducted on a liquid sensor by using SH-SAWs on a 36°YX cut lithium tantalate substrate. A COMSOL 3D simulation was carried out to optimize the interdigital transducer design and predict the response of the mass loading and viscosity properties. Experiments were conducted on different concentrations of glycerol to test the continuous flow with a two-port resonator design. Results confirmed that the design had a very stable signal and high sensitivity to detect the different weight concentrations of glycerol. Different weight concentrations of particles were investigated to improve sensitivity by redesigning the microchannel.

Thirdly, the resonator sensor integrated with the microfluidic system applied to a non-invasive contact-free monitoring of cell proliferation/growth platform after successfully detecting different concentrations of the particle. ZnO was applied as an optimized solution to reduce the temperature coefficient, which increased the stability and mass sensitivity. 3D simulation on different cell concentrations was conducted to predict the frequency response of the IDTs by using a 3D cell model. The final experiment results on the different cell lines (A549 and RAW264.7) showed that the resonator with a ZnO layer had four times the sensitivity of the bare wafer. Results of experiments on the cell line A549 also indicated that the simulation results matched the trend of the experiment data. Additional experiments on cell viability indicated that SAWs, ZnO layers and PDMS channels were bio-compatible for growing cells in vivo. This resonator's ability to sense the cell density from the PDMS along with its biocompatibility revealed great potential for

this device to be used on continuous real-time measurement of cell growth in a 3D environment during bio assays.

## **7.2. Future Work**

Both the SAW pump and SH-SAW sensor can be integrated onto a single lab-on-a-chip for chemistry, biomedical and biology applications. The future work for the SAW pump is to quantify the force of the SAWs body force generated as the wave travels into the liquid and also quantify the expansion force resulting from heat of the liquid. Improving the pump's efficiency over long distances and at high velocities should be part of another future study. Before taking these steps, there are a few theoretical and finite element problems that need to be further researched, such as the mathematic model for wave dissipation into the media and heat generated by the wave. The efficiency of the energy transferred to the heat needs to be investigated in the future.

An SH-SAW-based ZnO sensor works as a platform for real-time monitoring of cell line cultures. Future work on SH-SAWs should integrate the microfluidic system to replace the micro-well and introduce a multiple-layer sensor. The microfluidic system combined with a sensor will create a sealed and continuous flow environment for cell cultures. Then, multiple layers with different pairs of resonators can be achieved along with a full data analysis on cell number, cell culture media pH, and concentration of glucose—all of which can be recorded by a remote computer.



## REFERENCES

1. Rayleigh JWS. Proc. London Math Soc. 1885:17:4-11.
2. Fischerauer G, Mauder A, Müller R. *Acoustic Wave Devices.*; 2008. doi:10.1002/9783527619269.ch5g.
3. H. Meixner RJ. *Sensors: Micro- and Nanosensor Technology-Trends in Sensor Markets.*; 2008. doi:10.1002/9783527620180.
4. De Simoni G, Signore G, Agostini M, Beltram F, Piazza V. A surface-acoustic-wave-based cantilever bio-sensor. *Biosens Bioelectron.* 2015;68:570-576. doi:10.1016/j.bios.2014.12.058.
5. Di Pietrantonio F, Benetti M, Cannat D, et al. A surface acoustic wave bio-electronic nose for detection of volatile odorant molecules. *Biosens Bioelectron.* 2015;67:516-523. doi:10.1016/j.bios.2014.09.027.
6. Bracke N, Barhdadi S, Wynendaele E, Gevaert B, D'Hondt M, De Spiegeleer B. Surface acoustic wave biosensor as a functional quality method in pharmaceuticals. *Sensors Actuators, B Chem.* 2015;210:103-112. doi:10.1016/j.snb.2014.12.092.
7. Zeng Q, Guo F, Yao L, et al. Milliseconds mixing in microfluidic channel using focused surface acoustic wave. *Sensors Actuators, B Chem.* 2011;160(1):1552-1556. doi:10.1016/j.snb.2011.08.075.
8. Shilton RJ, Yeo LY, Friend JR. Quantification of surface acoustic wave induced chaotic mixing-flows in microfluidic wells. *Sensors Actuators, B Chem.* 2011;160(1):1565-1572. doi:10.1016/j.snb.2011.09.007.
9. Ding X, Peng Z, Lin S-CS, et al. Cell separation using tilted-angle standing surface acoustic waves. *Proc Natl Acad Sci.* 2014;111:12992-12997. doi:10.1073/pnas.1413325111.

10. Destgeer G, Ha BH, Jung JH, Sung HJ. Submicron separation of microspheres via travelling surface acoustic waves. *Lab Chip*. 2014;14(24):4665-4672. doi:10.1039/C4LC00868E.
11. Rajapaksa A, Qi A, Yeo LY, Coppel R, Friend JR. Enabling practical surface acoustic wave nebulizer drug delivery via amplitude modulation. *Lab Chip*. 2014;14(11):1858-1865. doi:10.1039/C4LC00232F.
12. Ghahremani M, Nabili M, Mahesh S, et al. Surface Acoustic Wave devices for ocular drug delivery. *2010 IEEE Int Ultrason Symp*. 2010:872-875. doi:10.1109/ULTSYM.2010.5935970.
13. Norbert Kockmann. Micro Process Engineering. *Fluid Dyn. Comput. Model. Appl*. 517 (2006). doi:10.1002/9783527616749.
14. Shen CY, Liou SY. Surface acoustic wave gas monitor for ppm ammonia detection. *Sensors Actuators, B Chem*. 2008;131(2):673-679. doi:10.1016/j.snb.2007.12.061.
15. Onen O, Ahmad AA, Guldiken R, Gallant ND. Surface modification on acoustic wave biosensors for enhanced specificity. *Sensors (Switzerland)*. 2012;12(9):12317-12328. doi:10.3390/s120912317.
16. Onen O, Sisman A, Gallant ND, Kruk P, Guldiken R. A urinary Bcl-2 surface acoustic wave biosensor for early ovarian cancer detection. *Sensors (Switzerland)*. 2012;12(6):7423-7437. doi:10.3390/s120607423.
17. Zimmermann C, Rebiere D, Dejous C, Pistre J, Planade R. Love-waves to improve chemical sensors sensitivity: theoretical and experimental comparison of acoustic modes. *Proc 2002 IEEE Int Freq Control Symp PDA Exhib (Cat No02CH37234)*. 2002:281-288. doi:10.1109/FREQ.2002.1075893.
18. Länge K, Grimm S, Rapp M. Chemical modification of parylene C coatings for SAW biosensors. *Sensors Actuators, B Chem*. 2007;125(2):441-446. doi:10.1016/j.snb.2007.02.039.
19. Rocha-Gaso, M.-I.; Garc ía, J.-V.; Garc ía, P.; March-Iborra, C.; Jim énez, Y.; Francis, L.-A.; Montoya, Á.; Arnau, A. Love Wave Immunosensor for the Detection of Carbaryl Pesticide. *Sensors*. 2014, *14*, 16434-16453. doi: 10.3390/s140916434.

20. Reder-Christ K, Schmitz P, Bota M, et al. A dry membrane protection technique to allow surface acoustic wave biosensor measurements of biological model membrane approaches. *Sensors (Basel)*. 2013;13(9):12392-12405. doi:10.3390/s130912392.
21. Long Y, Wang Y, Du X, Cheng L, Wu P, Jiang Y. The Different Sensitive Behaviors of a Hydrogen-Bond Acidic Polymer-Coated SAW Sensor for Chemical Warfare Agents and Their Simulants. *Sensors (Basel)*. 2015;15(8):18302-18314. doi:10.3390/s150818302.
22. Xu F, Wang W, Xue X, Hu H, Liu X, Pan Y. Development of a Wireless and Passive SAW-Based Chemical Sensor for Organophosphorous Compound Detection. 2015:30187-30198. doi:10.3390/s151229793.
23. McHale G, Newton MI, Martin F. Theoretical mass sensitivity of love wave and layer guided acoustic plate mode sensors. *J Appl Phys*. 2002;91(12):9701-9710. doi:10.1063/1.1477603.
24. Raimbault V, Rebiere D, Dejous C, Guirardel M, Pistre J, Lachaud JL. High frequency microrheological measurements of PDMS fluids using SAW microfluidic system. *Sensors Actuators, B Chem*. 2010;144(2):467-471. doi:10.1016/j.snb.2009.10.044.
25. Lindner G. Sensors and actuators based on surface acoustic waves propagating along solid-liquid interfaces. *J Phys D Appl Phys*. 2008;41(12):123002. doi:10.1088/0022-3727/41/12/123002.
26. Kogai T, Yoshimura N, Mori T, Yatsuda H. Liquid-phase shear horizontal surface acoustic wave immunosensor. *Jpn J Appl Phys*. 2010;49(7 PART 2):07HD15. doi:10.1143/JJAP.49.07HD15.
27. Kondoh J, Saito K, Shiokawa S, Suzuki H. Simultaneous Measurements of Liquid Properties Using Multichannel Shear Horizontal Surface Acoustic Wave Microsensor. *Jpn J Appl Phys*. 1996;35(Part 1, No. 5B):3093-3096. doi:10.1143/JJAP.35.3093.
28. Mitsakakis K, Tserepi a., Gizeli E. SAW device integrated with microfluidics for array-type biosensing. *Microelectron Eng*. 2009;86(4-6):1416-1418. doi:10.1016/j.mee.2008.12.063.
29. Research PM. Global Industry Insight: Neem Extract Market Development and Demand Forecast to 2020. 2015:66p.

30. Hashimoto K-Y. *Surface Acoustic Wave Devices in Telecommunications: Modelling and Simulation.*; 2013. doi:10.1007/978-3-662-04223-6.
31. Rinken T. State of the art in biosensors - General Aspects. In: *InTech*. Vol ; 2013:360. doi:10.5772/45832.
32. Jacques Curie and PC. Development, via compression, of electric polarization in hemihedral crystals with inclined faces. *Bull Soc min éral Fr*. 1880;3:90.
33. Curie J, Curie P. Contractions and expansions produced by voltages in hemihedral crystals with inclined faces. *Comptes Rendus*. 1881;(93):1137-1140.
34. Piezo ceramics in medicine: healthy, and getting better. *Free Libr*. 2014. <http://www.thefreelibrary.com/Piezo+ceramics+in+medicine%3a+healthy%2c+and+getting+better.-a0112538697>.
35. Dineva P, Gross D, Müller R, Rangelov T. Piezoelectric Materials. In: *Engineering Analysis of Smart Material Systems*. Vol Springer International Publishing Switzerland 2014; 2014:7-32. doi:10.1007/978-3-319-03961-9\_2.
36. Moro GD. *Surface Wave Analysis for Near Surface Applications.*; 2015. doi:10.1016/B978-0-12-800770-9.15003-4.
37. Campbell C. *Surface Acoustic Wave Devices for Mobile and Wireless Communications.*; 1998. doi:10.1016/B978-0-12-157345-4.50006-0.
38. Campbell C. Surface Acoustic Wave Devices and their Signal Processing Applications. *Surf Acoust Wave Devices their Signal Process Appl*. 1989:9-30. doi:10.1016/B978-0-12-157345-4.50006-0.
39. Campbell C. *Surface Acoustic Wave Devices and Their Signal Processing Applications.*; 1989. doi:10.1016/B978-0-12-157345-4.50006-0.
40. Kino GS. *Acoustic Waves: Devices, Imaging, and Analog Signal Processing*. Vol 100. 1987.
41. Ristic VM. *Principles of Acoustic Devices*, John Wiley & Sons, Inc.; 1983.

42. Ballantine Jr DS, White RM, Martin SJ, et al. *Acoustic Wave Sensors: Theory, Design, & Physico-Chemical Applications.*; 1996.
43. G. Endoh, K-y. Hashimoto and MY. Surface acoustic wave propagation characterisation by finite-element method and spectral domain analysis. *Jpn J Appl Phys.* 1995;34:2638. DOI: 10.1143/JJAP.34.2638
44. N. Rama Krishnan, H. B. Nemade and RP. Simulation of one-port saw resonator using comsol multiphysics. COMSOL Users conference 2006 Bangalore. [https://www.researchgate.net/publication/268297760\\_Simulation\\_of\\_One-Port\\_SAW\\_Resonator\\_using\\_COMSOL\\_Multiphysics](https://www.researchgate.net/publication/268297760_Simulation_of_One-Port_SAW_Resonator_using_COMSOL_Multiphysics)
45. Namdeo AK, Nemade HB. Simulation on Effects of Electrical Loading due to Interdigital Transducers in Surface Acoustic Wave Resonator. *Procedia Eng.* 2013;64:322-330. doi:10.1016/j.proeng.2013.09.104.
46. Ruppel, Clemens CW and Fjeldly TA. *Advances in Surface Acoustic Wave Technology, Systems and Applications.*; 2000.
47. Raj VB, Singh H, Nimal a T, Sharma MU, Gupta V. Oxide thin films (ZnO, TeO<sub>2</sub>, SnO<sub>2</sub>, and TiO<sub>2</sub>) based surface acoustic wave (SAW) E-nose for the detection of chemical warfare agents. *Sensors Actuators, B Chem.* 2013;178:636-647. doi:10.1016/j.snb.2012.12.074.
48. Guigen Zhang, Nanostructure-Enhanced Surface Acoustic Waves Biosensor and Its Computational Modeling. *Journal of Sensors.* 2009; doi:10.1155/2009/215085
49. Tao Wang, Qi Ni, Nathan C and Guldiken R. Surface Acoustic Wave Based Pumping in a Microchannel. *Microsystem Technol.* 2016; doi:10.1007/s00542-016-2880-9.
50. Jo MC, Guldiken R. Dual surface acoustic wave-based active mixing in a microfluidic channel. *Sensors Actuators, A Phys.* 2013;196:1-7. doi:10.1016/j.sna.2013.03.028.
51. Tan MK, Yeo LY, Friend JR. Rapid fluid flow and mixing induced in microchannels using surface acoustic waves. *EPL (Europhysics Lett.* 2009;87(4):47003. doi:10.1209/0295-5075/87/47003.
52. Sritharan K, Strobl CJ, Schneider MF, Wixforth A, Guttenberg Z. Acoustic mixing at low Reynold's numbers. *Appl Phys Lett.* 2006;88(5):054102. doi:10.1063/1.2171482.

53. Dung Luong T, Trung Nguyen N. Surface Acoustic Wave Driven Microfluidics—A Review. *Micro Nanosyst.* 2010;2(3):217-225. doi:10.2174/1876402911002030217.
54. Guldiken R, Jo MC, Gallant ND, Demirci U, Zhe J. Sheathless size-based acoustic particle separation. *Sensors.* 2012;12(1):905-922. doi:10.3390/s120100905.
55. Jo MC, Guldiken R. Active density-based separation using standing surface acoustic waves. *Sensors Actuators, A Phys.* 2012;187:22-28. doi:10.1016/j.sna.2012.08.020.
56. Jo MC, Guldiken R. Particle manipulation by phase-shifting of surface acoustic waves. *Sensors Actuators, A Phys.* 2014;207:39-42. doi:10.1016/j.sna.2013.12.020.
57. Shabani R, Cho HJ. Active surface tension driven micropump using droplet/meniscus pressure gradient. *2011 16th Int Solid-State Sensors, Actuators Microsystems Conf TRANSDUCERS'11.* 2011;180:1296-1299. doi:10.1109/transducers.2011.5969412.
58. Laser DJ, Santiago JG. A review of micropumps. *J Micromechanics Microengineering.* 2004;14(6):R35-R64. doi:10.1088/0960-1317/14/6/R01.
59. Alghane M, Fu YQ, Chen BX, Li Y, Desmulliez MPY, Walton a. J. Streaming phenomenon induced by Rayleigh surface acoustic wave in microdroplets. *J Appl Phys.* 2011;109(8):0-12. doi:10.1063/1.4758282.
60. Cecchini M, Girardo S, Pisignano D, Cingolani R, Beltram F. Acoustic-counterflow microfluidics by surface acoustic waves. *Appl Phys Lett.* 2008;92(10):104103. doi:10.1063/1.2889951.
61. Masini L, Cecchini M, Girardo S, Cingolani R, Pisignano D, Beltram F. Surface-acoustic-wave counterflow micropumps for on-chip liquid motion control in two-dimensional microchannel arrays. *Lab Chip.* 2010;10(15):1997. doi:10.1039/c000490a.
62. Girardo S, Cecchini M, Beltram F, Cingolani R, Pisignano D. Polydimethylsiloxane–LiNbO<sub>3</sub> surface acoustic wave micropump devices for fluid control into microchannels. *Lab Chip.* 2008;8(9):1557. doi:10.1039/b803967d.
63. Schmid L, Wixforth A, Weitz DA, Franke T. Novel surface acoustic wave (SAW)-driven closed PDMS flow chamber. *Microfluid Nanofluidics.* 2012;12(1-4):229-235. doi:10.1007/s10404-011-0867-5.

64. Jo MC, Guldiken R. Effects of polydimethylsiloxane (PDMS) microchannels on surface acoustic wave-based microfluidic devices. *Microelectron Eng.* 2014;113:98-104. doi:10.1016/j.mee.2013.07.021.
65. Tseng W-K, Lin J-L, Sung W-C, Chen S-H, Lee G-B. Active micro-mixers using surface acoustic waves on Y-cut 128 °LiNbO<sub>3</sub>. *J Micromechanics Microengineering.* 2006;16(3):539-548. doi:10.1088/0960-1317/16/3/009.
66. Rahimi P, Ward C a. Kinetics of evaporation: Statistical rate theory approach. *Int J Thermodyn.* 2005;8(1):1-14.
67. Feder ME. *Environmental Physiology of the Amphibians.* Chicago u.a.: Univ. of Chicago Press; 1992. <https://books.google.com/books?hl=en&lr=&id=oaS-OpEjPtUC&pgis=1>.
68. Mohanan AA, Islam MS, Ali SHM, Parthiban R, Ramakrishnan N. Investigation into mass loading sensitivity of Sezawa wave mode-based surface acoustic wave sensors. *Sensors (Switzerland).* 2013;13(2):2164-2175. doi:10.3390/s130202164.
69. Kaletta UC, Wenger C. FEM simulation of Rayleigh waves for CMOS compatible SAW devices based on AlN/SiO<sub>2</sub>/Si(100). *Ultrasonics.* 2014;54(1):291-295. doi:10.1016/j.ultras.2013.04.009.
70. Guldiken R, Jo MC, Gallant ND, Demirci U, Zhe J. Sheathless size-based acoustic particle separation. *Sensors (Basel).* 2012;12(1):905-922. doi:10.3390/s120100905.
71. Uchida D, Sugiura S, Go YSJS, Nakanishi H, Funatsu T, Shoji S. PDMS Microfluidic Devices With PTFE Passivated Channels. *7th Int Conf Miniaturized Chem Biochem Anal Syst.*:429-432.
72. Alghane M, Fu YQ, Chen BX, Li Y, Desmulliez MPY, Walton AJ. Frequency effect on streaming phenomenon induced by Rayleigh surface acoustic wave in microdroplets. *J Appl Phys.* 2012;112(8):084902. doi:10.1063/1.4758282.
73. Mata A, Fleischman AJ, Roy S. Characterization of Polydimethylsiloxane (PDMS) Properties for Biomedical Micro/Nanosystems. *Biomed Microdevices.* 2005;7(4):281-293. doi:10.1007/s10544-005-6070-2.



74. Cordeiro A. L, Nitschke M, Janke A, et al. Fluorination of poly(dimethylsiloxane) surfaces by low pressure CF<sub>4</sub> plasma-Physicochemical and antifouling properties. *Express Polym Lett.* 2009;3(2):70-83. doi:10.3144/expresspolymlett.2009.11.
75. Murochi N, Sugimoto M, Matsui Y, Kondoh J. Deposition of Thin Film Using a Surface Acoustic Wave Device. *Jpn J Appl Phys.* 2007;46(7B):4754-4759. doi:10.1143/JJAP.46.4754.
76. Search H, Journals C, Contact A, Iopscience M, Address IP. Surface Acoustic Wave Liquid Sensors Based on One-Port Resonator. 1993; doi: 10.1143/JJAP.32.2372.
77. Shilton RJ, Travagliati M, Beltram F, Cecchini M. Microfluidic pumping through miniaturized channels driven by ultra-high frequency surface acoustic waves. *Appl Phys Lett.* 2014;105(7):074106. doi:10.1063/1.4893975.
78. Li F. *The Acoustic Wave Sensor and Soft Lithography Technologies for Cell Biological Studies*. ProQuest, UMI Dissertation Publishing (September 4, 2011); 2009. <http://d-scholarship.pitt.edu/8744/>.
79. Kogai T, Yoshimura N, Mori T, Yatsuda H. Liquid-phase shear horizontal surface acoustic wave immunosensor. *Jpn J Appl Phys.* 2010;49(7 PART 2). doi:10.1143/JJAP.49.07HD15.
80. March-iborra C, Montoya-baides Á, Arnau-vives A. Surface Generated Acoustic Wave Biosensors for the Detection of Pathogens: A Review. *Sensors.* 2009;9(12):5740-5769. doi:10.3390/s90705740.
81. Wang W, Liu J, Xie X, Liu M, He S. Development of a new surface acoustic wave based gyroscope on a X-112 °Y LiTaO<sub>3</sub> substrate. *Sensors.* 2011;11(11):10894-10906. doi:10.3390/s111110894.
82. Zhang G. Orientation of Piezoelectric Crystals and Acoustic Wave Propagation. *COMSOL Conf.* 2012:20. [http://www.comsol.asia/papers/13727/download/zhang\\_paper.pdf](http://www.comsol.asia/papers/13727/download/zhang_paper.pdf).
83. Segur J. *Physical Properties of Glycerol and Its Solutions*. Glycerine Producers' Association; 1953. <http://scholar.google.com/scholar?hl=en&btnG=Search&q=intitle:Physical+Properties+of+Glycerine+and+Its+Solutions#0>. Accessed December 8, 2014.




84. Wang T, Green R, Nair RR, et al. Surface acoustic waves (SAW)-based biosensing for quantification of cell growth in 2D and 3D Cultures. *Sensors (Switzerland)*. 2015;15(12):32045-32055. doi:10.3390/s151229909.
85. Onen O, Ahmad AA, Guldiken R, Gallant ND. Surface Modification on Acoustic Wave Biosensors for Enhanced Specificity. 2012:12317-12328. doi:10.3390/s120912317.
86. Vivancos J-L, Rącz Z, Cole M, Gardner JW. Surface acoustic wave based analytical system for the detection of liquid detergents. *Sensors Actuators, B Chem.* 2012;171-172:469-477. doi:10.1016/j.snb.2012.05.014.
87. Pomowski A, Baricham C, Rapp BE, Matern A, Länge K. Acoustic Biosensors Coated With Phosphorylcholine Groups for Label-Free Detection of Human C-Reactive Protein in Serum. 2015;15(8):4388-4392. doi: 10.1109/JSEN.2015.2419278
88. Nomura T, Saitoh A, Horikoshi Y. Measurement of acoustic properties of liquid using liquid flow SH-SAW sensor system. *Sensors Actuators, B Chem.* 2001;76(1-3):69-73. doi:10.1016/S0925-4005(01)00571-8.
89. Deobagkar D. Acoustic wave immunosensing of Escherichia coli in water. *Sensors Actuators B Chem.* 2005;104(1):85-89. doi:10.1016/j.snb.2004.04.106.
90. Roederer JE, Bastiaans GJ. Microgravimetric immunoassay with piezoelectric crystals. *Anal Chem.* 1983;55(14):2333-2336. doi:10.1021/ac00264a030.
91. Kondoh J, Tabushi S, Matsui Y, Shiokawa S. Development of methanol sensor using a shear horizontal surface acoustic wave device for a direct methanol fuel cell. *Sensors Actuators B Chem.* 2008;129(2):575-580. doi: 10.1016/j.snb.2007.09.023.
92. Nomura T, Saitoh A., Miyazaki T. Liquid sensor probe using reflecting SH-SAW delay line. *Sensors Actuators, B Chem.* 2003;91(1-3):298-302. doi:10.1016/S0925-4005(03)00103-5.
93. Pang HF, Fu YQ, Li ZJ, et al. Love mode surface acoustic wave ultraviolet sensor using ZnO films deposited on 36 °Y-cut LiTaO<sub>3</sub>. *Sensors Actuators, A Phys.* 2013;193:87-94. doi:10.1016/j.sna.2013.01.016.

94. Lam CS, Lam CS, Wang YJC, Wang YJC, Wang SM, Wang SM. A Review of the Recent Development of Temperature Stable Cuts of Quartz for SAW Applications. *Ultrasonics*. 2004;1:1-7.
95. Oh H, Lee KJ, Baek J, Yang SS, Lee K. Development of a high sensitive pH sensor based on shear horizontal surface acoustic wave with ZnO nanoparticles. *Microelectron Eng*. 2013;111:154-159. doi:10.1016/j.mee.2013.03.097.
96. Chivukula V, Ciplys D, Shur M, Dutta P. ZnO nanoparticle surface acoustic wave UV sensor. *Appl Phys Lett*. 2010;96(23):3-6. doi:10.1063/1.3447932.
97. Powell, D.A.; Kalantar-zadeh, K.; Ippolito, S.; Wlodarski W. A layered SAW device based on ZnO/LiTaO<sub>3</sub> for liquid media sensing applications. *Proc 2002 IEEE Int Ultrason Symp*. Volume 1:493-496.
98. Powell DA, Kalantar-Zadeh K, Wlodarski W. Numerical calculation of SAW sensitivity: Application to ZnO/LiTaO<sub>3</sub> transducers. *Sensors Actuators, A Phys*. 2004;115(2-3 SPEC. ISS.):456-461. doi:10.1016/j.sna.2004.05.031.
99. Chang R-C, Chu S-Y, Hong C-S, Chuang Y-T. A study of Love wave devices in ZnO/Quartz and ZnO/LiTaO<sub>3</sub> structures. *Thin Solid Films*. 2006;498(1):146-151. doi:10.1016/j.tsf.2005.07.065.
100. Fu YQ, Luo JK, Du XY, et al. Recent developments on ZnO films for acoustic wave based bio-sensing and microfluidic applications: a review. *Sensors Actuators B Chem*. 2010;143(2):606-619. doi:10.1016/j.snb.2009.10.010.
101. Kondoh J. A liquid-phase sensor using shear horizontal surface acoustic wave devices. *Electron Commun Japan*. 2013;96(2):41-49. doi:10.1002/ecj.10407.
102. Onen O, Guldiken R. Investigation of guided surface acoustic wave sensors by analytical modeling and perturbation analysis. *Sensors Actuators, A Phys*. 2014;205(January):38-46. doi:10.1016/j.sna.2013.10.021.
103. Girard YK, Wang C, Ravi S, et al. A 3D Fibrous Scaffold Inducing Tumoroids: A Platform for Anticancer Drug Development. *PLoS One*. 2013;8(10). doi:10.1371/journal.pone.0075345.

## APPENDICES

## Appendix A. Copyright Clearance (Chapter 4)

All referenced figures and manuscript and figures of Chapter 4 have been previously published in journal “Microsystem Technologies”. The authorization of reproduction of author’s own manuscript is granted by the copyright transfer letter.



Springer

Copyright Transfer 17.02.2016

visit us at [springer.com](http://springer.com)

---

### Confirmation of your Copyright Transfer

---

Dear Author,

Please note: This e-mail is a confirmation of your copyright transfer and was sent to you only for your own records.

The copyright to this article, including any graphic elements therein (e.g. illustrations, charts, moving images), is hereby assigned for good and valuable consideration to Springer-Verlag Berlin Heidelberg effective if and when the article is accepted for publication and to the extent assignable if assignability is restricted for by applicable law or regulations (e.g. for U.S. government or crown employees). Author warrants (i) that he/she is the sole owner or has been authorized by any additional copyright owner to assign the right, (ii) that the article does not infringe any third party rights and no license from or payments to a third party is required to publish the article and (iii) that the article has not been previously published or licensed.

The copyright assignment includes without limitation the exclusive, assignable and sublicensable right, unlimited in time and territory, to reproduce, publish, distribute, transmit, make available and store the article, including abstracts thereof, in all forms of media of expression now known or developed in the future, including pre- and reprints, translations, photographic reproductions and microform. Springer may use the article in whole or in part in electronic form, such as use in databases or data networks for display, print or download to stationary or portable devices. This includes interactive and multimedia use and the right to alter the article to the extent necessary for such use.

Authors may self-archive the Author’s accepted manuscript of their articles on their own websites. Authors may also deposit this version of the article in any repository, provided it is only made publicly available 12 months after official publication or later. He/she may not use the publisher’s version (the final article), which is posted on SpringerLink and other Springer websites, for the purpose of self-archiving or deposit. Furthermore, the Author may only post his/her version provided acknowledgement is given to the original source of publication and a link is inserted to the published article on Springer’s website. The link must be provided by inserting the DOI number of the article in the following sentence: “The final publication is available at Springer via <http://dx.doi.org/insert DOI>”.

Prior versions of the article published on non-commercial pre-print servers like arXiv.org can remain on these servers and/or can be updated with Author’s accepted version. The final published version (in pdf or html/xml format) cannot be used for this purpose. Acknowledgement needs to be given to the final publication and a link must be inserted to the published article on Springer’s website, by inserting the DOI number of the article in the following sentence: “The final publication is available at Springer via <http://dx.doi.org/insert DOI>”. **Author retains the right to use his/her article for his/her further scientific career by including the final published journal article in other publications such as dissertations and postdoctoral qualifications provided acknowledgement is given to the original source of publication.**

Articles disseminated via <http://link.springer.com> are indexed, abstracted and referenced by many abstracting and information services, bibliographic networks, subscription agencies, library networks, and consortia.

After submission of the agreement signed by the corresponding author, changes of authorship or in the order of the authors listed will not be accepted by Springer.

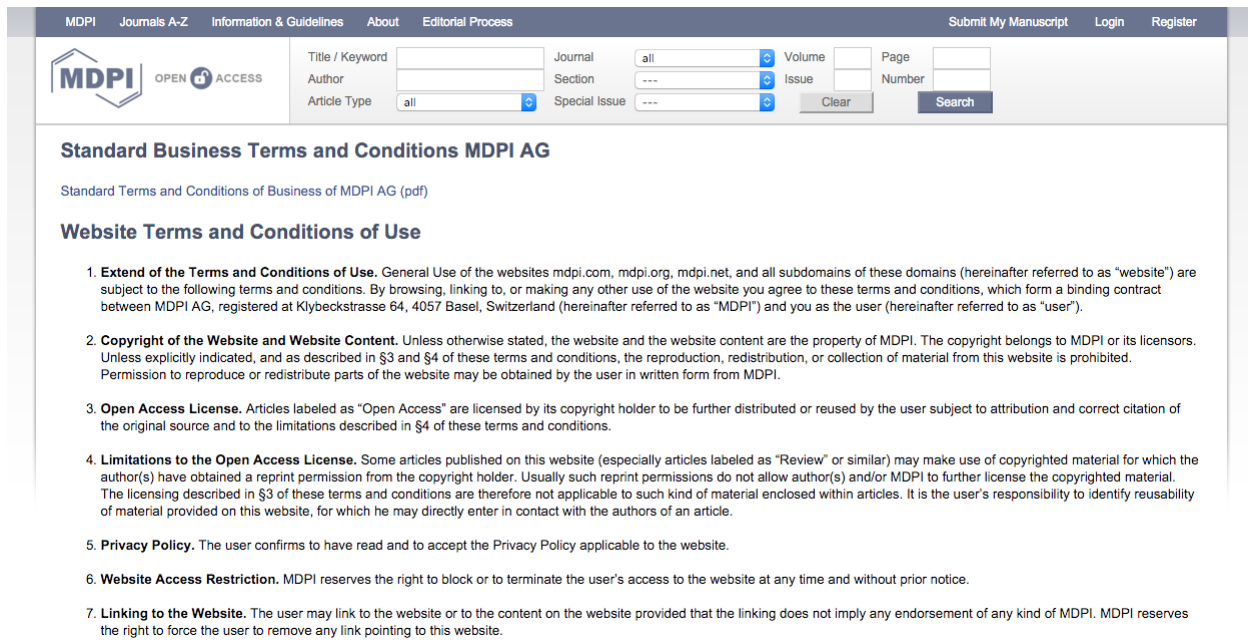
This is an automated e-mail; please do not reply to this account. If you have any questions, please go to our [help pages](#).

Thank you very much.

Kind regards,  
Springer Author Services

## Appendix B. Copyright Clearance (Chapter 6)

All referenced figures and manuscript and figures of Chapter 6 were published in open access journal “Sensors MDPI”. The authorization of reproduction of author’s own manuscript is granted by terms of use as stated in “3. Open Access License.” from the webpage: <http://www.mdpi.com/about/termsfuse>.



The screenshot shows the MDPI website interface. At the top, there is a navigation bar with links for MDPI, Journals A-Z, Information & Guidelines, About, and Editorial Process. On the right side of the navigation bar, there are links for Submit My Manuscript, Login, and Register. Below the navigation bar is a search bar with the MDPI logo and the text 'OPEN ACCESS'. The search bar contains several input fields: Title / Keyword, Author, Article Type, Journal, Section, Special Issue, Volume, Issue, Page, and Number. There are also 'Clear' and 'Search' buttons. Below the search bar, the page displays the 'Standard Business Terms and Conditions MDPI AG' page. The page title is 'Standard Business Terms and Conditions MDPI AG' and it includes a link to the 'Standard Terms and Conditions of Business of MDPI AG (pdf)'. The main content of the page is titled 'Website Terms and Conditions of Use' and contains seven numbered sections:

- 1. Extend of the Terms and Conditions of Use.** General Use of the websites mdpi.com, mdpi.org, mdpi.net, and all subdomains of these domains (hereinafter referred to as "website") are subject to the following terms and conditions. By browsing, linking to, or making any other use of the website you agree to these terms and conditions, which form a binding contract between MDPI AG, registered at Klybeckstrasse 64, 4057 Basel, Switzerland (hereinafter referred to as "MDPI") and you as the user (hereinafter referred to as "user").
- 2. Copyright of the Website and Website Content.** Unless otherwise stated, the website and the website content are the property of MDPI. The copyright belongs to MDPI or its licensors. Unless explicitly indicated, and as described in §3 and §4 of these terms and conditions, the reproduction, redistribution, or collection of material from this website is prohibited. Permission to reproduce or redistribute parts of the website may be obtained by the user in written form from MDPI.
- 3. Open Access License.** Articles labeled as "Open Access" are licensed by its copyright holder to be further distributed or reused by the user subject to attribution and correct citation of the original source and to the limitations described in §4 of these terms and conditions.
- 4. Limitations to the Open Access License.** Some articles published on this website (especially articles labeled as "Review" or similar) may make use of copyrighted material for which the author(s) have obtained a reprint permission from the copyright holder. Usually such reprint permissions do not allow author(s) and/or MDPI to further license the copyrighted material. The licensing described in §3 of these terms and conditions are therefore not applicable to such kind of material enclosed within articles. It is the user's responsibility to identify reusability of material provided on this website, for which he may directly enter in contact with the authors of an article.
- 5. Privacy Policy.** The user confirms to have read and to accept the Privacy Policy applicable to the website.
- 6. Website Access Restriction.** MDPI reserves the right to block or to terminate the user's access to the website at any time and without prior notice.
- 7. Linking to the Website.** The user may link to the website or to the content on the website provided that the linking does not imply any endorsement of any kind of MDPI. MDPI reserves the right to force the user to remove any link pointing to this website.